Speciation of molybdenum- and vanadium-based polyoxometalate species in aqueous medium and gas-phase and its consequences for M1 structured MoV oxide synthesis

vorlegt von

Master of Science

Sabrina Jung

geb. in Gießen

von der Fakultät II – Mathematik und Naturwissenschaften

der Technischen Universität Berlin

zur Erlangung des akademischen Grades

Doktor der Naturwissenschaften

Dr. rer. nat.

genehmigte Dissertation

Promotionsausschuss:

Vorsitzender: Prof. Dr. Reinhard Schomäker

Gutachter: Prof. Dr. Robert Schlögl

Gutachter: Prof. Dr. Erhard Kemnitz

Gutachter: Prof. Dr. Martin Lerch

Tag der wissenschaftlichen Aussprache: 19.07.2018

Berlin 2018

Für meinen 91-jährigen Opa,

der so viel in seinem Leben gesehen, erlebt, und erreicht hat.

Ich bin glücklich und dem Universum mehr als dankbar, dass du (noch) da bist,

um dieses Ereignis mit mir zu teilen.

There is a theory which states that if ever anyone discovers exactly what the Universe is for and why it is here, it will instantly disappear and be replaced by something even more bizarre and inexplicable. There is another theory which states that this has already happened.

- Douglas Adams

Acknowledgement

First and foremost, I want to thank Prof. Dr. Robert Schlögl who offered me the opportunity to conduct my PhD studies at the Fritz-Haber-Institute of the Max-Planck-Society. It was a pleasure to have all this equipment at my disposal, and never having to wait long for anything. Also, always knowing which great minds have worked and shaped the scientific world here helped and inspired me a lot. Prof. Schlögl has always pushed my work forward, being it with criticism, humor, and/or great ideas, and I will be eternally grateful for that.

Great appreciation and thanks go to Dr. Annette Trunschke, who supervised and guided me through this work. This work would not have been possible without our regular meetings and discussions, which always left me optimistic even in spite of negative results. Her criticism, positive and negative, has contributed a lot to my scientific and personal growth.

I also want to thank Dr. Gert von Helden, Dr. Mateusz Marianski, Dr. Jongcheol Seo, und Dr. Johanna Hofmann of the Molecular Physics department, who gave me the opportunity to pursue part of my work at their mass spectrometers and the free electron laser, supported me with calculations, and were always ready for a good discussion.

Many thanks go to Dr. Frank Girgsdies, Dr. Olaf Timpe, Maike Hashagen, Dipl. Ing. Wiebke Frandsen, and Liudmyla Masliuk, who supported this work with their analytic skills and discussions.

I want to thank especially Stephen Lohr and Sven Richter, who for one introduced me to the great world of hydrothermal synthesis and for the other helped me out with my synthesis plans.

I highly appreciate Dr. Gregor Koch and Pierre Kube for their endless fountains of knowledge and their readiness to share it with me at any time. Additionally, I thank Pierre a lot for his catalytic tests of my samples.

Great appreciation goes out to all PhD students who worked with me in the PhDNet, especially Elisabeth Wolf for accompanying me through the fun and the madness.

I also want to acknowledge Andrea Moebius and Sabrina Wobring, who were always readily available for any administrative problems, cookies, sweets, and if I just needed to vent.

In the end, work is no fun at all without the right colleagues. Hence, I want to thank all people in the AC department who made these past 3.5 years to what they are. Especially I want to thank those of you, who became so much more than colleagues to me: Jasmin, Maike, Stephen.

Finally, I want to thank all family members and friends who relentlessly asked when they would „finally get a letter from Frau Doktor Sabrina Jung“ and with that simultaneously annoyed and motivated me.

Abstract

Polyoxomolybdate and –vanadate speciation has been examined in aqueous solution and in the gas-phase depending on the concentration and pH value. Raman and UV-vis spectroscopy showed the compact and highly charged hepta- and octamolybdate, and decavanadate species to be present, respectively, while mass spectrometric measurements led to a multitude of different species. The structure of these gas-phase species was determined by infrared multiple photon dissociation spectroscopy accompanied by density functional theory calculations. In the case of molybdates, three structural regimes in the form of chains, rings, and Lindqvist-derived structures were found.

Mixed MoV solutions with different vanadium sources (metavanadate $[VO_3]_n^{n-}$ or vanadyl VO^{2+}) were investigated with the same procedure. The presence of vanadyl species in the solution led to the formation of Keplerate $\{Mo_{72}V_{30}\}$, a crucial precursor for the M1 structure. With decreasing total metal concentration, the mixed species in the gas-phase became vanadium-richer, while at the same time hydrothermal synthesis produced less product yield.

Dilution of the $MoVO_x$ synthesis precursor solution led to the formation of basic M1 structural characteristics, however in different extents of phase-purity and defectiveness. While the number of defects in the *a*-*b*-plane and amorphous phase increases with decreasing metal concentration, the three dimensional M1 layer structure is formed regardless.

1 % of vanadium concentration was substituted with various metals with different oxidation states, but similar ionic radii, to decrease the segregation of vanadium to the surface during catalysis. The resulting solids consisted of phase-pure M1 structure and a third metal in concentrations between 0.2 and 0.3 at%, while the vanadium content was simultaneously decreased compared to the unsubstituted $MoVO_x$. In the oxidative dehydrogenation of ethane, Te and As as substituents led to the best catalytic results with selectivity to ethylene of 95 % or more at their respective highest conversions at 290 °C and the lowest apparent activation energies. Furthermore, all substituted MoV oxides showed better catalytic results than the unsubstituted M1 $MoVO_x$,

Zusammenfassung

Die Speziation von Polyoxomolybdaten und –vanadaten in wässriger Lösung und in der Gasphase wurde abhängig von Konzentration und pH-Wert untersucht. Raman und UV-vis Spektroskopie zeigten kompakte und hochgeladene Hepta- und Oktamolybdate, und Dekavanadate anwesend in den jeweiligen Lösungen, während massenspektrometrische Messungen auf eine Vielzahl unterschiedlicher Spezies hinwies. Die Struktur dieser Gasphasenspezies wurde mittels Infrared Multiphoton Dissoziation (IRMPD) Spektroskopie im Zusammenspiel mit Dichtefunktionaltheorie (DFT) bestimmt. Im Fall von Molybdaten wurden drei strukturelle Regimes in Form von Ketten, Ringen, und Lindqvist-abgeleiteten Strukturen gefunden.

Gemische MoV Lösungen mit unterschiedlichen Vanadiumquellen (Metavanadat $[VO_3]_n^{n-}$ oder Vanadyl VO^{2+}) wurden auf die gleiche Art und Weise untersucht. Die Anwesenheit von Vanadylspezies in der Lösung führte zum Entstehen von Keplerat $\{Mo_{72}V_{30}\}$. Mit abnehmender Metallkonzentration wurden die gemischen Spezies in der Gasphase reicher an Vanadium, während gleichzeitig die Hydrothermalsynthese zu weniger Produktausbeute führte.

Die Verdünnung der Eduktlösung zur MoVOx synthese führte zur Bildung grundlegender M1 Strukturelemente in unterschiedlichen Maßen der Phasenreinheit und Defektbehaftung. Während die Anzahl der Defekte in der a-b-Ebene und die Präsenz amorpher Phase mit abnehmener Metallkonzentration zunahmen, wurde unabhängig davon die dreidimensionale M1 Lagenstruktur gebildet.

1 % der Vanadiumkonzentration wurde mit diversen Metallen unterschiedlicher Oxidationszustände aber ähnlicher Ionenradii substitutiert, um die Segregation von Vanadium an die Oberfläche während der Katalyse zu verringern. Die daraus resultierenden Feststoffe hatten phasenreiner M1 Struktur und eine Drittmetalkonzentration zwischen 0,2 und 0,3 at% inne, während der Vanadiumgehalt gleichzeitig gesunken war im Vergleich zum unsubstituierten $MoVO_x$.

In der oxidativen Dehydrogenierung (ODH) von Ethan zeigten Te und As als Substituenten die besten katalytischen Ergebnisse mit einer Selektivität zu Ethen von 95 % oder mehr bei ihren jeweiligen höchsten Konversionsraten bei 290 °C und die geringsten scheinbaren aktivierungsenergien. Zudem besaßen alle alle substituierten MoV Oxide bessere katalytische Ergebnisse als das unsubstituierte M1 $MoVO_x$.

List of figures

List of tables

Table of contents

1. Introduction

The introduction to this work deals with the basic concepts of heterogeneous oxidation catalysis (part 1.1.1), with a focus on different solid catalysts that have either been used in the past or are currently investigated for the (partial) (amm)oxidation of light alkanes or alkenes (chapters 1.1.2-1.1.5) This will be followed up by details about metal oxoanions important for the synthesis of MoV-based oxides (chapter 1.2.1), and subsequently the influence of synthesis parameters (1.2.2) and thermal activation (1.2.3) on the structural and hence catalytic outcome of the catalyst precursor material. A brief summary of these influences will be given, and chapter 1.3 will end with the research questions and motivations for this work.

1.1 Transition metal oxide phases in oxidation catalysis

1.1.1 Catalytic oxidation of light alkanes

For the production of light alkenes from their corresponding alkanes, oxidative dehydrogenation (ODH) reactions can be applied. With the introduction of an oxidant – commonly O_2 – to the reactor, otherwise evolving hydrogen can be oxidised, the reaction becomes exothermic and requires lower temperatures. This also leads to the reduction of side reactions like coke formation and cracking of the alkane. However, it is difficult to control the total oxidation of carbon oxides.

Different mechanistic approaches have been postulated for this kind of catalytic reactions. While these approaches differ in various ways, they have four characteristic steps in common: (1) the alkane interacts with the catalyst surface via physical or weak adsorption, (2) a C-H bond is broken to form the alkyl species, (3) the alkyl species reacts with a neighbouring surface oxygen in form of a β-elimination and the alkene is formed, (4) the catalyst is again reduced or reoxidised.[6]

One approach to describe the catalytic mechanism in alkane ODH is the Langmuir-Hinshelwood (LH) model. It is based on the assumption that a surface consists of non-interacting adsorption sites, and that all reaction stages apart from the rate-determining step are close to thermodynamic equilibrium. Any kind of step can be rate-determining.

The Eley-Rideal Model is based on the Langmuir assumptions for the adsorption, i.e. equilibrated adsorption on the surface of the catalyst, followed by the reaction of the adsorbed species with molecules from the gas-phase. The Rake model considers the dehydrogenation products as intermediates in a series of consecutive oxidation reactions to total oxidation of the alkane.

In the context of ODH, the Mars-van-Krevelen (MvK) model is regularly discussed. It assumes that the oxygen used in the reaction originates from the surface lattice of the catalyst, while the catalyst is reoxidised later on by oxygen from the gas-phase. This model concerns itself more with the state of the catalyst than the catalytic reaction compared to e.g. the LH model.

However, it depends on the alkane and catalyst used, in which exact way the alkane/alkene interacts with the catalyst surface. For molybdenum and vanadium oxides, for example, monomeric as well as polymeric sites might be active in ODH, and the terminal metal-oxygen bond is not involved in the oxidation.[7]

1.1.2 VO_x on oxide supports

Vanadium oxide species on different supporting materials are of interest for catalytic applications due to various favourable properties, among them cheap costs and high activity and selectivity. This type of catalyst usually consists of isolated or polymeric (sometimes both simultaneously) VO_x species distributed over a metal oxide MO. With increasing vanadia coverage, the monomeric VO_4 polymerises, subsequently forms a monolayer, and then V_2O_5 particles[8]. In the case of oxidation catalysis, VO_x/MO systems are applied mostly for the dehydrogenation of alcohols and alkanes.

The catalytic activity and selectivity of supported VO_x depends mainly on two factors: (i) the coverage of $VO_{x[8]}$, and (ii) the chosen support oxide[9-11]. Generally it can be said, that the catalyst possesses higher activity if the coverage of VO_x species is one monolayer or below[10, 12], and that catalysts based on reducible MO supports fare better[13-16].

VO_x on TiO_2 has been used as a catalyst for oxidative dehydrogenation of methanol to formaldehyde[17-19], and of dehydration of ethanol to ethylene and acetaldehyde[17]. In these reactions the reducible V-O-Ti bond plays a major role for the chemical activity, since it stabilises higher oxidation states of vanadium.

Another reducible supporting oxide is ceria, which leads to very active sub-monolayer catalysts[20-22]. V_2O_3 as well as V_2O_5 can be formed on the surface of CeO_2 after the correct oxidation treatment, leading to different results in catalytic activity in methanol oxidation. In the case of V_2O_5/CeO_2, cerium is

partially present in the oxidation state +IV, thus forming a strong interaction with the vanadium oxide, leading to desorption of formaldehyde at 267 °C. If V_2O_3 is present on the surface, cerium remains completely in the oxidation state of +III, and formaldehyde desorbs at higher temperatures of 332 °C[23, 24].

Regarding non-reducible supporting oxides, Al_2O_3, SiO_2, and ZrO_2 are usually chosen. VO_x/SiO_2 has been applied for the ODH of propane, showing a selectivity to propylene of 88.3 % at a propane conversion of 3.0 % at a temperature of 450 °C[25]. VO_x/ZrO_2 and VO_x/Al_2O_3 have been tested in the ODH of ethanol and propane and showed ODH rates of 0.11 and 0.006 mol_{AA}/mol_{vS}, and 0.033 and 0.03 mol_{C3H6}/mol_{Vs}, respectively, performing significantly lower that titania-supported VO_x (0.41 mol_{AA}/mol_{Vs} and 0.261 mol_{C3H6}/mol_{Vs}, respectively)[16].

However, VO_x/MO systems are mainly used as model catalysts and are only applied on an industrial scale for other catalytic processes than alkane oxidation.

1.1.3 Vanadyl pyrophosphate

While vanadyl phosphates (short VPO) technically do not belong to the material class of metal oxides, they possess a vanadyl bond, are the most active catalysts in the C_4 oxidation to maleic anhydride, and hence should be addressed briefly.

$VO(HPO_4) * 0.5\ H_2O$ is synthesised via heating of V_2O_5 in H_3PO_4 and is a bright yellow solid. Catalytic activity is achieved by thermally activating the precursor species to transform into vanadyl pyrophosphate $(VO)_2(P_2O_7)$. Additionally, other crystalline phases like α_I, α_{II}, β, γ, δ, and metastable o polymorphs of $VOPO_4$ are present in VPO compounds[26]. The final phase composition of the catalyst is determined by the preparation method and activation parameters. However, it has been discovered that the amount of surface area is detrimental to the conversion of n-butane, and not the phase composition[27, 28]. Hence, an active VPO catalyst consists of an amorphous surface supported on a highly crystalline vanadyl pyrophosphate[29].

Apart from the oxidation of butane, VPO catalysts have also been tested in the ammoxidation of various alkanes[27, 30].

1.1.4 Polyoxometalates and heteropolyacids

Polyoxometalates (POM) are anionic species of transition metals (mainly molybdenum, vanadium, and tungsten) in their highest oxidation states linked by oxygen atoms to form a three dimensional framework. POMs can be divided into two classes: (i) isopolyoxometalates, which are made up of only one type of metal, and (ii) heteropolyoxometalates, which consist of at least one transition metal, and a main group hetero atom.

Heteropoly acids (HPA) are a certain type of acid based on heteropolyoxometalates, which in their most known forms are either structurally based on the Keggin structure $H_nXM_{12}O_{40}$ or the Dawson structure $H_nX_2M_{18}O_{62}$. In both cases, X resembles an atom from the p-block of the periodic table like silicon or phosphorus, and M a transition metal such as molybdenum, tungsten, vanadium, among others.

Both compound classes are formed by condensation reactions in aqueous media based on the presence of protons in the solution. The lower the pH value, the more condensed and possibly higher charged are the POM species. At high pH values, monomeric species prevail.

For catalytic purposes, the POM and HPA species are fixated on a variety of supporting materials – some even possessing catalytic properties themselves – since the aqueous species are otherwise difficult to use in heterogeneous catalysis. Examples for different combinations of compounds and their respective oxidation catalysis reactions are listed below.

Keggin-type POM substituted with zinc, manganese, titanium, and iron have been applied in the epoxidation of alkenes with H_2O_2 as oxidant by various research groups[31-36], for example [g-$SiW_{10}O_{34}(H_2O)]^{4-}$, which even showed selectivity of 99 % or more for the epoxidation of cyclic and linear C_3-C_8 molecules[37, 38] or $[TBA]_5PTiW_{11}O_{40}$[39]. These Keggin polyoxometalates with lipophilic TBA counter cations have also shown activity in the oxidation of cyclooctane to cyclooctyl hydroperoxide in the cases of $[XW_{12}O_{40}]$, $[XW_{11}O_{39}]$, $[XW_{11}VO_{40}]$, and $[XW_{11}M^{III}(H_2O)O_{40}]$ with X being either Si or P, and M being either Fe and Mn[40]. Alcohols have been selectively epoxidated as well with $[WZnM_2(ZnW_9O_{34})_2]^{q-}$ (M = Mn, Ru, Fe, Pd, Pt, Zn) and hydrogen peroxide[41].

Homogeneous oxidation of propene to acetone, and 1-butene to butanone have been performed by palladium supplemented $H_{3+x}PV_xMo_{12-x}O_{40}$ (x = 1-4)[42]. Other oxidation reactions have been executed as well with this type of compounds. Aldehydes have been oxidised with $TBA_5H_2PW_8V_4O_{40}$[43] and ε-Keggin $[Mo_{12}V_{39}(\mu_2\text{-}OH)_{10}H_2\{X^{II}(H_2O)_3\}_4]$ with X being Ni, Co, Mn, or Cu[44]. Oxidation catalysis of alkanes[45], arenes[46-48], sulphur containing compounds[49-51], and nitrogen containing compounds[52, 53] have also been reported. For example, $[\gamma\text{-}SiW_{10}O_{36}(PhPO)_2]^{4-}$ can oxidise olefins, alcohols, and sulphides with a product yield of 97 % or more[54, 55].

Heteropoly acids can be either precipitated and hybridised, or immobilised on a given support material. Very common choices for this are zeolites, since they offer a high surface area value and structural stability. {PMo_{12}} and {$SiMo_{12}$} HPA compounds have been hydrothermally incorporated into Y-zeolite and used for the oxidation of methanol to formaldehyde[56]. Also, {PW_{12}} has been impregnated on Y-zeolite in water and has been used for the liquid phase oxidation of various substrates with H_2O_2[57, 58]. Alcohols and alkenes have been oxidised with {PMo_{11}} on zeolite Hβ, showing the highest activity for a HPA loading of 30 wt%. The oxidation of benzyl alcohol was performed with a selectivity of 90 % and a turn over number of 10,000, whereas the oxidation of styrene led to even higher TON of more than 20,000[59]. $[PZnMo_2W_{99}O_{39}]^{5-}$ was inserted into zeolite MIL-101 for the oxidation of alkenes with H_2O_2[60], as well as {PW_4} and {PW_{12}} for the oxidation of cyclohexane, which was performed with a conversion of 76% and a selectivity of 74 %[61]. The same catalytic reaction was tested with 35 wt% phosphotungstic acid encapsulating UiO-66 and led to a conversion of 94.8 % and a glutaraldehyde yield of 78.3 %[62].

One of the so far best catalysts for the ammoxidation of ethane to acetonitrile is cobalt containing BEA zeolite with an ethane conversion of 47 % and a selectivitiy to acetronitrile of 57 % at 476 °C[63].

Another special type or supports for POM or HPA are layered double hydroxides (LDH). POM- resp. HPA-LDH can be synthesised via ion exchange[64-66], co-precipidation[38], reconstitution[39], host-layer modification, or exfoliation assembly method[67]. Cyclohexene has been epoxidised with intercalated $[Mo_7O_{24}]^{6-}$ and $[W_{12}O_{41}]^{10-}$[68], and allylic alcohols with {Mg_3Al}-ionic liquid-C_8-{LaW_{10}}[69]. The latter converting trans-2-hexen-1-ol to 96 % with a selectivity of 99 % to the corresponding epoxide at room temperature. Benzyl alcohol was successfully oxidised to benzyl aldehyde with tris(hydroxymethyl)aminomethane(Tris)-LDH-$X_4(PW_9)_2$ (X = Mn, Fe, Co, Ni, Cu, Zn)[70]. Furthermore, sulfoxation has been performed with Mg_3Al-$P_2W_{17}Zn$ as catalyst[66], and N-oxidation of pyridines at room temperature with Tris-LDH-La$(PW_{11})_2$[56].

1.1.5 Mixed metal oxides

Mixed metal oxides have become an important catalyst material for different oxidation reactions, mostly of alkanes and alkenes, due to their properties, like for instance the coordination environment of the surface atoms and their oxidation states, and their redox and with that acid-base properties[71]. Since the presence of cations with variable oxidation states is important for the Mars-van-Krevelen mechanism, mixed metal oxides are suitable compounds for (partial) oxidation reactions.

Nickel niobate $NiNbO_x$ shows conversion of ethane to ethylene of 51 % at a temperature of 400 °C with a selectivity to the alkene of 90 % and is with that one of the best catalysts for the ODH of ethane.[72] Substituting nickel with antimony and supporting the resulting mixed oxide on alumina leads to a very good catalyst for the ammoxidation of the same alkane, with a conversion of 40 % and selectivity to acetonitrile of 50 % at 540 °C[63].

Generally, catalysts containing vanadium have shown a great ability for the (amm)oxidation of light alkanes. The to-date best catalysts for the dehydrogenation of propane to propene are for one VMgO

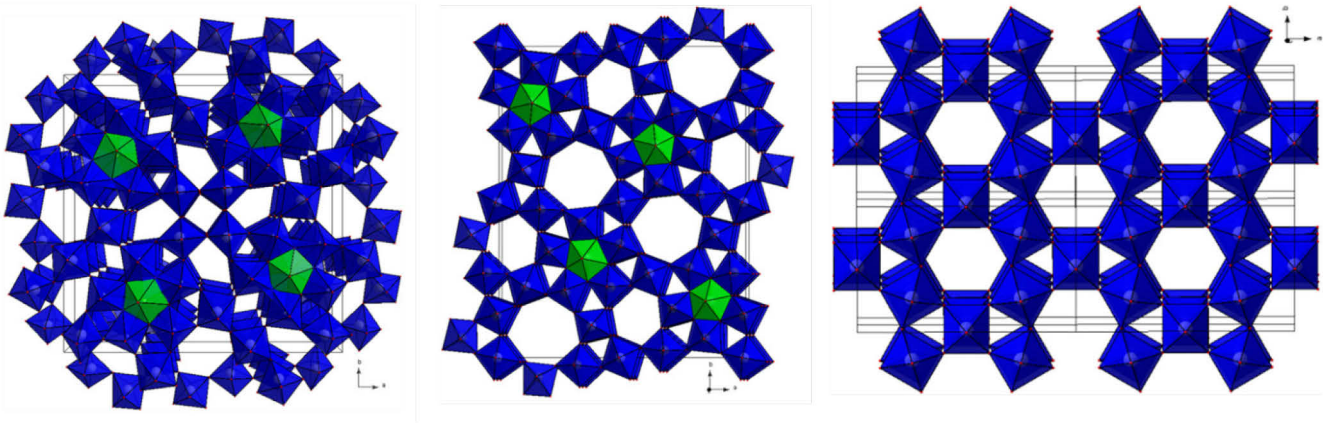

Fig. 1.1: Crystal structures of Mo_5O_{14} (left), M1 (middle), and M2 (right) mixed oxide compounds. Blue: MO_6 octahedra, green: pentagonal bipyramidal MO_7. [2]

with a propane conversion of 62 % and a corresponding selectivity of 38 %, and V-silicalite with a conversion of 30 % and a selectivity of 70 %. Both catalysts work best at temperatures around 540 – 550 °C. [63]

Not only the presence of vanadium in the mixed oxide, but also simultaneously of molybdenum enhances the catalytic properties of the mixed oxide. Three different structural types of MoV-based oxides have shown their outstanding catalytic activity in the past and present. One of these structures is the Mo_5O_{14}-type (Fig. 1.1 left), in which molybdenum atoms can be substituted with other transition metals. For example, the mixed $(VNbMo)_5O_{14}$ oxide with the sum formula $Mo_{0.73}V_{0.18}Nb_{0.09}O_x$ turned out to be one of the best catalysts for the oxidation of ethane to 100 % ethylene at 10 % conversion and 286 °C[73].

Another type of MoV oxide compound with the orthorhombic structure denoted M1 – named after the developing company Mitsubishi – has been in the focus of C_2 and C_3 oxidation catalysis since the middle of the 1990s. Originally, the oxide is made up of four transition metal elements: MoVTe(Sb)Nb(Ta). Corner-linked MO_6 octahedra are generally filled with Mo and/or V atoms, whereas niobium is located in

the centre of a MO_7 pentagonal bipyramid, and tellurium sits in the heptagonal and hexagonal channels which form along the [0 0 1] axis of the structure. Since the structure is quite complex, it is not surprising that it reacts sensitively to the synthesis parameters. Details on the synthesis and thermal activation procedures and their consequences will be discussed in more detail in chapters 1.2.2 and 1.2.3.

The variety of different metals makes these compounds excellent oxidation catalysts, especially the metal combination of MoVTeNb shows promising results in various ODH reactions. For instance, dehydrogenation of ethane to ethylene was performed with a conversion of 85 % and a selectivity of 88 % at 400 °C, the ammoxidation of propane to acrylonitrile with conversion and selectivity of 86 % and 72 %, respectively, at 420 °C. Oxidation to acrylic acid was performed at 380 °C with 80 % propane conversion and acrylic acid selectivity of 61 %. Adding palladium to the quaternary M1 oxide turns it into a viable catalyst for ethane oxidation to acetic acid at 300 °C with a selectivity of 82 % at ethane conversion[63].

During synthesis, a deviation of the M1 phase can form which is thus denoted M2 (Fig. 1.1 right) and is less catalytically active. Nevertheless, a symbiotic dependency of both M-phases during catalysis has been reported.[74]

However, only molybdenum and vanadium perform as active centres during oxidation catalysis in the Mars-van-Krevelen mechanism[75], thus an only Mo and V containing M1 structured mixed oxide can serve as a good catalyst for ODH reactions as well. In this case, vanadium tends to fill the heptagonal channels in the place of tellurium in $MoVTeNbO_x$, whereas the pentagonal bipyramidal space is filled with Mo atoms.

$MoVO_x$ can come in four different crystal structures: orthorhombic, trigonal, tetragonal, and amorphous. As with quaternary M1, the orthorhombic structure gives the best catalytic results. For instance, in the oxidation of ethane, a selectivity of 81.8 % to ethylene can be achieved at a conversion of 56.0 % (335 °C). Admittedly, amorphous $MoVO_x$ shows a selectivity of 86.7 %, however the corresponding ethane conversion is only 11.4 % at the same temperature[76].

While vanadium is considered to be the active centre for the first and rate determining step of the ODH of alkanes, and its presence is therefore detrimental to the activity of the catalyst, it has been shown that too high concentration of V in the structure can hinder the process and even lead to total combustion and deactivation in the long run[77].

1.2 Synthesis of mixed MoV oxides

1.2.1 Speciation in aqueous solutions

1.2.1.1 Molybdates

Monomolybdates like $[MoO_4]^{2-}$ are the dominant species in aqueous solutions at a molybdenum concentration of 0.1 mM or lower. At higher concentrations and a pH value of 7 or lower, protonation starts to occur. This protonation happens in two steps, the first to the mono-protonated $[HMoO_4]^-$, the second step expands the coordination number of the molybdenum from 4 to 6 in form of $[MoO_3(H_2O)_3]$, which has been proven be calculations and UV-vis spectra[78-80]. This expanding mechanism is essential to the condensation of polyoxomolybdates, since these structures usually consist of $\{MoO_6\}$ moieties.

Lowering the pH value from 7 leads to the formation of heptamolybdate $[Mo_7O_{24}]^{6-}$ and later on octamolybdate $[Mo_8O_{26}]^{4-}$, which has been shown via potentiometric measurements[81]. Additionally, the dominant presence of heptamolybdate has been identified by comparing Raman measurements of solid heptamolybdate and the respective aqueous solution[82, 83]. Also, X-ray scattering proved heptamolybdate to be dominant at a Z value of 1.14, and subsequently β-octamolybdate at Z = 1.5[84].

While both hepta- and β-octamolybdate are made up of $\{MoO_6\}$ octahedra, it is not possible to obtain the latter by just adding another octahedron to the existing heptamolybdate due to massive distortion. Other octamolybdate species are α-octamolybdate with two fourfold-coordinated molybdenum atoms, and γ-octamolybdate with two fivefold-coordinated Mo atoms incorporated in the structure. However, both species are not in measureable amounts in aqueous solution[81].

Decreasing the pH value further at high concentrations, supramolecular $[Mo_{36}O_{112}]^{8-}$ is the prominent species as shown by Raman[85, 86] and X-ray scattering[87]. At lower concentrations, a $\{Mo_{18}\}$ structure might be possible[88].

The proposed succession of molybdate species in the pH range from 8.4 to 0.5 has been confirmed by Raman[89], NMR spectroscopy[4, 89], frequency response analysis[90] and is as follows: $[MoO_4]^{2-}$, $[Mo_7O_{24}]^{6-}$, $[Mo_3O_{10}]^{2-}$, a-$[Mo_8O_{26}]^{4-}$, b-$[Mo_8O_{26}]^{4-}$, and lastly $[Mo_{36}O_{112}]^{8-}$.

Various speciation or predominance diagrams for molybdates, usually depending on the pH value and the molybdenum concentration, have been constructed over time, the most complex one being published by Baes and Meamer[91], in which the molybdate species predominance is shown over a wide range of molybdenum concentration and pH value of the aqueous solution and combines the

potentiometric data of Sasaki et al. (1959)[92], Aveston et al. (1964)[93], Sasaki and Sillén (1968)[94], and Haeringer and Schwing (1967)[95]. Said diagram is dominated by mono- and heptamolybdates in different protonation states. It shows the pH range from 1 to 7, and a concentration range from 0.1 M to 0.01 mM molybdenum. The deprotonated monomolybdate $[MoO_4]^{2-}$ dominates over the whole concentration range at pH 7 and almost all concentrations at pH 6. At pH 5 it is abundant for concentrations from 0.01 mM up to ca. 3 mM, for higher concentrations the deprotonated heptamolybdate $[Mo_7O_{24}]^{6-}$ is predominant. Around pH 4.5 a proton is added to the heptamolybdate to give $[Mo_7O_{23}(OH)]^{5-}$ or $[HMo_7O_{24}]^{5-}$ which then dominates in solutions with concentrations down to 0.7 mM. Lower concentrations are again dominated by $[MoO_4]^{2-}$. From pH 3.6 to 3.8 and concentrations below 0.1 mM, $[HMoO_4]^-$ is the dominating species. Solutions with higher concentrations still have an abundance of the singly protonated heptamolybdate. This changes as well from pH 3.6 (c = 0.1 mM) to 2.6 (c = 0.6) , where another proton is added to the species, giving $[H_2Mo_7O_{24}]^{4-}$. Solutions with lower concentrations than mentioned before are dominated by the doubly protonated H_2MoO_4, which also dominates down to pH 1 every solution with concentrations roughly below 1 mM. Solutions with concentrations over 1 mM and below pH 2.6 are dominated by the triply protonated heptamolybdate $[H_3Mo_7O_{24}]^{3-}$, although a coexistence with MoO_3, and for the lowest pH and highest concentrations with $[Mo_{19}O_{59}]^{4-}$ is possible.

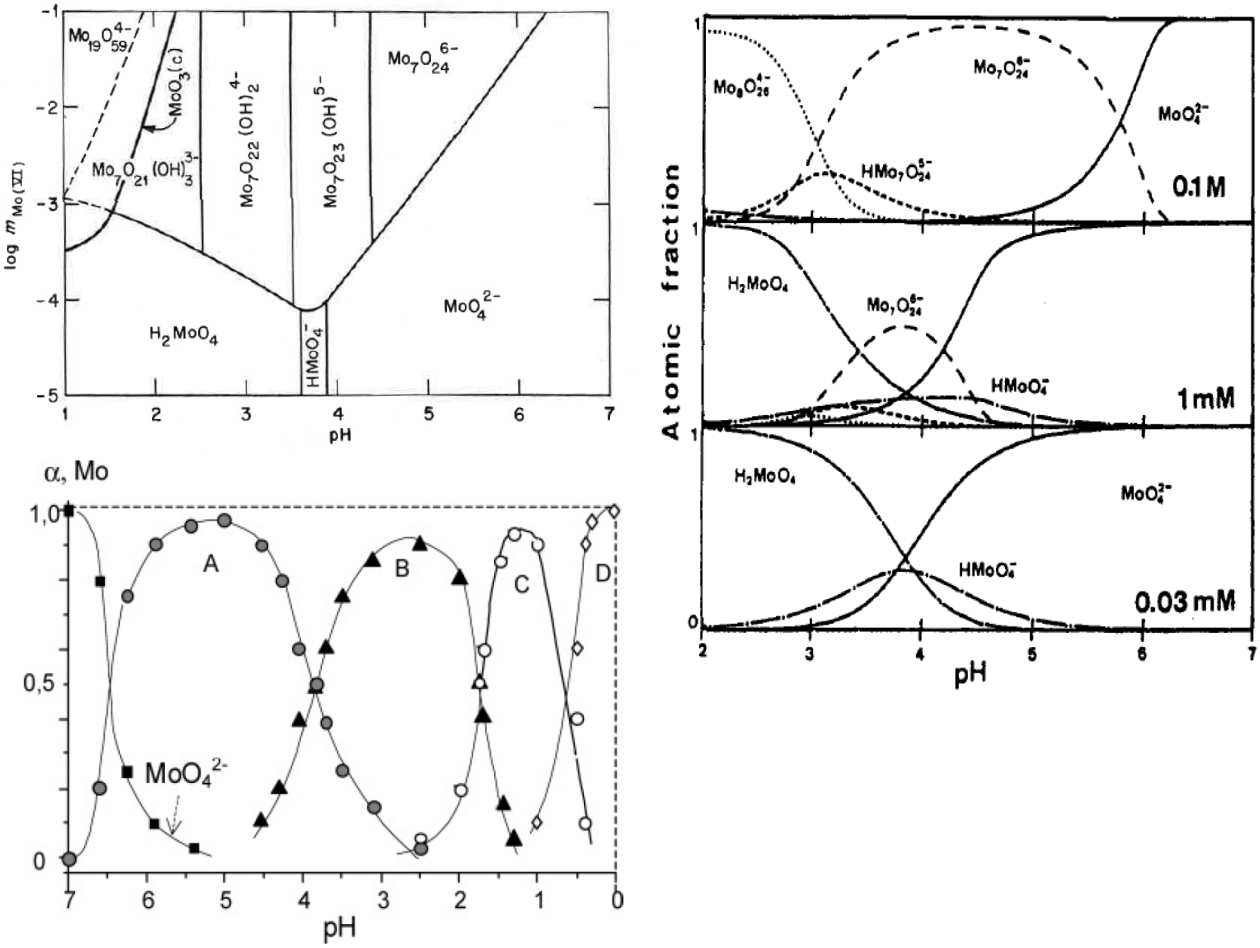

Fig. 1.2: Speciation diagrams for molybdate species in aqueous solutions. Top left: based on potentiometric data[1]. Bottom left: based on ^{95}Mo NMR spectra of 0.4 M solutions of Na_2Mo_4; (A) $H_xMo_7O_{24}^{x-6}$ (b) β-$Mo_8O_{26}^{4-}$; (C) mainly $Mo_{36}O_{112}^{8-}$; (D) cationic species including MoO_2^{2+}[4]. Right: based on formation constants.[5]

Another predominance diagram was reported by Ozeki et al.[5] in 1988 based on UV/vis measurements of aqueous molybdate solutions for low concentrations (0.03 mM Mo) and based on calculation via the formation constants for higher concentrations (1 mM and 0.1 M Mo). His results agree widely with the aforementioned, but heptamolybdate $[Mo_7O_{24}]^{6-}$ is almost exclusively present in its deprotonated form. Furthermore, at a concentration of 0.1 M and for pH values from 3 to 2, octamolybdate $[Mo_8O_{26}]^{4-}$ is the dominant species.

Maksimovskaya and Maksimov[96] analysed molybdate solutions with a concentration of 0.4 M over a pH range of 0-7 with ^{95}Mo and ^{17}O NMR. They came to the following predominance distribution: $[MoO_4]^{2-}$ (pH 7-6.5), $[H_xMo_7O_{24}]^{x-6}$ with x = 0-2 (pH 6.5-4), β-$[Mo_8O_{26}]^{4-}$ (pH 4-1.7), $[Mo_{28}Mo_{112}]^{8-}$ (pH 1.7-0.7), and finally $[MoO_2]^{2+}$ (below pH 0.7).

It is obvious that depending on the analysation method, different conclusions about the speciation are reached, especially in the region of high concentrations and low pH values.

The speciation of molybdates has also been investigated at hydrothermal conditions and temperatures between 170 and 200 °C with Raman spectroscopy[97]. Compared to the speciation taking place at ambient pressures and temperatures, dense and chain-like structures like dimolybdate $[Mo_2O_7]^{2-}$ and trimolybdate $[Mo_3O_{10}]^{2-}$ are preferred at pH values around 6 to 5, and there is no formation of supramolecular species below the pH of 2. Instead, octamolybdate poses as the final species upon acidification of the aqueous solution. Another hydrothermal study dealt with the ionisation of H_2MoO_4 between 30 and 300 °C at saturated vapour pressures and showed that the deprotonated species $[HMoO_4]^-$ and $[MoO_4]^{2-}$ are stable at high temperatures as well[98].

Apart from the presence of different molybdate species and their dominance, the structure of hydrated monomolybdate – also known as molybdic acid – has been object to many investigations due to its importance in the condensation process of polyoxomolybdates. First quantum mechanical calculations of the fractionation equilibrium constants for ^{92}Mo and ^{100}Mo in different monomeric molybdate structures showed the octahedral $[Mo(OH)_6]$ to be unstable, and suggested MoO_3 or $[MoO_3(H_2O)_3]$ to be more stable and suitable structures for the molecule[80]. The latter was supported by UV resonance Raman experiments[79]. Another calculation-based study proposed $[MoO_2(OH)_2(H_2O)_2]$ to be the more suitable structure of molybdic acid in aqueous solution[99].

1.2.1.2 Vanadates

Orthovanadate $[VO_4]^{3-}$ are already protonated at pH values of around 12 to $[HVO_4]^{2-}$, as it is a stronger base than $[MoO_4]^{2-}$. In highly diluted solutions (below 0.05 mM vanadium), the protonated monomers are almost solely present. Still, oligomers with a nuclearity between 2 and 6 or of 10 can coexist with the protonated monomer in the pH range from 0 to 12, which has been studied with potentiometry and NMR spectroscopy[100-105].

The deprotonated dimer $[V_2O_7]^{4-}$ occurs in the same pH region as $[HVO_4]^{2-}$ and possesses the same structure of corner sharing tetrahedra in the solution as in solid state[106]. Linear trivanadate $[V_3O_{10}]^{5-}$ and tetravanadate $[V_4O_{13}]^{6-}$ are also present below pH 10 as was confirmed by potentiometry and ^{51}V and ^{18}O NMR spectroscopy[107]. The cyclic tetramer $[V_4O_{12}]^{4-}$, pentamer $[V_5O_{15}]^{5-}$ and hexamer $[V_6O_{18}]^{6-}$ coexist with $[H_2VO_4]^-$ and $[H_2V_2O_7]^{2-}$ in the metavanadate region, whereby $[V_4O_{12}]^{4-}$ is the most dominant

from pH 9.5 and lower[108]. This region is defined as the pH region, where there is one negative charge per vanadium atom. Both the tetramer and pentamer have a cyclic structure of corner sharing tetrahedra in solution, and no protonated forms have been found to date[109]. Generally, all aqueous isopolyvanadates are based on either corner sharing VO_4 tetrahedra or arrays of cubically packed edge-sharing VO_6 octahedra.

VO_6-based decavanadate $[V_{10}O_{28}]^{6-}$ and three of its protonated forms emerge below a pH value of 6.5, whereas singly and doubly protonated decavanadates dominate. Studies of examining decavanadate solutions at different pH values showed that it tends to dissociate into smaller tetrahedral oligomers (mainly mono- and dimers) with increasing pH values, but remains detectable until pH 8.6[3]. The structure of $[V_{10}O_{28}]^{6-}$ has been proven to be the same in solution and solid state with NMR and X-ray studies[100]. $[H_3V_{10}O_{28}]^{3-}$ possesses the highest concentration at pH 2, then rapidly converses to $[VO_2(H_2O)_4]^{+}$[105].

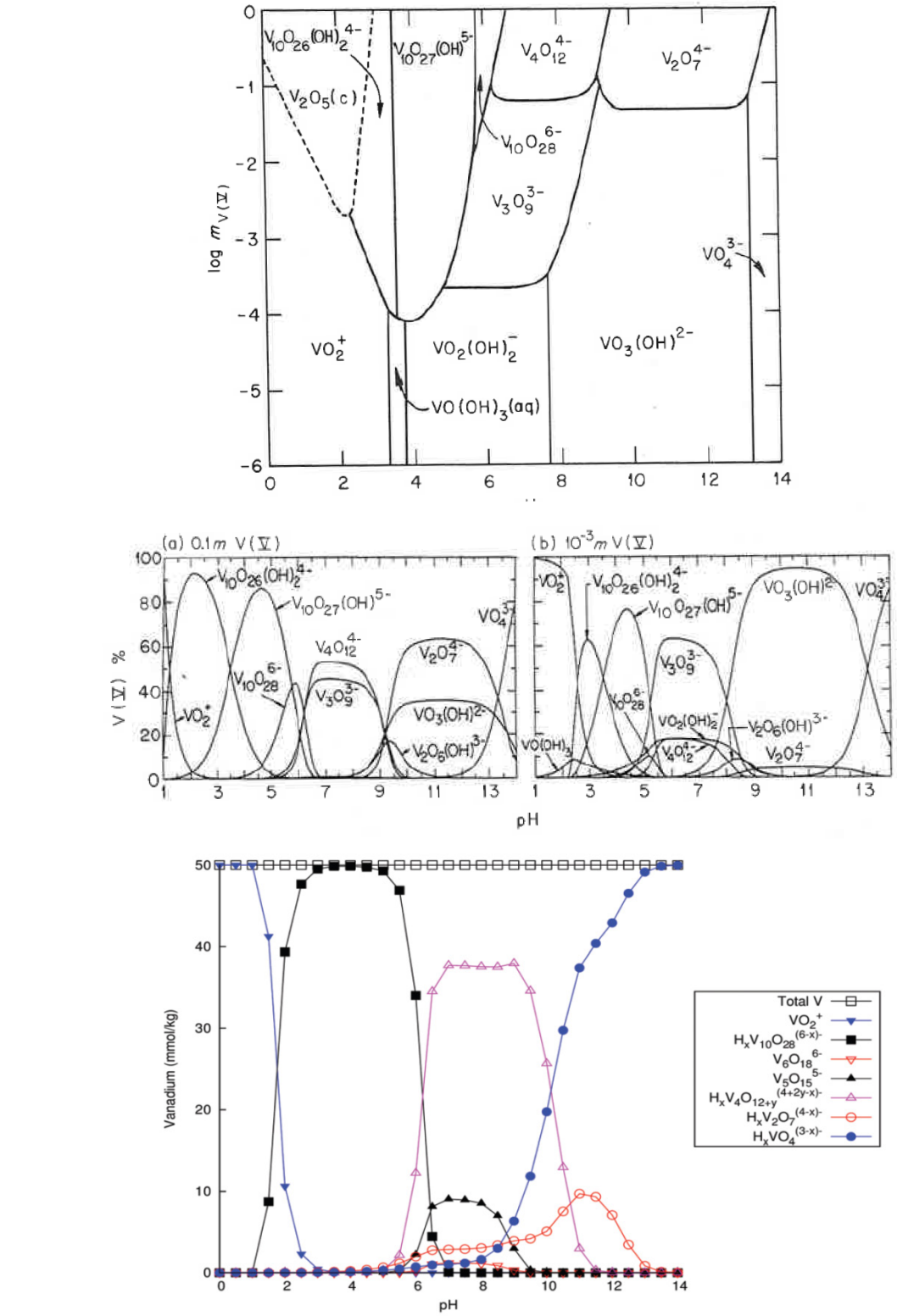

Fig. 1.2: Speciation diagrams for vanadate species in aqueous solutions. Top: based on potentiometry[1]. Middle: detailed speciation diagram for 0.1 M and 0.001 M V, based on potentiometry[1] Bottom: 50 mmol/kg vanadate solution, based on ^{51}V-NMR measurements.[3]

Decreasing the pH of the aqueous solution to 1 (at concentrations > 0.05 mM) leads to the formation of pale yellow VO_2^+ ions. These ions increase in their coordination number from 4 to 6 in the fourth protonation step to form $[VO_2(H_2O)_4]^+$, which then dimerised to the red $[V_2O_3]^{4+}$ ion[105]. Speciation diagrams including the aforementioned data is shown in Fig. 1.2.

Both diagrams top and middle of Fig. 1.2 show the distribution of vanadates as measured by potentiometry, whereby the middle diagrams not only show the most dominant species at a certain pH and concentration, but the relative concentration of all present species for two vanadium concentrations over the whole pH range. At vanadium concentrations below 0.1 mM, monomeric species dominate in solution, whereas above this value and depending on the pH in solution, decavandate, trivanadate, divanadate, or tetravanadate dominate. This clearly demonstrates the misleading nature of predominance/distribution diagrams with both pH and metal concentration as axes, since this variant does not depict the very likely presence of other species.

As in the case of molybdates, the detected species depend on the method applied: Fig. 1.2 bottom shows the relative concentration of vanadate species at 50 mmol/kg measured with ^{51}V NMR spectroscopy, and depicts tetravanadate to be the most abundant species from pH 6 to pH 10. According to potentiometric data however, trivanadate $[V_3O_9]^{3-}$ and then monovanadate should be the most dominant species. In the NMR results, trivanadate does not appear.

The structure and stability of VO_2^+ in aqueous solution was calculated with Car-Parrinello molecular dynamics (MD) and static quantum chemical calculations, as well. Sadoc et al. came to the conclusion, that the acidification of the solvent is of importance to avoid the conversion from VO_2^+ to $[VO_2(OH)]^{2-}$, which is preferred in neutral medium. In acidic medium and 500 K, $VO(OH)_3$ appeared the most stable structure[110].

Car-Parrinello molecular dynamics simulations have been applied to calculate the stability of vanadium peroxo species in high pH aqueous solutions, in which the dodecahedral $[(VO_2)_4]^{3-}$ appeared to be stable for picoseconds, and $[VO(O_2)_3]^{3-}$ formed $[VO(O_2)_2(OOH)]^{2-}$, a hydroperoxy complex [111].

1.2.1.3 Molybdovanadates

The structure of MoV species in aqueous solution can in general be described as the same octahedra-based structures of decavanadate $[V_{10}O_{28}]^{6-}$, octamolybdate β-$[Mo_8O_{26}]^{4-}$, and these molecules consume protons the same way isopolymolybdate or –vanadate species do[112].

A variety of molybdovanadates based on decavanadate has been discovered so far. ^{51}NMR spectroscopy suggests a molybdenum substituted decavanadate with the formula $[MoV_9O_{28}]^{5-}$ to be existent in solution[112, 113], as well as a doubly substituted $[Mo_2V_8O_{28}]^{4-}$ - the latter being also found by potentiometry. In both cases, molybdenum replaces the vanadium at the capping positions of the structure.

If the Mo/V ratio of the solution exceeds 1, multiple mixed anions without decavanadate structure can be detected. Among them are $[Mo_5VO_{19}]^{3-}$, protonated and deprotonated $[Mo_4V_2O_{19}]^{4-}$ in Lindqvist structure, β-$[Mo_7VO_{26}]^{5-}$ analogue to β-octamolybdate[114]. In pure vanadate or molybdate solutions, no anions with nine metal atoms are found, in mixed solutions however, $[Mo_4V_5O_{27}]^{5-}$ and its protonated from have been discovered[114].

Furthermore, there have been indications for the presence of α-$[Mo_7VO_{26}]^{4-}$, β-$[H_2Mo_6V_2O_{26}]^{5-}$, α-$[HMo_6V_2O_{26}]^{5-}$, $[Mo_4VO_{17}]^{5-}$, and $[HMo_8V_2O_{32}]^{5-}$[115].

Mixing Mo(VI) and V(IV) species in a ratio of 4:1 in an aqueous solution leads to the formation of Keplerate $\{Mo_{72}V_{30}\}$, which consists of twelve pentagonal $[Mo_6O_{21}]^{6-}$ units interlinked by 30 vanadyl units, as has been shown by Raman[116, 117], IR, and UV-vis spectroscopy[118].

Under hydrothermal conditions at temperatures around 170 to 200 °C, adding VO_2^+ to a molybdate solution leads to two possible outcomes: (1) if octamolybdate species are present in solution, MoO_3 precipitates, (2) if chain-like structured di- or trimolybdate is present, the complex mixed MoV-based M1 structure is formed[97].

1.2.1.4 Influence of other elements

The presence of other elements in the aqueous solution of polyoxometalates can have a strong impact on the speciation. Especially the ionic strength, which can be adjusted by various additives to the solution, influences the stability or formation of certain structural species, since polyanions are generally more stable at higher ionic strength.

For example at high perchloric acid concentrations, monomolybdate $[MoO_4]^{2-}$ tends to dimerise to $[Mo_2O_5(OH)H_2O]^{5+}$, whereas the doubly charged dimer is favoured at even higher perchloric acid concentrations[119]. Adding $LiClO_4$ or NaCl to an aqueous molybdate solution with lower molybdenum concentration leads to the formation of protonated and deprotonated $[Mo_7O_{24}]^{6-}$, whereby at higher concentrations up to 1 M Mo and down to pH 1 octamolybdate $[Mo_8O_{26}]^{4-}$ and $[Mo_{18}O_{56}(H_2O)_8]^{4-}$ dominate the solution[120]. Ion exchange experiments from high HCl and H_2SO_4 solutions were carried

out to illuminate the presence of anionic molybdate species within a concentration range between 1 M and 9 M, showing that Mo(IV) starts to form from 1 M H_2SO_4 and 3 M HCl[Lee]. Also, decreasing the pH from 1.92 to 0 in a sulphate solution leads to structural changes from $[H_3Mo_7O_{24}]^{3-}$ to dimer $[Mo_2O_5(SO_4)_2]^{2-}$ and lastly $[MoO_2(HSO_4)_4]^{2-}$ [121].
The speciation of molybdates was furthermore investigated in up to 5.5 M HCl solutions between 25 and 385 °C at 600 bar by XAS, whereby the molybdenum concentration varied between 0.158 and 0.414 M and the pH value between 8.7 and -0.8. No complexation took place between $[MoO_4]^{2-}$ and chloride anions at any temperature, only in highly acidified solutions a complex between $[MoO_2(H_2O)_4]^{2-}$ and Cl^- was formed. The structural change from tetrahedral to octahedral turned out to be mainly dependent on the acidity, not on temperature[122].

In the case of vanadates, decavanadate $[V_{10}O_{28}]^{6-}$ is especially affected by the ionic medium: the species is present with over 20 % in a solution including 3 M $NaClO_4$, whereas it is only a minor species if the perchlorate concentration is around 0.15 M. Also, the tendency for monomeric $[HVO_4]^{2-}$ to dimerise increases with the ionic strength of the solution. [81]

The speciation in a 0.4 mM V(V) solution depending on the concentration of sulphuric acid (1 – 16.8 mol/L) was investigated by Kurbatova et al.. From H_2SO_4 concentrations of 1 to 7 mol/L, VO_2^+ is the dominant species, with increasing acid concentration dimeric $[V_2O_3]^{4+}$ is formed. Furthermore it was found that at a sulphuric acid concentration of 12 mol/L and a vanadium concentration over 0.1 M only dimeric species are present, whereas at concentrations below 1 mM mono- and dimeric species coexist[123].

1.2.2 Precipitation and hydrothermal synthesis

Molybdenum-vanadium based oxides which solely consist of these two transition metals are often synthesised by a hydrothermal approach. The influence of synthesis parameters, like the pH of the precursor solution, or the structure of the metalate precursors, on the final product and the reaction pathways during synthesis have been studied.
Various species are present in a mixed MoV precursor solution, the most dominant being of $\{Mo_{72}V_{30}\}$, $\{Mo_{132}\}$, and $\{Mo_{57}V_6\}$ structure[76]. All these species have the $[Mo_6O_{21}]^{6-}$ – also denoted as $\{Mo(Mo_5)\}$ – unit in common, a pentagonally coordinated molybdenum centre surrounded by five MoO_6 octahedra. The Keplerate structure $\{Mo_{72}V_{30}\}$ – consisting of 12 pentagonal $[Mo_6O_{21}]^{6-}$ units interlinked by 30

$[V=O]^{2+}$ units – is highly dependent on the pH value of the precursor solution[76, 116, 124]. It is stable at pH values from 1.5 to 4.5, but its concentration fluctuates strongly in this range[116].

During hydrothermal synthesis a reduction-oxidation reaction between two elements in the solution takes place, enabling restructuring and subsequent transformation into a layered solid[76]. Depending on the concentration of $\{Mo_{72}V_{30}\}$ and hence the pH value of the precursor solution, different structures of the MoV oxide can be obtained. At pH values between 3.4 and 2.7 the orthorhombic M1 structure is formed[118], whereas a pH of around 2.2 results in the trigonal M1 structure. Lowering the pH even further leads to the hexagonal $Mo_{0.87}V_{0.13}O_{2.94}$. A pH value above 3.4 leads to fewer or no product at all, since the $[Mo_6O_{21}]^{6-}$ unit cannot condense at too high pH values and with that no Keplerates can be formed[124].

Additionally, to form the $\{Mo_{72}V_{30}\}$ structure, it is not important which molybdate structure is used as a precursor, for example both trimolybdate $[Mo_3O_{10}]^{2-}$ and heptamolybdate $[Mo_7O_{24}]^{6-}$ form the Keplerate as long as the pH is in the right range[118].

Adding more elements to the synthesis makes the formation process of the M1 structure more complex. When tellurium is mixed to the Keplerate containing MoV solution, the Anderson-type structure $[TeMo_6O_{24}]^{6-}$ is formed[117, 125]. Substitution of molybdenum atoms by vanadium is also likely as indicated by shifts in Raman spectra. The addition of niobium to the mixture leads to no change in the Raman spectra, but rather to precipitation[117, 125]. This four element precursor solution can be subjected to hydrothermal synthesis or evaporation treatment. However, precipitation and evaporation based synthesis routes require an additional purification step to obtain phase-pure orthorhombic M1 MoVTeNb. When niobium is added directly to the mixed MoV precursor solution, signals that can be attributed to $[MoO_2]^{2+}$, b-$[Mo_8O_{26}]^{4-}$, and $[VO_2]^{+}$ appear in ^{95}Mo- and ^{51}V-NMR spectra, but no peaks that are indicative of any structural interaction with Nb[126].

When applying hydrothermal synthesis, the material of the autoclave liner also influences the structural outcome, with Hastelloy rather leading to phase-pure catalyst precursors than Teflon[117].

Nevertheless, a comparative study showed that phase-pure M1 MoVTeNb oxide can be obtained with three different synthesis approaches (hydrothermal, precipitation-evaporation, super heated water treatment) with the only difference being the particle morphology and size of the catalyst precursor[127].

1.2.3 Thermal treatment

While the conditions of the synthesis certainly play a very important role in the formation of mixed metal oxides, the thermal treatment which takes place afterwards has an influence on the structural composition that cannot be neglected.

Four element based MoVTeNb oxide possesses usually an amorphous structure right after synthesis, irrespective of the synthesis route, and shows broad signals in x-ray diffractograms[117, 128]. If the precursor powder is then heated in an inert gas, overlapping reflexes for M1, M2 and Mo_5O_{14}-type structures arise from 390 °C on upwards. The M2 structure decomposes again at temperatures between 530 and 580 °C. Increasing the temperature further to 600 °C leads to a phase-mixture of M1, MoO_3, and Mo_5O_{14}. Again, the sensitivity of the structure is shown by in-situ heating experiments, since interactions with the sample holder led to a phase mixture, whereas the ex-situ heated precursor resulted in phase-pure M1[128]. Furthermore, if the precursor solid already shows reflexes hinting at the presence of additional phases apart from M1, no matter if mostly amorphous or already crystalline, a phase mixture consisting of M1, M2, and Mo_5O_{14}-type will be present after thermal activation[117, 127].

Thermal treatment of three element MoVTe or MoVNb oxide[126] showed that a higher crystalline precursor is more stable than an amorphous one, the latter already decomposing and partially transforming at 500 °C in N_2, while the crystalline solid only starts decomposing and forming by-phases at 600 °C[129]. Adding alkali metals like potassium to the structure during synthesis leads to decomposition of the M1 phase during thermal activation, as has been shown for the case of MoVSb oxide[130]. Also, including tungsten as the third metal element in the synthesis leads to the preferred formation of Mo_5O_{14}-type structured during thermal treatment[131, 132]. This structure forms at around 450 °C when the precursor solid is first heat treated in air and subsequently in an inert atmosphere[133]. Performing both heating steps in either air or inert atmosphere results in the early decomposition of the structure[131, 133].

MoV mixed oxide is usually quite crystalline directly after synthesis. Additional thermal activation results in the migration of vanadium ions into the heptagonal channels which are usually occupied by tellurium in the more complex MoVTeNb oxide. These vanadium ions might come from surrounding framework sites or migrate along the channels from the outside[77].

However, the local arrangement of the metals does not change from the precursor to the activated solid, i.e. heating in an inert gas-phase establishes a long-range order in the solid, and does not create the structures necessary for the desired M1 structure[125].

Subjecting these MoV based oxides to reductive or oxidative atmosphere at higher temperatures results in the simplest case of MoV in the evolution of lattice oxygen, or the incorporation of gaseous O_2, respectively[124]. The ternary Mo_5O_{14}-structured MoVW oxide is stable in 20 % oxygen atmosphere at up to 500 °C, whereas a reducing environment with 10 % hydrogen transforms the precursor mostly to MoO_2 and WO_2 at already 400 °C[132]. In comparison, the Mo_5O_{14} structure in quaternary MoVNbPd oxide remains intact at 475 °C in reducing as well as in oxidising atmosphere[134].

1.2.4 Conclusion

Polyoxometalates are the precursor species in aqueous solution for the synthesis of mixed metal oxides. They have been investigated mostly by spectroscopic techniques like Raman or UV-vis spectroscopy, and titration methods. Their presence and concentration in solution is mostly dependent on the pH value and the concentration of the metal in the solution. In general, higher concentrations and lower pH values lead to higher condensed species like octamolybdates $[Mo_8O_{26}]^{4-}$ or decavanadates $[V_{10}O_{28}]^{6-}$ made up of MO_6 octahedra.

These dependencies are part of the sensitivity of MoV mixed oxides to their synthesis conditions. Not only does the formation of the M1 phase depend highly on the pH value of the precursor solution (and with that to a certain extend on the structure of the precursor polyoxometalates), the lining of the autoclave can already make an impact. The same is the case for the reaction temperature and time. Furthermore, the thermal treatment after synthesis is also a crucial point. The right conditions have to be administered to enforce the long-range order of the desired structure instead of decomposing it.

1.3 Motivation and research questions

As has been pointed out, due to impending oil shortage in the near future, it is important to find another source of organic species which can be used to synthesise important chemical building blocks for all purposes. Simple hydrocarbons like alkanes are the perfect starting material for any desired product and are abundant in natural gas. However, a catalyst has to be developed which can surpass the high energy barrier of alkane activation and simultaneously lead to the formation of the desired product.

While mixed transition metal oxides like $MoVO_x$ and $MoVTeNbO_x$ with the orthorhombic M1 structure are promising candidates, their selectivity values are still too low to be considered for industrial applications. Since there is a strong connection between the structural composition and catalytic properties, it is of interest to develop a way of fine-tuning the oxide structure to yield higher selectivity.

The structure, in return, is influenced by synthesis and thermal treatment parameters. Hence, the right synthesis conditions have to be found for the respective M1 oxide catalyst and the respective catalytic reaction. Polyoxomolybdates and –vanadates are precursors during synthesis and their structure is easily tuneable. Formation of the precursor oxide in aqueous solution as well as the crystallisation of the final M1 structure have been investigated, but one step of the whole synthesis procedure has not been examined so far.

The desolvation process occurring during drying after synthesis and before thermal activation equates an increase of POM concentration and might with that influence the structural species present in the not yet activated precursor. A suitable technique for the investigation of this process is electrospray ionisation (ESI) mass spectrometry. During ionisation, the solvent is evaporating which mimics a change in concentration and pH value.

One aim of this work is to examine whether ESI-MS can be applied as another technique to investigate the speciation of polyoxometalates in aqueous solution, the condensation mechanism after the removal of the solvent, and deliver new insights due to its extraordinary sensitivity to small concentrations. Furthermore, it is of interest to determine the effect of synthesis parameters like pH value, metal concentration, and trace substitution of vanadium on the catalytic outcome in the ODH of ethane and propane.

2. Experimental

2.1 Preparation of aqueous metalate solutions

2.1.1 Molybdate solutions

Ammonium heptamolybdate tetrahydrate ($(NH_4)_6Mo_7O_{24} \cdot 4\ H_2O$, Carl Roth, >99 %) was dissolved in Milli-Q water to give molybdate solutions with Mo concentrations of 0.35 M, 35 mM, 7 mM, 0.7 mM, and 0.07 mM. 20 mL of these solutions were then either titrated with 5 % diluted nitric acid or 3 % diluted ammonia to attain pH values from 2 to 9 in steps of 1, respectively. All solutions were examined via mass spectrometry, Raman spectroscopy, ATR spectroscopy and UV/vis spectroscopy.

2.1.2 Vanadate solutions

Ammonium metavanadate ($(NH_4)VO_3$ (MERCK, p.a.) was dissolved in Milli-Q water to give vanadate solutions with V-concentrations of 10 mM, 5 mM, 1 mM, and 0.1 mM. 20 mL of these solutions were then either titrated with diluted nitric acid or diluted ammonia to attain pH values from 2 to 9 in steps of 1, respectively. All solutions were examined via mass spectrometry, Raman spectroscopy, ATR spectroscopy and UV/vis spectroscopy.

2.1.3 Molybdovanadate solutions

Aqueous solutions with different Mo/V ratios and overall metal concentrations were prepared with the concentrations shown in Tab. 2.1

Table 2.1: Concentration of Mo and V for different molybdovanadate solutions.

Overall metal concentration / mM	metal	Mo/V ratio			
		0.33	1	3	4
250	Mo	62.5	125.0	187.5	200.0
	V	187.5	125.0	62.5	50.0
43.75	Mo	10.94	21.875	32.81	35.00
	V	32.81	21.875	10.94	8.75
8.75	Mo	2.19	4.375	6.56	7.00
	V	6.56	4.375	2.19	1.75

Ammonium heptamolybdate tetrahydrate was used as molybdenum source, whereas for vanadium vanadylsulphate pentahydrate as well as ammonium metavanadate were used, leading to 24 solutions in total. For comparability, all solutions were adjusted with diluted nitric acid to a pH value of 2.8, which is the pH value of the precursor solution used in hydrothermal $(MoV)O_x$ synthesis. All solutions were examined by mass spectrometry and Raman spectroscopy.

2.2 Analysis of metalate solutions

2.2.1 Ion Mobility Electrospray ionisation mass spectrometry & Infrared Multiple Photon Dissociation

Mass spectrometric measurements were performed with a GS-2 nano-electrospray ionisation (nESI) quadrupole mass spectrometer by Waters, including an ion mobility cell. Mass-to-charge ratios from 50 to 2000 were recorded in negative ion mode with an applied capillary voltage of –1.0 kV and a cone voltage of –60 V. The source offset was set to 25. The ion mobility cell was filled with He gas at a pressure of 2.2 Torr, and the following voltages were applied: -40 V IMS DC Entrance, 50 V Helium DC Entrance, -40 V Helium Exit, and 50 V IMS Bias.

To find the most suitable parameters for measurements, chosen parameters were changed one at a time. The capillary voltage was varied in the range from -0.5 kV to 1.4 kV, the cone voltage from -60 V to -20 V, and the Helium pressure from 1.6 Torr to 2.2 Torr.

For even softer ionization conditions, a home-built dirft-tube quadropole time-of-flight mass spectrometer was applied, which is also used for infrared multiplie photon dissociation (IRMPD) spectroscopy. Herein, the sample solution is electrosprayed with a spray voltage of –1.0 kV (negative ion mode) and the generated anions are transferred into a home-built drift tube-ion mobility-mass spectrometer. A schematic diagram of the instrument is given in following Fig. 2.1.

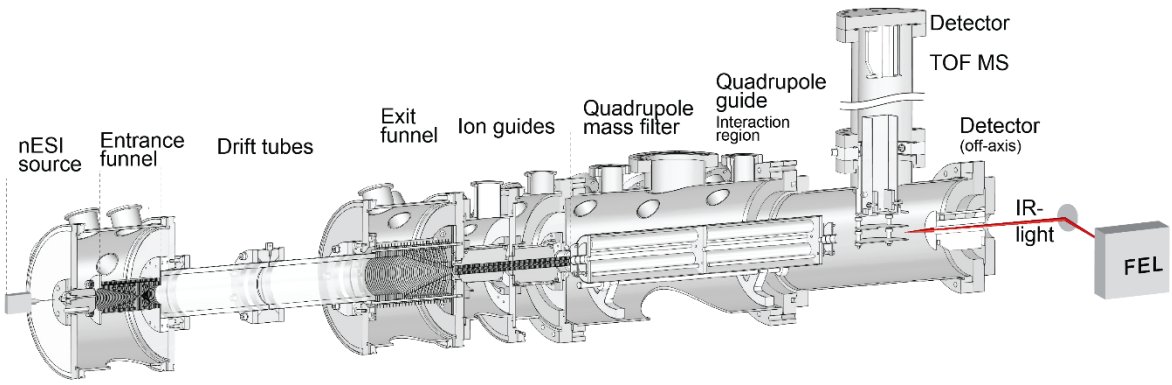

Fig. 2.1: A home-built drift-tube (DT) quadrupole time-of-flight (Q-TOF) mass spectrometer equipped with nanoelectrospray ionization (nESI) source.

Metal oxide (vanadium or molybdenium oxide) anions generated nESI are initially collected in an entrance RF ion funnel. Then, ions are pulsed with 20 Hz repetition rate into a 80 cm-long drift tube filled with helium buffer gas (4–5 mbar), in which ions traverse the drift tube under the influence of a weak electric field (10–15 Vcm^{-1}). with a drift velocity depending on their size-to-charge ratio. At the end of the drift tube, the mobility-separated ions are transported into the high vacuum region by an exit RF ion funnel. The *m*/*z* selection is done in the first quadrupole, and then the time-dependent ion current is measured at the off-axis detector to obtain an arrival time distribution (ATD) which is further used to determine the collision cross-section.

IRMPD spectroscopy. A narrow ATD slice (100-μs width) is selected by electrostatic gating at the end of the ion guides, and then *m*/*z*-selection is done for the ions in the ATD slice. The ion mobility- and *m*/*z*-selected ions are then irradiated by intense IR pulses (pulse width 7–8 μs) provided by the Fritz Haber Institute free-electron laser (FHI FEL). When the IR wavelength is on resonance with an IR mode of the ion, the absorption of multiple photons can take place and dissociation can occur. The fragment ions as well as the precursor anion are monitored using a time-of-flight (TOF) mass analyzer (see Figure 1). The IR spectrum is constructed by plotting fragmentation efficiency as a function of IR wavenumber. The fragmentation efficiency (*Y*) at the specific wavenumber ($\tilde{\nu}$) is determined by following equation 1, where I_p and I_f are wavenumber-dependent abundances of the precursor and the fragment ions, respectively. *P* is the pulse energy of IR photons.

$$Y(\tilde{\nu}) = -\log\left\{\frac{I_p(\tilde{\nu})}{I_p(\tilde{\nu}) + \sum I_f(\tilde{\nu})}\right\}\frac{1}{P(\tilde{\nu})} \qquad (1)$$

IR spectra are obtained by scanning the laser in 3 cm−1 steps in the range 700–1100 cm^{-1}, averaging 30–100 mass spectra (depending on the signal intensities of fragment ions) per wavenumber step and plotting the fragmentation efficiency as a function of wavenumber.

2.2.2 Raman spectroscopy

For Raman measurements, an immersion probe with a wavelength of 785 nm was used (Kaiser optical systems, RamanRxn System, immersion optic ¼"OD (HC-276)). Depending on the concentration of the solution, the illumination time ranged from one minute to 10 minutes.

2.2.3 UV-vis spectroscopy

UV-vis measurements were done with a PerkinElmer Lambda 650 UV/vis spectrometer with an Hg- and deuterium lamp and recorded from 200-800 nm with the software PerkinElmer UV WinLab. An UV-transparent quartz cuvette with a thickness of 0.01 mm (Hellma Analytics) was used. Milli-Q water in and identical cuvette served as reference.

2.3 Density functional theory calculations

Density functional theory calculations have been carried out in collaboration with the Molecular Physics department, in particular Dr. Mateusz Marianski.

2.3.1 Collision cross sections and infrared multiple photon dissociation spectra

The calculations have been performed with the all-electron numeric atom-centered orbitals code FHI-aims[135] using the generalized gradient approximation exchange-correlation PBE functional[136] augmented with the Tkatchenko-Scheme[137] scheme (vdW^{TS}) to correct for longrange van der Waals interactions. The geometry optimizations were carried out with tight basis set settings. The harmonic vibrations calculations were performed numerically by displacing each atom by 0.0025 Å in each direction followed by the digitalization of the resulting hessian. 3N-6 positive frequencies confirmed that all optimizations yielded stable minima.

The ab initio molecular dynamics simulations were performed with the FHI-aims code using PBE exchange-correlation functional augmented with vdW^{TS} to account for longrange dispersion. The simulations were carried out with light basis set. The trajectories were simulated for 10 ps with 1 fs time step at 300K using a stochastic velocity rescaling thermostat.[138] The anharmonic spectra were derived using a fortran program as outlined in Rossi et al.[139]

The transition state between minima in Mo_4O_{13} were found using the string method[140] followed by climbing image approach as it is implemented in the aimsChains tool.

2.3.2 Raman spectra

The interpretation of Raman measurements is supported by density-functional theory (DFT) calculations carried out in Gaussian09 software[1]. Molecular clusters were first optimized using general-gradient approximation PBE[2] functional in def2-TZVP[3] basis set and Raman spectra were derived using harmonic approximation. We previously observed that PBE functional yields geometries, energetics as well as theoretical spectra of small negatively charged molybdenum oxide clusters in a good agreement with experimental data[4, Mateusz' paper]. Presented calculations were performed in the gas phase, as comparison with polarizable continuous solvation models showed only systematic redshifts. Hepta- and octamolybdates in high charge states have been partially protonated to render the structures stable. All vibrations are shown unscaled and were broadened by 10 cm^{-1} gaussian.

2.4 Synthesis of mixed $(MoV)O_x$

A solution of 114.75 g ammonium heptamolybdate tetrahydrate (0.65 mol Mo) and 2,875 g Milli-Q water and a solution of 41.25 g vanadylsulphate pentahydrate (0.17 mol V) and 375 g Milli-Q water were filled into a 6 litre autoclave reactor setup with integrated stirrer (Premex Reactor AG, Fig. 2.2). All remaining air in the vessel and in the precursor solution was replaced by N_2 (Westfalen) under constant stirring at 100 rpm until the pressure in the reactor remained constant for ten minutes. After the excess pressure was vented from the vessel, the reaction mixture was stirred at 100 rpm and heated to 200 °C at 1 °C/min and the temperature was held for 17 hours. After cooling down to room temperature, the resulting solid was filtrated with a no. 4 glass frit, washed twice with Milli-Q water, and dried at 80 °C for two nights. On average, 80 g of a black solid were obtained, which corresponds to a yield of 91 % based on the molar mass of Mo_3VO_{11}.

The 14 g of the black solid was washed with 0.25 M oxalic acid (25 mL per 1 g solid) under continuous stirring at 60 ° C for 30 minutes to remove amorphous parts. Afterwards the suspension was filtered with a no. 4 glass frit and washed twice with Milli-Q water, before drying in air at 80 °C over night. On average, 4 g (29 % yield compared to amount before washing) remained.

The remaining material was heated to 40 °C in a continuous argon flow of 100 mL/min in a rotating furnace vessel made of quartz. After 3 hours, the furnace was heated to 400 °C with 15 °C/min and stayed at that temperature for 2 hours.

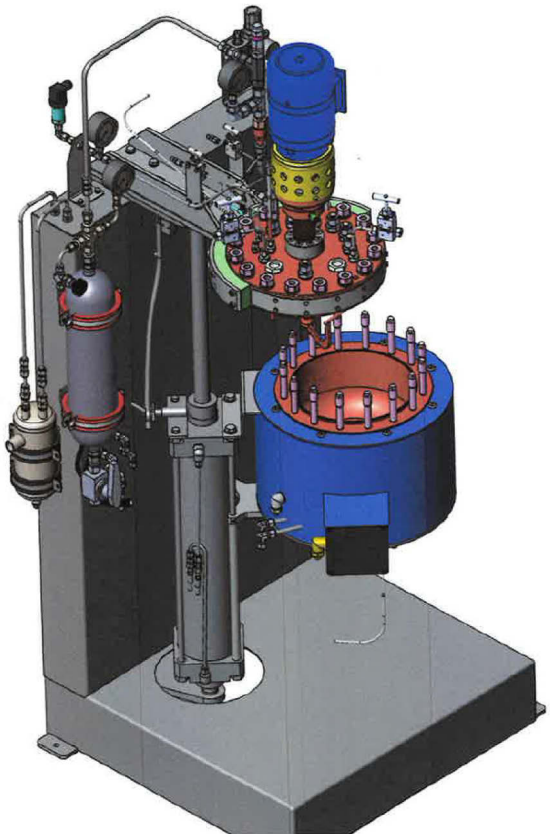

Fig. 2.2: Premex autoclave setup with integrated Raman probe, pH control, and stirrer.

These experiments were repeated with lower concentrations of molybdenum and vanadium as follows in Tab. 2.2.

Table 2.2: Chemical amount of Mo and V for diluted (MoV)O_x and the corresponding yield.

	Dilution I (#26672)	Dilution II (#26562)	Dilution III (#26732)	Dilution IV (#26578)
***c*(Mo) / mmol**	113.75	26	22.75	0.325
***c*(V) / mmol**	28.44	6.5	5.69	0.081
yield	10.24 g / 69.8 %	-	0.01 g / 0.4 %	< 0.01 g / < 0.4 %

2.5 Synthesis of transition metal substituted (MoV)O_x

Solutions of 3.53 g AHM (20 mmol Mo) in 20 g of Milli-Q water, 1.24 g $VOSO_4$ pentahydrate (4.95 mmol V) in 20 g Milli-Q water, and 0.05 mmol (if not stated otherwise) of a third chosen metal in 10 g of Milli-Q water were prepared. The chosen transition metals, the used chemical compounds and the corresponding amount used are found in Tab 2.3.

Table 2.3: Transition metals used in the hydrothermal synthesis of substituted (MoV)O_x and their corresponding amount used.

metal	Used chemical compound	Amount in 10 g dist. water
titanium	$TiOSO_4 \cdot 2\ H_2O$	9.8 mg
manganese	$MnSO_4 \cdot H_2O$	8.5 mg
cobalt	$CoSO_4 \cdot 7\ H_2O$	14.0 mg
zinc	$ZnSO_4 \cdot 7\ H_2O$	14.4 mg
tellurium	$Te(OH)_6$	11.5 mg
chromium	$Cr_2(SO_4)_3 \cdot H_2O$	9.8 mg
arsenic	As_2O_3	5.0 mg

For each synthesis run, each molybdate, vanadate, and transition metal solution was prepared four times. In one quartz vessel, one molybdate, vanadate, and transition metal solution was filled each, leading to four vessels, each filled with 50 mL of MoVM precursor solution. These vessels were mounted into a Multiwave PRO microwave reactor setup by Anton Paar according to instructions. The solutions were heated from room temperature to 240 °C in 22 minutes under constant stirring and remained at that temperature for 2 hours before cooling down again. The four acquired black-purple suspensions were centrifuged for 10 minutes at 6000 rpm, the excess solution was decanted and the solid washed with Milli-Q water. This process was repeated two more times, whereas the last centrifugation took place at 3600 rpm for 30 minutes. The remaining solids were dried in air at 80 °C over night.

2.6 Analysis of solid catalysts

2.6.1 X-ray diffraction

The X-ray diffraction (XRD) measurements were performed in Bragg-Brentano geometry on a Bruker AXS D8 Advance II theta/theta diffractometer, using Ni filtered Cu $K\alpha_{1+2}$ radiation and a position sensitive energy dispersive LynxEye silicon strip detector. The sample powder was filled into the recess of a cup-shaped sample holder, the surface of the powder bed being level with the sample holder edge (front loading).

XRD Data were evaluated by whole powder pattern fitting according to the Rietveld method as implemented in the TOPAS software [version 5, copyright 1999-2014 Bruker AXS].

2.6.2 X-ray fluorescence

Up to 100 mg of sample are mixed up with 8.9 g of Dilithiumtetraborate (LTB), purchased from FLUXANA, high purity grade and molten in a Pt/Au crucible at around 1300 °C. The melt is poured into molds, although Pt/Au, to form glass disks of 40 mm diameter.

The XRF instrument is a wavelength dispersive device *S4-Pioneer*, derived from BRUKER-AXS. The radiation source is a tube with Rh-anode operated with maximum 60 kV and 4 kW. The exiting radiation can by filtered optionally with different Al, Cu and Mo filters to cut of Compton and Raleigh scattering of the characteristic (Rh) part. The signal is detected by a scintillation counter in the lower energy range (up to 10 keV) and a flow-counter in the upper range. The tube-current is automatically adapted to the intensity to avoid detector saturation and dead-time problems.

The instrumental energy resolution depends on the collimator and the crystal – with LiF 200 and the 0.23° collimator the resolution is about 380 eV at 17.5 keV (Mo Kα).

Amount of a given element is calculated by iteration following the Lachance-Traill formalism based on peak-high intensity; background correction is done by 2-point linear fitting.

The glass specimen are picked up by an autosampling system of the XRF instrument and measured in vacuum. The sample is rotated with a frequency of 0.5 min^{-1} during measurement.

For a multi-element problem the parameter space is reduced for calibration. A balance point composition close to the assumed sample composition is defined. For a set of calibration standards, the concentration of one element is varied around this center, the ratio of all other elements kept constant.

The calibration factors are calculated by linear regression, plotting the α-corrected intensities (Lachance-Traill) versus chemical concentration in the calibration standards. Normally, intercept and α are not fixed but optimized and calculated from the regression routine.

2.6.3 BET measurements

The samples have been pretreated in 9 mm measuring cells with an external heating station (Autosorb Degasser, Quantachome). Herein, the samples have been heated *in vacuo* to 200 °C, kept for two hours at this temperature, and then cooled down to room temperature. Afterwards it was tested if the samples might still degas., before weighing them. A filling rod was used to reduce the volume during measuring.

To determine the BET (Brunnauer, Emmett, Teller) surface area, a fully automatic volumentric sorption apparatus (AUTOSORB-6B-MP, Quantachrome) was applied. A nitrogen isotherm was recorded at 77 K with 11 points in the relative pressure range p/p_0 = 0.05-0.3 (DIN Norm: DIN-ISO 9277).

2.6.4 Transmission electron microscopy and energy dispersive X-ray spectroscopy

Aberration-corrected scanning transmission electron microscopy (STEM) was performed on a JEM-ARM200F microscope with CEOS CESCOR and CEOS CETCOR hexapole aberration correctors for probe and image forming lenses, respectively, and a cold field emission gun (CFEG). STEM images were recorded with a JEOL annular dark-field (ADF) detector. Prior to the measurements, the powdered material was dry deposited on a carbon coated copper TEM grid. Prior to the ADF-STEM analysis some particles were oriented along the crystallographic c-axis.

The elemental analysis was performed using a high angle silicon drift EDX detector with the solid angle up to 0.98 steradians from a detection area of 100mm^2. EDX maps and spectra were collected using Gatan Digital Micrograph software.

2.6.5 Scanning electron microscopy

The Hitachi S-4800 is a semi-in-lens Scanning Electron Microscope (SEM) and working with a cold field emission gun. The acceleration voltage can be changed from 0.1 kV to 30 kV. The SEM is equipped with an upper and a lower secondary electron (SE) detector, a YAG back scattered electron (BSE) detector, a transmitted electron (TE) detector and an EDX detector (QUANTAX 800 with XFlash® 6 (Bruker)). Its maximum resolutions are 1.4 nm at 1 kV, 1.0 nm at 15 kV, and at 30 kV in STEM mode. The probe current varies between 1 pA and 1 nA.

The MoV based oxide samples were measured at 1.5 kV with a working distance of 3.0 mm and magnifications between 1500 and 150000.

2.7 Catalytic tests of transition metal substituted (MoV)Ox

Of each sample batch one sample was chosen for catalytic testing in oxidative dehydrogenation of ethane and propane. A setup for partial oxidation with eight parallel reactors – all equipped with thermocouples – was used. The catalyst was pressed and sieved to obtain particles in the size between 100 and 200 µm. 200 mg of the catalyst were filled into the reactor and diluted with SiC.

Two different gas feed compositions were applied: (1) 10:5:85 ethane/O_2/N_2, and (2) 10:10:80 ethane/O_2/N_2, while the temperature was changed in steps of 10 °C from 200 °C to 290 °C. The total flow was 20 mL/min for all experiments and the catalytic performance was determined at steady state conditions and atmospheric pressure.

For gas analysis, an online gas chromatograph (Agilent 7890A) was used. To analyse the permanent gases CO, CO_2, N_2, O_2, and CH_4, a combination of Plot-Q (length 30 m, 0.53 mm internal diameter, 40mm film thickness) and Plot-MoleSieve 5A columns (30m length, 0.53 mm internal diameter, 50mm film thickness), connected to a thermal conductivity detector (TCD) was used.

3. Speciation of molybdates in aqueous solution and gas-phase

To investigate the influence of the POM speciation on the synthesis of MoV oxide, the speciation of molybdates in aqueous solution at various molybdenum concentrations (350 mM – 0.07 mM) and pH values (2-9) has been examined by Raman and UV-vis spectroscopy. The gas-phase composition has been investigated with electrospray ionisation mass spectrometry, while simultaenously the collision cross sections of the singled out molecules have been derived from the measurements via ion mobility spectroscopy. For more structural insights, infrared multiple photon dissociation (IRMPD) experiments have been performed and the structures in the gas-phase have been calculated in accordance with the IRMPD spectra. These molybdenum concentrations were chosen based on the standard hydrothermal synthesis route, in which the Mo concentration ranges usually around 200 mM. Hence, values above and below 200 mM were used. Furthermore, since these aqueous solutions have been investigated in regard to the synthesis following in chapter 6, no additional salts were added to the solution as it is done in literature to keep at constant ion strength.

3.1 Molybdate species in aqueous solution

3.1.1 Raman spectroscopy

Aqueous solutions of molybdate species have been investigated in literature[93, 141-143] and the band assignments of different species are widely known. To compare the Raman spectra of the solutions studied by MS with the literature, Raman spectra of all samples with a Mo concentration of 7 mM and higher were measured with an immersion probe. For lower concentrations, either the signal to noise ratio was too low, or no signal at all was received.

At a concentration of 350 mM Mo, various species are present depending on the pH of the solution (Figure 3.1). Low pH values lead to a single outstanding signal at 895 cm^{-1}, which then is joined by a second one at pH 6. The single signal is attributed to the Mo-O stretching vibration of monomolybdate $[MoO_4]^{2-}$, whereas this signal together with the one at 939 cm^{-1} (asym. stretching of Mo=O) indicates the presence of heptamolybdate $[Mo_7O_{24}]^{6-}$[143]. This signal shifts to a higher wavenumber of 946 cm^{-1} at pH 4, which has been applied to the formation of trimolybdate $[Mo_3O_{10}]^{2-}$ by Himeno et al.[143]. However, based on the distribution diagrams mentioned in previous chapters, said species has not been

detected by various other methods. Instead, it is more plausible that this shift is due to the protonation of heptamolybdate, since this is an inevitable step in the condensation reaction to octamolybdate. The spectra at pH 3 and 2 show signals at 956 and 969 cm^{-1} arise, which are attributed to α- and β-$[Mo_8O_{26}]^{4-}$, respectively[143]. The presence of a-octamolybdate is however not conclusive. On one hand, this species is claimed to be not present in aqueous media, on the other signals around 956 cm^{-1} are widely attributed to the Mo=O vibration of it when found in aqueous molybdate solutions. Hence, there is no clear evidence so far to what species exactly this dominant signal belongs to. The signal at 910 cm^{-1} also belongs to these two species. The signal at 846 cm^{-1} on the other hand, may signal the formation of the supramolecular $[Mo_{36}O_{112}]^{8-}$ molecule[97].

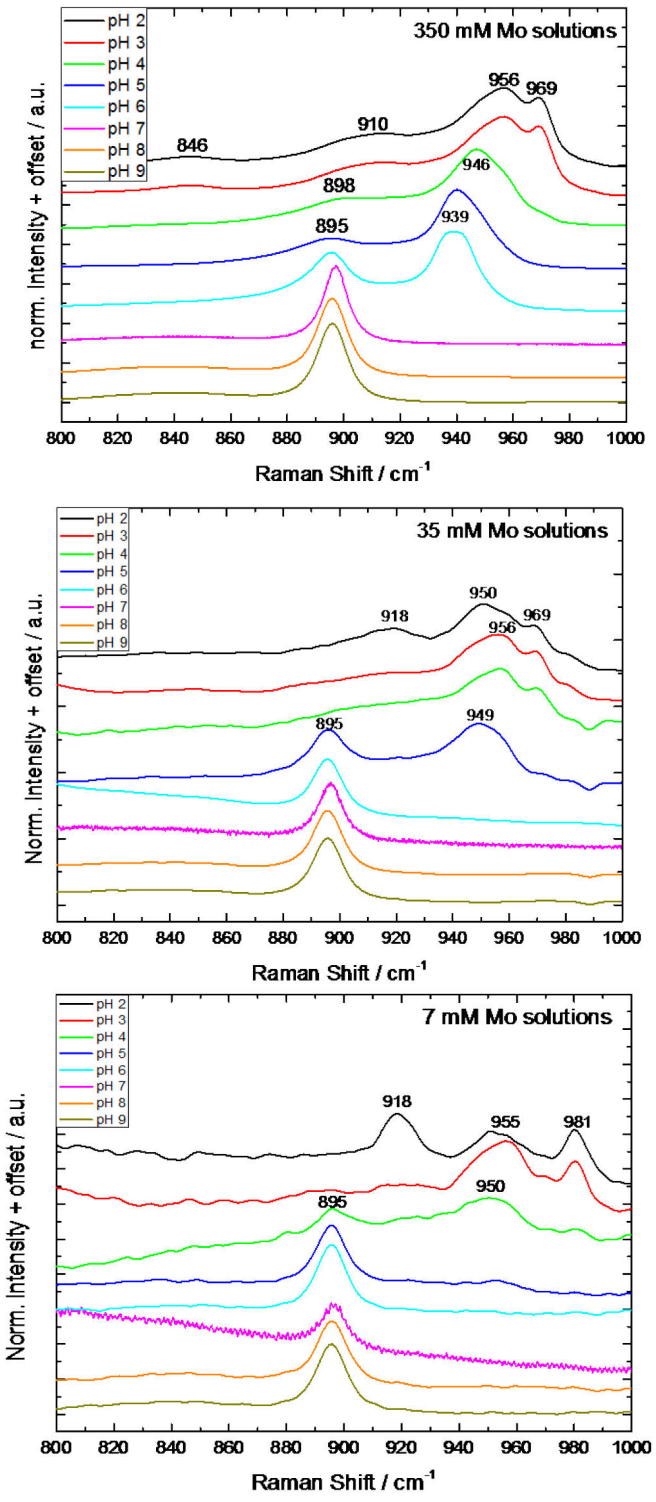

Figure 3.1: Raman spectra of the concentration series 0.35 M, 35 mM and 7 mM in distilled water, depending on their pH value.

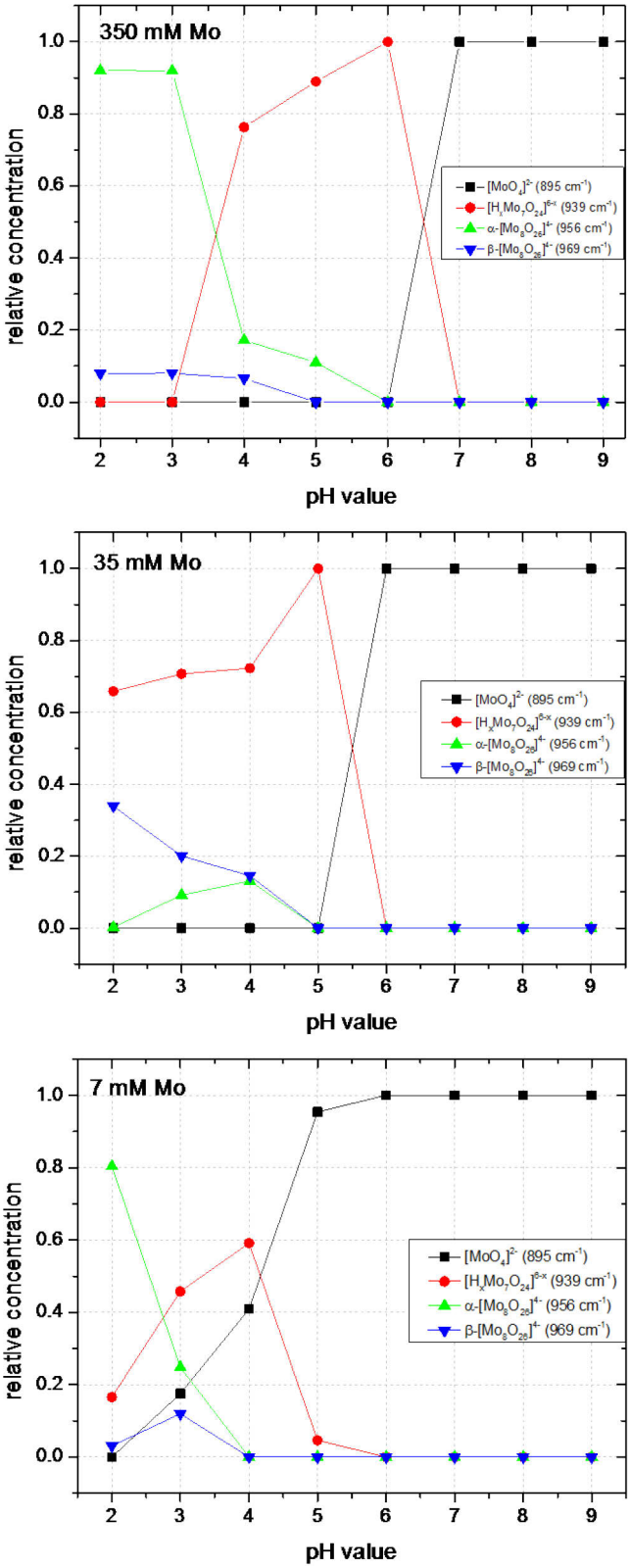

Fig. 3.2: Relative concentrations of molybdate species in aqueous solution depending on the pH value from spectral deconvolution of Raman measurements.

For the spectra with a tenfold lower molybdenum concentration, the change from monomolybdate to a higher molecular species sets in with pH 5, at which pH value the signal for protonated $[Mo_7O_{24}]^{6-}$ appears at 949 cm^{-1}. Lowering the pH of the solutions further leads to the aforementioned signals of α- and β-$[Mo_8O_{26}]^{4-}$, which stay present from pH 4 to pH 2.

Raman spectra of solutions with 7 mM molybdenum show monomolybdate to be present as major species down to a pH value of 4, where again the signal for trimolybdate $[Mo_3O_{10}]^{2-}$ arises. Decreasing the pH value to pH 2, leads first to a shift from 950 cm^{-1} to 955 cm^{-1}, indicating the presence of octamolybdate, and a new signal at 981 cm^{-1}, then also to an increase of the signal at 918 cm^{-1}.

Relative amounts of the aforementioned molybdate species corresponding to Fig. 3.1 can be found in Fig. 3.2. The relative amounts of the species were derived from the experimental data under the assumption of identical scattering cross-sections of all species.

Tab. 3.1: Detected Raman signals in 350-0.07 mM Mo aq. solution and their respective assignments based on [143] and [144].

Signal / cm^{-1}	Vibration	Species
846		$[Mo_{36}O_{112}]^{8-}$
895	ν_s(Mo-O_t)	$[MoO_4]^{2-}$
		$[Mo_7O_{24}]^{6-}$
910-918	ν_{as}(Mo-O_t)	$[Mo_8O_{26}]^{4-}$
939	ν_{as}(Mo=O)	$[Mo_7O_{24}]^{6-}$
946-950	ν_{as}(Mo=O)	$[Mo_3O_{10}]^{2-}$
956	ν_{as}(Mo=O)	$[Mo_8O_{26}]^{4-}$
969	ν_{as}(Mo=O)	$[Mo_8O_{26}]^{4-}$

Comparing these experimental data with the known distribution diagrams mentioned in chapter 1, it is again shown that different methods can lead to slightly different speciation distributions. Octamolybdate is accounted as the predominant species at low pH values in our measurements, which has also been documented by ^{95}Mo NMR spectroscopy[4] and calculations based on formation constants[5]. The appearance of protonated heptamolybdate is supported by potentiometric data[1] and NMR spectroscopy[4] as well. Hence, the acquired Raman data resemble a combination of the different distribution diagrams already known.

3.1.2 UV-vis spectroscopy

UV-vis spectroscopy is a useful tool to discriminate between the immediate coordination environment of an atom. The wavelength of the charge transfer between different atoms is hence dependent on the number and position of the surrounding. In the case of molybdates, this allows to determine the presence of either {MoO_4} tetrahedra or {MoO_6} octahedra in the present species.

The presence of various species creating an overlayer effect can complicate UV-vis measurements drastically, but also the protonation state can make a difference as Ozeki et al. showed in the case of monomolybdate[5]. Therein, the maxima of UV-vis spectra of 0.03 mM molybdate solution changed from 208 and 232 nm for unprotonated $[MoO_4]^{2-}$ to 215 and 242 nm for $[HMoO_4]^-$, and lastly 225 nm with a shoulder at 235 nm for H_2MoO_4.

Our measured spectra are shown in Fig. 3.3 for all concentrations and pH values. The spectra at the highest concentration show clear changes in signals when increasing the pH value of the solution. At pH 2 the maximum absorbance is at 200 nm (or just below) and a shoulder is present at 247 nm. Increasing the pH to 3 leads to another additional shoulder at 290 nm. These three signals stay present up until a pH value of 6, whereas the latter one might be attributed to heptamolybdate, as it should be present according to Raman spectra and only slowly appears after increasing the pH value to 3 and more. The signals for pH values from 7 to 9 at 208 and 233 nm are clearly indicative of deprotonated $[MoO_4]^{2-}$ like Ozeki et al. postulated[5].

Decreasing the molybdenum concentration leads to a lower signal to shoulder ratio at pH 2, but both signals at 201 and 246 nm are still present like at 350 mM. At pH 3 however, only the signal at roughly 200 nm remains, while at higher pH values the shoulder reappears and then shifts from 246 to 233 nm at pH 5, where it stays until pH 8. From pH 5 to 8 the signal at 200 nm also shifts to 208 nm. The spectra at pH 9 looks presumably like the one before, just shifted to lower wavelengths. The reason for this is unclear. Taken this assumed shift into account, monomolybdate $[MoO_4]^{2-}$ is the dominant species in the pH range from 6 to 9, but the broadening of the signal at 234 nm in the direction of higher wavelengths might also indicate the presence of protonated $[HMoO_4]^-$ at neutral pH[5].

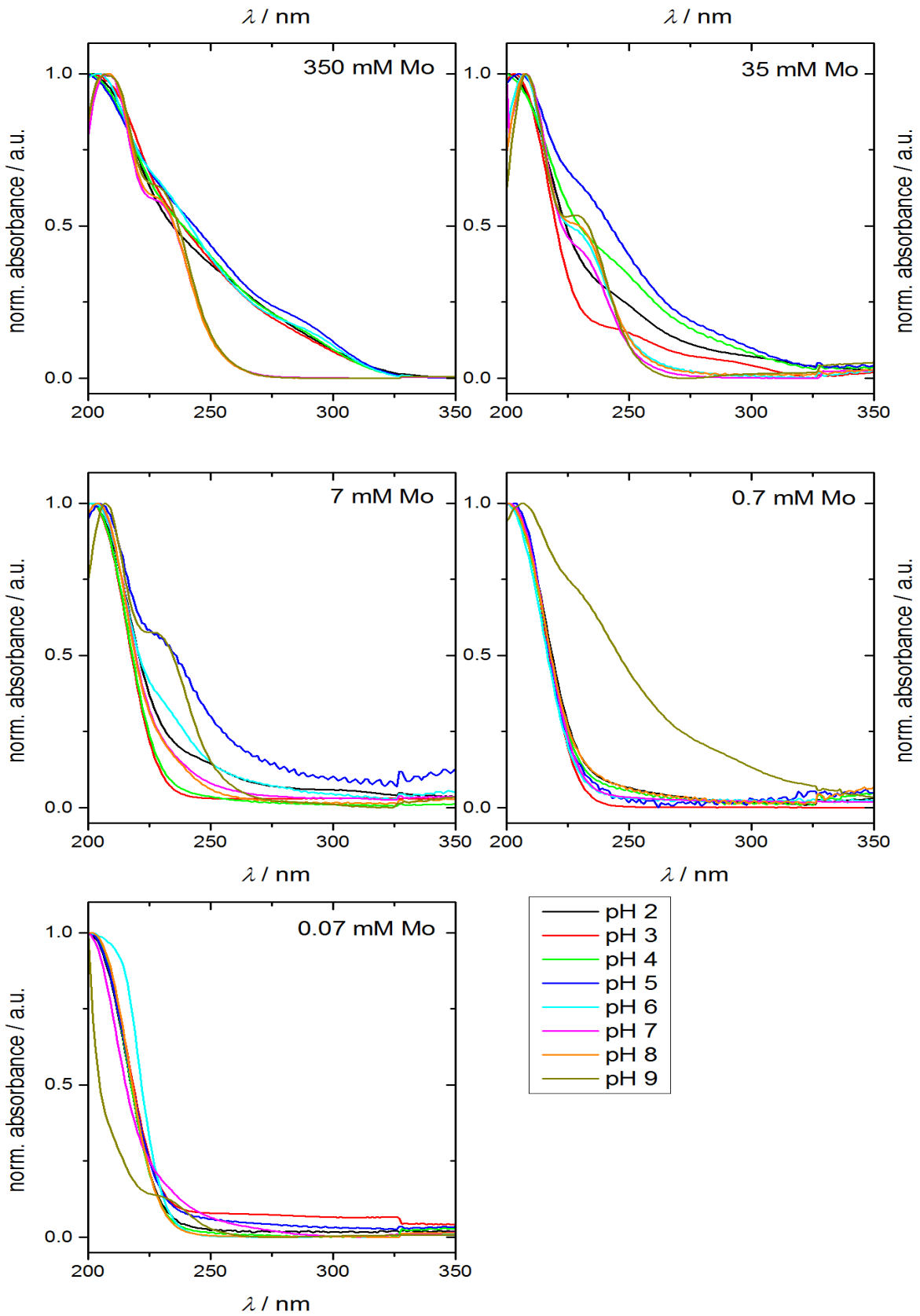

Fig. 3.3: UV-vis spectra of different molybdate solutions, sorted by Mo concentration and pH value.

With decreasing molybdenum concentration, the spectra start to show less variation in signals. Spectra of the samples with a concentration of 7 mM, for instance, are all showing peaks in the range of 200 and 205, in some cases an additional shoulder at 248 nm (pH 2) or 234 nm (pH 5 and 6, maybe also pH 9). The latter can be classified as deprotonated monomolybdate, whereas the signal at 248 nm might coincide with $[HMoO_4]^-$, which makes sense at this low pH value. The two lowest concentrations can be summed up at once: in all cases there is only monomolybdate present, classified by signals at around 201 nm and in single cases 235 nm (pH 9 at both 0.7 mM and 0.07 mM), and 247 nm (pH 2, 0.07 mM).

Comparing this speciation profile with the ones created by Raman spectroscopy, shows an almost complete agreement between these three methods regarding the presence of monomolybdate in certain concentration and pH regions, not taking into account the protonation state. For high concentrations and low pH values the signals in spectra cannot be assigned unambiguously, since there are few UV-vis studies of molybdates in aqueous solution which, in addition, claim different results. Pungor et al. classified signals at 220 and 225 nm to belong to octamolybdate $[Mo_8O_{26}]^{4-}$, and a broad signal at 213 nm to belong to heptamolybdate $[Mo_7O_{24}]^{6-}$[145]. Wang et al. on the other hand, synthesised octamolybdate with different organic cations and attributed broad signals in the range of 230 to 310 nm to this species, which might explain the signal at 290 nm that is apparent in the 350 mM spectra[146]. It might also be attributed to heptamolybdate $[Mo_7O_{24}]^{6-}$, which possesses bands at 225, 275 and 303 nm according to Ashley et al[147]. However, these results belong to a solid sample of ammonium heptamolybdate and can therefore not be related to the aqueous solution with complete certainty.

A recent study by P.C.H. Mitchell suggests that independent of the solid species, in aqueous solution only monomolybdates of various protonation states are present[148]. Albeit, this is in strong disagreement with Raman and IR studies and furthermore does not explain the signal at 290 nm in our studies.

An overview of the measured signals and their assignments is shown in Tab. 3.2.

Tab. 3.2: Detected UV-vis signals of O^{2-} → Mo^{6+} charge transfers in 350-0.07 mM molybdenum aq. solution and their assignments.

λ / nm	Species	Reference
200-208	$[MoO_4]^{2-}$	[5]
213	$[Mo_7O_{24}]^{6-}$	[145]
220-225	$[Mo_8O_{26}]^{4-}$	[145]
233-235	$[MoO_4]^{2-}$	[5]
246-248	$[HMoO_4]^{-}$	[5]
275	$[Mo_7O_{24}]^{6-}$	[147]
290	$[Mo_8O_{26}]^{4-}$	[146]
303	$[Mo_7O_{24}]^{6-}$	[147]

In conclusion, the spectroscopic measurements of the aqueous molybdate solutions agree very well with the known literature. For concentrations of 350 and 35 mM, this means that at pH values from 9 to 7, and 9 to 6, respectively, monomolybdate and its protonated derivatives are the dominant species. Decreasing the pH value leads to the speciation of $[Mo_7O_{24}]^{6-}$ in both cases, with heptamolybdate being present down to pH 4 at 350 mM and to pH 3 at 35 mM. The remaining solutions with pH values of 2 or 2 and 3 are mostly dominated by octamolybdate.

3.2 Molybdate species in the gas-phase

The molybdates present in aqueous solution are transferred into the gas-phase by evaporating the solvent. This is achieved via electrospray ionisation in the mass spectrometer, followed by transport through high vacuum to the detector.

3.2.1 Mass spectrometric measurements

Mass spectra of every sample show more than just one m/z signal, indicating that there are more than one molybdate species present at any pH value and concentration. In a typical solution, a wide variety of molybdates and their protonated forms can be detected: monomolybdates $[MoO_3]^-$ (m/z 145) and $[HMoO_4]^-$ (m/z 162), dimolybdates $[Mo_2O_7]^{2-}$ (m/z 151) and $[HMo_2O_7]^-$ (m/z 304), trimolybdates $[Mo_3O_{10}]^{2-}$ (m/z 223) and $[HMo_3O_{10}]^-$ (m/z 448), tetramolybdates $[Mo_4O_{13}]^{2-}$ (m/z 296) and $[HMo_4O_{13}]^-$ (m/z 592), pentamolybdates $[Mo_5O_{16}]^{2-}$ (m/z 367) and $[HMo_5O_{16}]^-$ (m/z 734), hexamolybdates $[Mo_6O_{19}]^{2-}$ (m/z 440) and $[HMo_6O_{19}]^-$ (m/z 880), heptamolybdate $[Mo_7O_{22}]^{2-}$ (m/z 511), octamolybdate $[Mo_8O_{25}]^{2-}$ (m/z 583), nonamolybdate $[Mo_9O_{28}]^{2-}$ (m/z 656) and decamolybdate $[Mo_{10}O_{31}]^{2-}$ (m/z 728), all shown in Fig. 3.4. These species can be summed up in to series, namely the protonated $[HMo_mO_{3m+1}]^-$ and the de-protonated $[Mo_mO_{3m+1}]^{2-}$ series, whereas the protonated species can only be found up to m = 6.

This deviates from the findings of Walanda et al.[149], who were the first to investigate the mass

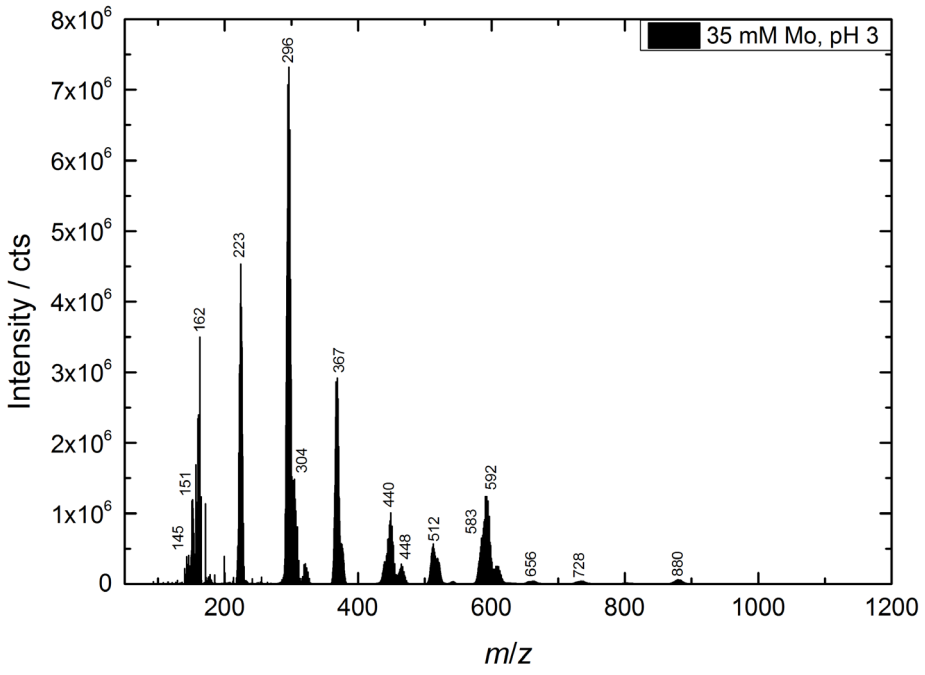

Fig. 3.4: Mass spectrum of 35 mM molybdate solution at pH 3.

spectra of aqueous molybdate solutions without any additional salts to keep the ionic strength constant. During their examination of molybdate solutions with the pH value of 4.5 and 6, they found not only the aforementioned deprotonated series up to m = 20, but also claim to have detected a $[Mo_mO_{3m+2}]^{4-}$ series (m = 9-23), and the highly charged heptamolybdate $[Mo_7O_{24}]^{6-}$ in small amounts. The difference between the two experiments lies in the concentration of molybdenum (848 mM) and the very high capillary voltage of –3.5 kV compared to the –1.0 kV which were applied in our experiments. Deploying very high capillary voltages can lead to polymerisation during ionisation, which can explain the highly molecular species like $[Mo_{21}O_{71}]^{4-}$ that they found originating from a solution with pH 6.

For this variation series a sample with the maximum of different species was chosen: 35 mM molybdenum and pH 3. First, the capillary voltage was varied between -0.5 and -1.4 kV. An overview of all spectra recorded at different capillary voltages can be found in Figure 3.6. The spectra with a capillary voltage of -0.50, -0.65, and -0.80 kV are not shown, since there were no signals visible, only background noise, indicating that a capillary voltage below -0.95 kV does not lead to a stable ion spray, same applies for capillary voltages above -1.40 kV.

The m/z range from 50 to 250 is quite sensitive to background noise and stray signals, so it is of interest to eliminate these as much as possible. At capillary voltages of -0.95 and -1.00 kV, none of these signals are visible, so the optimum voltage lies in this range.

Furthermore it is of great interest to see how the presence of species changes with the parameter settings. For this, the relative concentration of all present species was plotted against the different values of a certain parameter. This can be found in Figure 3.5 top.

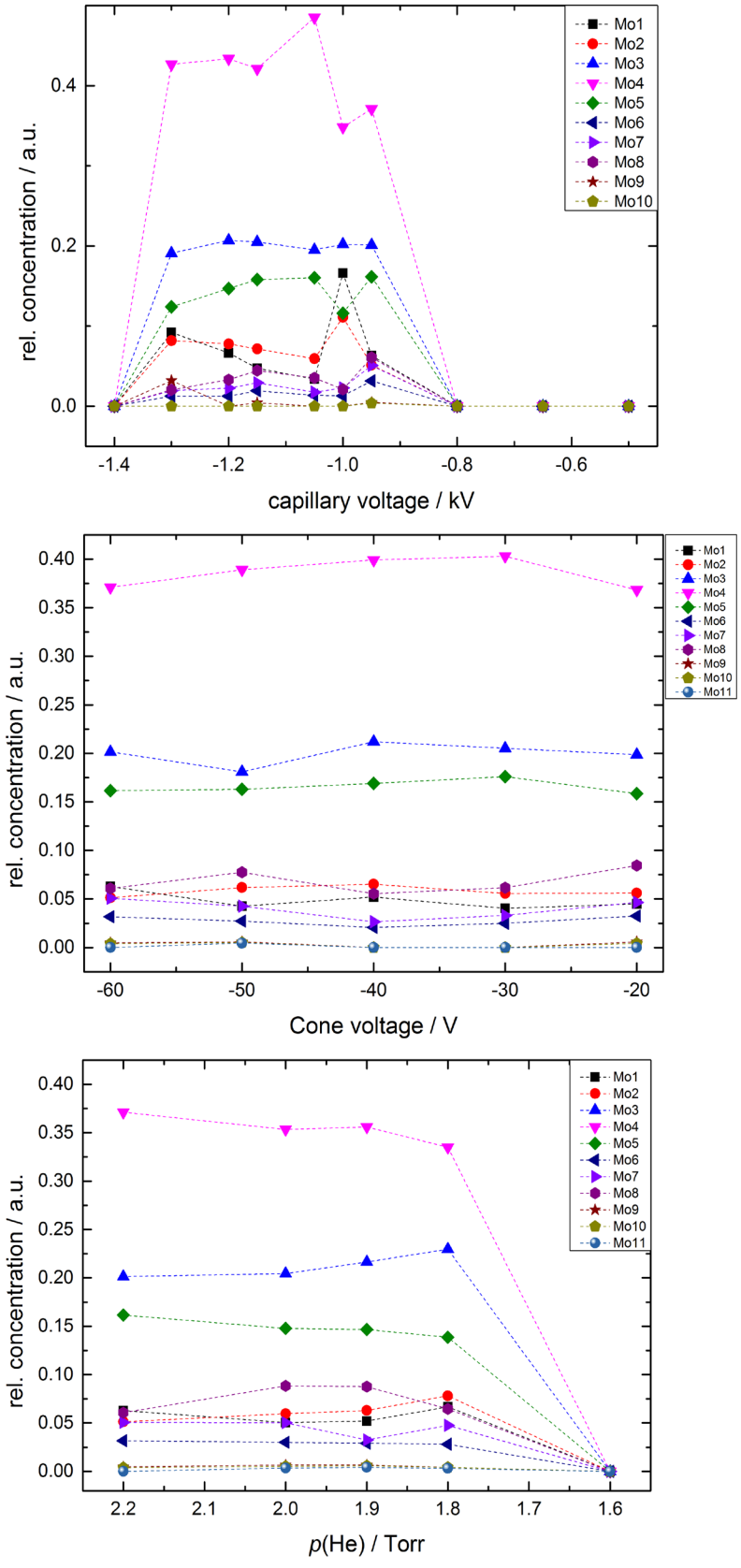

Figure 3.5: Distribution of molybdate species in 35 mM Mo aqueous solution with a pH of 3, depending on different mass spectrometric parameters: capillary voltage, cone voltage, and He pressure in the IMS cell (top to bottom).

There is a clear dependence on the capillary voltage in the chosen range, since there are only species present in the spectra at voltages from -0.95 -1.30 kV. Within this range, the relative concentration of tri-molybdates is constant, but the tetramolybdates experience a jump at -1.05 kV to higher concentrations, whereas at -1.00 kV the mono- and dimolybdates increase and the pentamolybdates decrease simultaneously.

Still, when it comes to bigger POMs, the lowest possible voltages are best to inhibit fragmentation, as was to be expected.

Varying the cone voltage, which is the voltage that is applied at the sampling cone, does not lead to any significant changes in the species concentration (Figure 3.5 middle) and can therefore be neglected in further discussions. The same can be said for the helium pressure in the ion mobility cell. At a pressure of 1.6 Torr, the signal breaks down and no species can be detected anymore. Any other higher pressure leads to a stable flow and not much difference in the relative

concentrations of the species. If one looks closely enough, it seems like species with three molybdenum atoms or less are favoured by lower pressures, whereas bigger molecules are more present at higher pressures.

To be sure, various voltage variations were carried out at a different, but fully comparable, spectrometer which came to the same conclusions as before regarding the speciation present.

After all, the distribution of species is not significantly affected by a wide range of parameter values.

Furthermore, there are different structural possibilities for any given formula. Walanda *et al.*[149] suggested that the $[Mo_mO_{3m+1}]^{2-}$ series consists of corner-linked tetrahedra, but there are also other possibilities, which yet have not be documented as isolated species in solids. An example is given in Fig. 3.10 with different structures of the $[Mo_4O_{13}]^{2-}$ anion. It is widely known that the speciation in solution is dependent on the molybdenum concentration and the pH value[150, 151]. The distribution diagrams mentioned in the introduction will now be compared with our measured MS data.

The mass spectrometric diagram based on the average cluster size of present species is shown in Fig. 3.6. At lower concentrations and higher pH values – i.e. all samples with $c_{Mo} \leq 0.7$ mM and pH ≥ 7 – monomeric $[MoO_4]^{2-}$ species are by far the most dominant, whereas at higher concentrations and lower pH values first tetramolybdate $[H_xMo_4O_{13}]^{x-2}$ (x = 0, 1) and smaller percentages of higher condensed species dominate and for samples with a concentration of 350 mM and pH values from 3 to 7 dimolybdates $[H_xMo_2O_7]^{x-2}$ (x = 0, 1) are the most abundant species and lower the value of the average cluster size. There are no data present for the samples with 350 mM molybdenum and a pH of 2, since after adding the acid almost immediately molybdic acid started forming as a white precipitate and therefore no reliable mass spectra could be obtained.

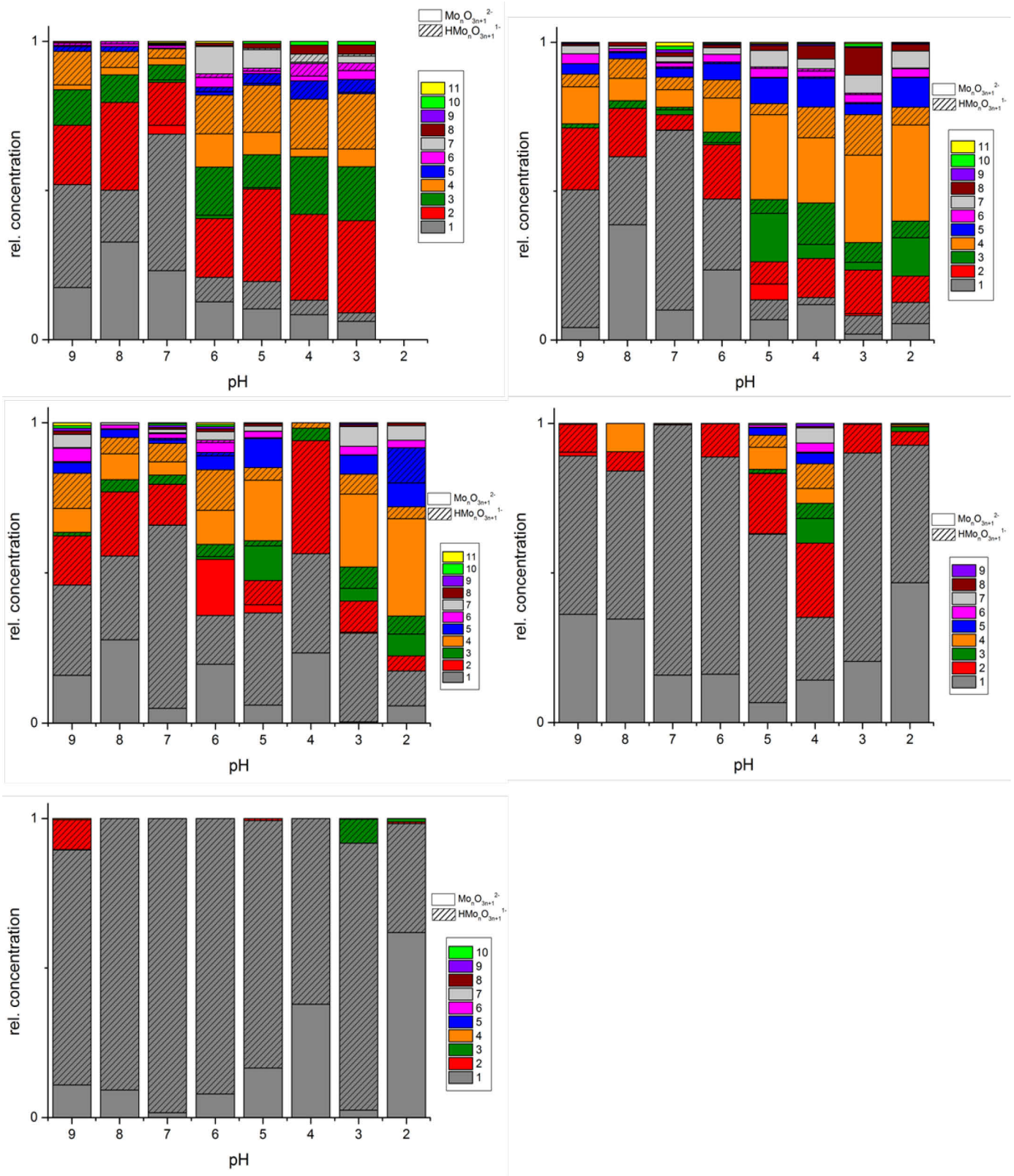

Fig. 3.6: Distribution of different molybdate species in the mass spectrometer based on the concentration and pH value in solution. 350 mM (top left), 35 mM (top right), 7 mM (middle left), 0.7 mM (middle right), 0.07 mM (bottom left).

For concentrations below 0.7 mM, the MS data agree with the predominance diagram by Baes and Meamer[91], additionally, the MS data show monomolybdate as dominant species for all concentrations in the pH range of 7-9 like in the literature diagram. But apart from this, discrepancies in dominance arise. Combining all three aforementioned predominance diagrams, a systematic difference between the data sets can be found: where in the MS data tetramolybdate is the most dominant species, heptamolybdate $[Mo_7O_{24}]^{6-}$ is claimed to be the dominant one by all three sources, and where dimolybdate is abundant in our measurements, octamolybdate $[Mo_8O_{26}]^{4-}$ is the dominant species. A peculiarity is, that no higher charged and condensed species like $[Mo_7O_{24}]^{6-}$ or $[Mo_8O_{26}]^{4-}$ are found in our studies. This agrees well with the findings of Fan et al., claiming that polyoxotungstates in higher charged stages are not stable anymore once they are freed of their surrounding solvent and hence fragment in mass spectrometric investigations[152]. It is probable that this is the reason why no molybdate species of that kind could be detected in the mass spectra, since even tungstates, which form stronger metal oxygen bonds[153], are not stabilised.

The aforementioned investigations have taken place with water as solvent and with only small counter cations like NH_4^+. Thus, the question arises if the probable fragmentation can be prevented by stabilising the condensed and highly charged polyoxomolybdates by addition of larger cations, e.g. tetrabutyl ammonium (short: TBA) $C_4H_{36}N^+$. These cations also demand a change of the solution medium to organic solvents, which might also influence the stability.

3.2.2 Detection of octahedral $[Mo_8O_{26}]^{4-}$ in the mass spectrometer

Tetrabutylammonium octamolybdate $(C_{16}H_{36}N)_4[Mo_8O_{26}]$ was synthesised in acetonitrile. The resulting colourless solid was analysed by X-ray diffraction and ICP-OES and XRF to gain insight over the purity of the sample. The respective diffractogram is shown in Fig. 3.7 and the results of the elemental analysis in Tab. 3.3.

Tab. 3.3: XRF (Mo) and ICP-OES (rest) data of synthesised $TBA_4[Mo_8O_{26}]$ sample.

	Mo	C	H	N
Calculated (m%)	35.60	35.70	6.74	2.60
Measured (m%)	34.61	37.76	6.97	2.60

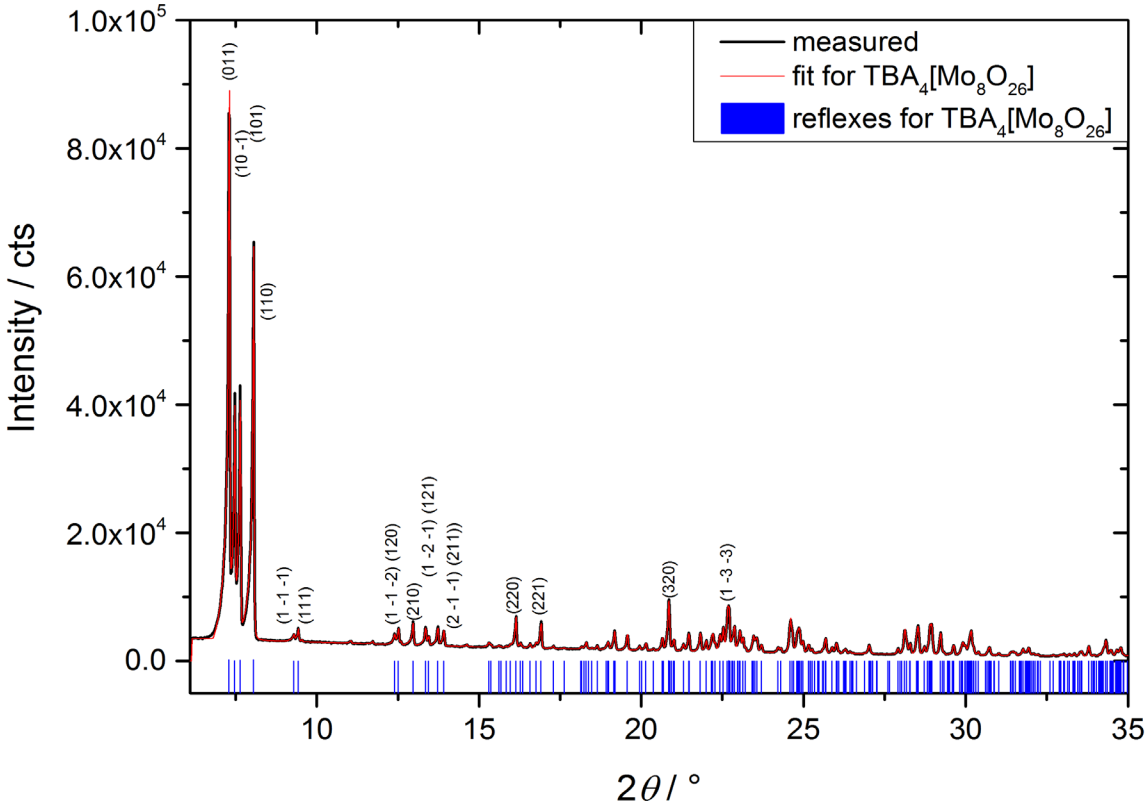

Fig. 3.7: X-ray diffractogram of synthesised $TBA_4[Mo_8O_{26}]$.

All atomic weight percentages of the elements agree quite well with the calculated values, only carbon is about 2 % higher than the calculated percentage. This might be due to small amounts of residual free ligands or of the solvent. Still, the diffractogram in Fig. 3.7 shows phase-pure $TBA_4[Mo_8O_{26}]$.

The respective mass spectrum of the sample can be found in Figure 3.8. Clearly, there are more signals visible than there are expected. Only one octamolybdate species can be found in the mass spectrum: $TBA_3[Mo_8O_{26}]^-$ (m/z 1912). These are the only species of this condensed molybdate that can be found, neither $TBA_2[Mo_8O_{26}]^{2-}$, $TBA[Mo_8O_{26}]^{3-}$ nor $[Mo_8O_{26}]^{4-}$ are visible in the mass spectrum. Instead, a lot of other molybdate species from the $[HMo_mO_{3m+1}]^-$ and $[Mo_mO_{3m+1}]^{2-}$ series are present, namely monomolybdates $[MoO_3]^-$ (m/z 145) and $[HMoO_4]^-$ (m/z 162), dimolybdate $[HMo_2O_7]^-$ (m/z 304), trimolybdates $[Mo_3O_{10}]^{2-}$ (m/z 223) and $[HMo_3O_{10}]^-$ (m/z 448), tetramolybdates $[Mo_4O_{13}]^{2-}$ (m/z 296) and $[HMo_4O_{13}]^-$ (m/z 592), pentamolybdate $[Mo_5O_{16}]^{2-}$ (m/z 367), hexamolybdate $[Mo_6O_{19}]^{2-}$ (m/z 440), octamolybdate $[Mo_8O_{25}]^{2-}$ (m/z 583), and nonamolybdate $[Mo_9O_{28}]^{2-}$ (m/z 656).

The most dominant species are $[Mo_3O_{10}]^{2-}$, $[Mo_4O_{13}]2-$ and $[Mo_5O_{16}]^{2-}$.

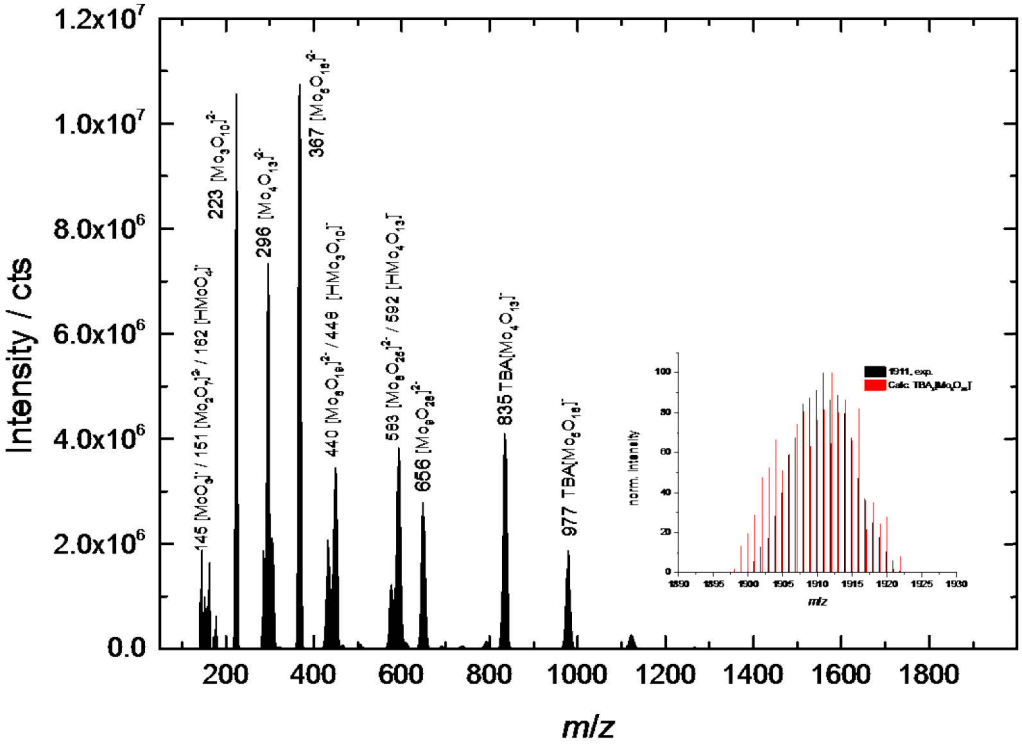

Figure 3.8: Mass spectrum of $TBA_4[Mo_8O_{26}]$ in pure acetonitrile with a molybdenum concentration of 35 mM.

It is very important to note that the signal at roughly m/z 835 can correspond to both $TBA_2[Mo_8O_{26}]^{2-}$ and $TBA[Mo_4O_{13}]^-$. Taking a look at the isotopic pattern, it is clear that in this case the tetramolybdate species is present. This suggests that octamolybdate $[Mo_8O_{26}]^{4-}$ is only stable with big counter cations

surrounding it. Taking only one ligand away can already lead to fragmentation. Another TBA species present is pentamolybdate $TBA[Mo_5O_{16}]^-$ at m/z 977.

Tetrabutylammonium octamolybdate is not soluble in pure water. Instead a serial dilution was made and analysed by MS. All final solutions had a molybdenum concentration of 35 mM, exactly like the solution with pure MeCN. The result in species distribution depending on the water content in the solution is shown in Figure 3.9. From 50 % MeCN on or lower, a white solid started to precipitate immediately after mixing the MeCN solution with water. Therefore these samples were not analysed any further.

$TBA_3[Mo_8O_{26}]^-$ remains at a very low concentration throughout the serial dilution, but it drops continually with decreased acetonitrile percentage. This is the first and most important indication, that this species is not stable in aqueous solutions. Raising the water percentage results additionally in a strong increase of small molecules, i.e. with one or two molybdenum atoms, whereas the molecules with five or more molybdenum atoms decline or stagnate at a very low concentration level. Especially tetramolybdate seems to be particularly stable in the MS.

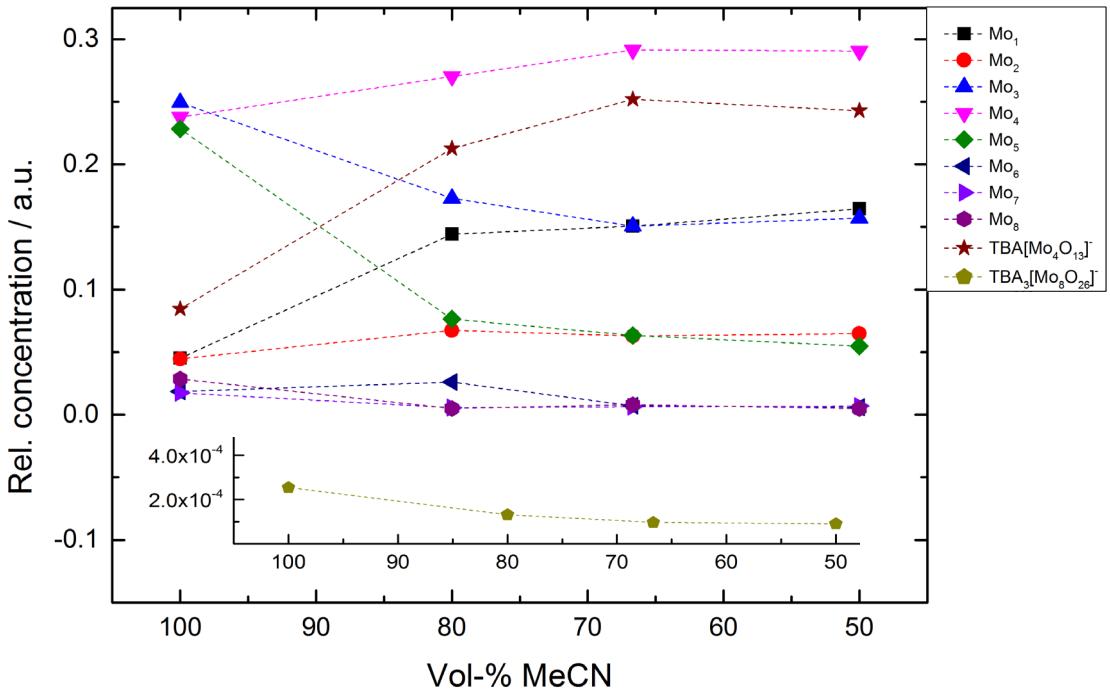

Figure 3.9: Speciation distribution depending on the acetonitrile content of the solution medium.

3.2.3 Ion mobility mass spectrometry and collision cross sections

To get an idea which structure might be present in the mass spectrometer, collision cross sections (CCS) were measured by varying the IMS bias voltage in steps of 10 from 20 to 90 V and determining the drift time of the $[Mo_4O_{13}]^{2-}$ species at a m/z ratio of 296. Plotting the drift time t_D against the inverse voltage $1/V$ leads to the mobility K according to Eq. (1):

$$t_D = \frac{L^2}{K} \cdot \frac{1}{V} + t_0 \qquad (1)$$

L - drift length, 0.1 m

t_0 - time offset

This mobility K is connected to the CCS Ω via the Mason-Schamp equation (2).

$$\Omega = \frac{3 \cdot q}{16 \cdot N} \cdot \sqrt{\frac{2 \cdot \pi}{\mu \cdot k_B \cdot T}} \cdot \frac{P_0 \cdot T}{P \cdot T_0} \cdot \frac{1}{K} \qquad (2)$$

q - charge $z \cdot e^-$

N – drift-gas numer density, 4

μ – reduced mass (ion + drift-gas molecule)

k_B – Boltzmann constant

T – drift gas temperature, 300 K

P – drift gas pressure, 1.8 Torr

The measured CCS has to be compared with a calculated value to either reject or approve a structure. As a calculation approach Projection Approximation (PA) was used, which virtually turns the molecule in different directions and calculates the two-dimensional area. The measured CCS should not differ from these values by more than 10 %. Results

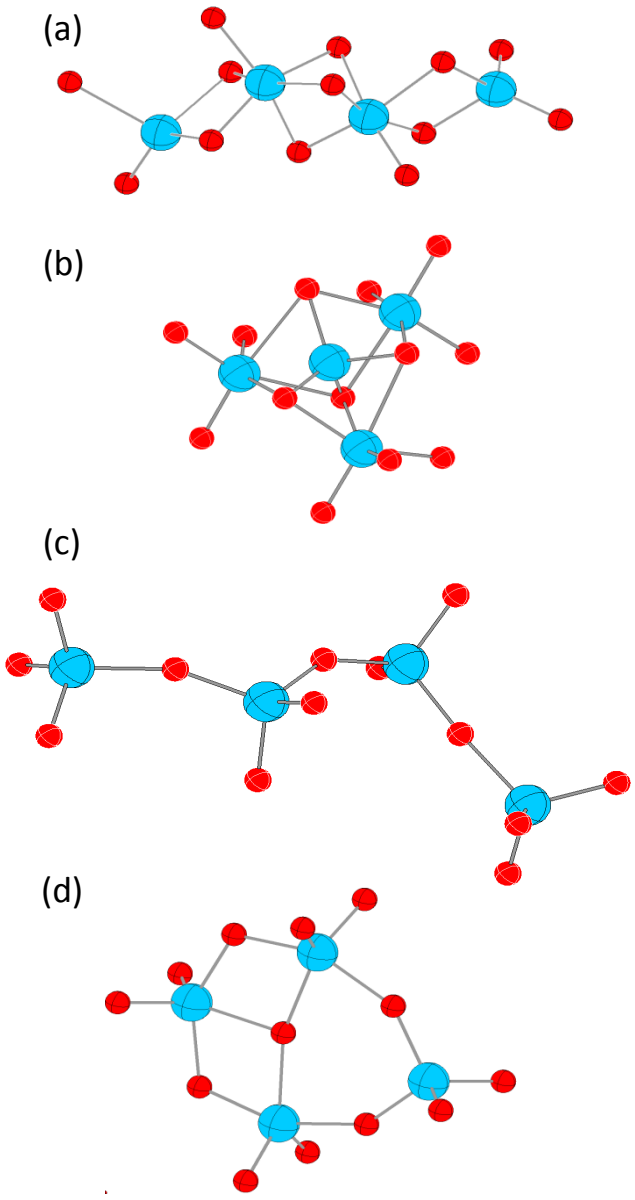

Fig. 3.10: Possible structures for a molybdate anion with the sum formula $[Mo_4O_{13}]^{2-}$ (Mo: blue, O: red): (a) two face-linked octahedra with two edge-sharing tetrahedra on each one; (b) three edge-linked octahedra with a central molybdenum in between; (c) chain of corner-linked tetrahedra, see Walanda et al.[32], (d) ring of three edge-sharing trigonal bipyramids and one corner-sharing tetrahedron.

for the tetramolybdate molecule are found in Tab. 3.4.

Based on the shown results, the structures of Fig. 3.10 (a) or (d) are most likely to be present in the mass spectrometer.

Tab. 3.4: Measured and calculated CCS of tetramolybdate $[Mo_4O_{13}]^{2-}$

Structure	Measured CCS	Calc. CCS (PA)
$[Mo_4O_{13}]^{2-}$	94 Å²	
Fig. 2 (a)		95 Å²
Fig. 2 (b)		82 Å²
Fig. 2 (c)		113 Å²
Fig. 2 (d)		93 Å²

To obtain a complete picture of the species present in the gas-phase, collision cross sections of all molecules of the $[Mo_mO_{3m+1}]^{2-}$ series up to m = 8 (excluding m = 2, due to lack of intensity) were measured. The graphic depiction of the results can be found in Fig. 3.11 as function of present molybdenum atoms. Following Walanda et al.'s predictions[149], the aforementioned molybdate series should consist of linear species, which in response would lead to a linear trend in collision cross sections. However, it is clearly visible that there are three distinctive structural domains, as the CCS for one between $[Mo_3O_{10}]^{2-}$ and $[Mo_4O_{13}]^{2-}$ reduces from 93 to 92 Å², and for two between $[Mo_5O_{16}]^{2-}$ and $[Mo_6O_{19}]^{2-}$ reduces from 112 to 102 Å².

Using density functional theory (DFT) calculations, model structures were constructed with different dimensionalities corresponding to the different domains. For $[HMoO_4]^-$ the lowest energy is found by a simple tetrahedral structure with one of the Mo surrounding oxygens being protonated. The respective CCS amounts to 46.5 Å² and therefore fits very well with the experimental value of 45 Å². The theoretical minimum of $[Mo_2O_7]^{2-}$ belongs to a structure with two edge-sharing tetrahedra and fits with a theoretical CCS of 70 Å² perfectly with the interpolation between mono- and trimolybdate. For trimolybdate $[Mo_3O_{10}]^{2-}$ the linear structure with three edge-sharing tetrahedra turned out to be more stable than a ring shape, and its calculated CCS of 92 Å² fits with the experimental value, while the CCS of the ring structure (75 Å²) is too low.

Linear and ring structures have been used as a base for the calculations of tetra- and pentamolybdate as well. The most stable tetramolybdate consists of a Mo_4O_{12} ring with one oxygen atom in the middle of the ring binding to three of the four molybdenum atoms. The corresponding CCS has the value of 91 Å² and is with that more fitting than the linear counterpart with 113 Å². Pentamolybdate $[Mo_5O_{16}]^{2-}$ displays the same tendency to ring-like structures, offering two different structural conformers: analogue to tetramolybdate at Mo_5O_{15} ring with one oxygen atom in the middle (CCS 110 Å²), or the already described $[Mo_4O_{13}]^{2-}$ ring structure with an additional MoO_3 moiety attached to one of the outer oxygens (CCS 113 Å²). Both of these structures are reasonable regarding the experimental CCS of 112 Å², and are almost equally energetically favoured.

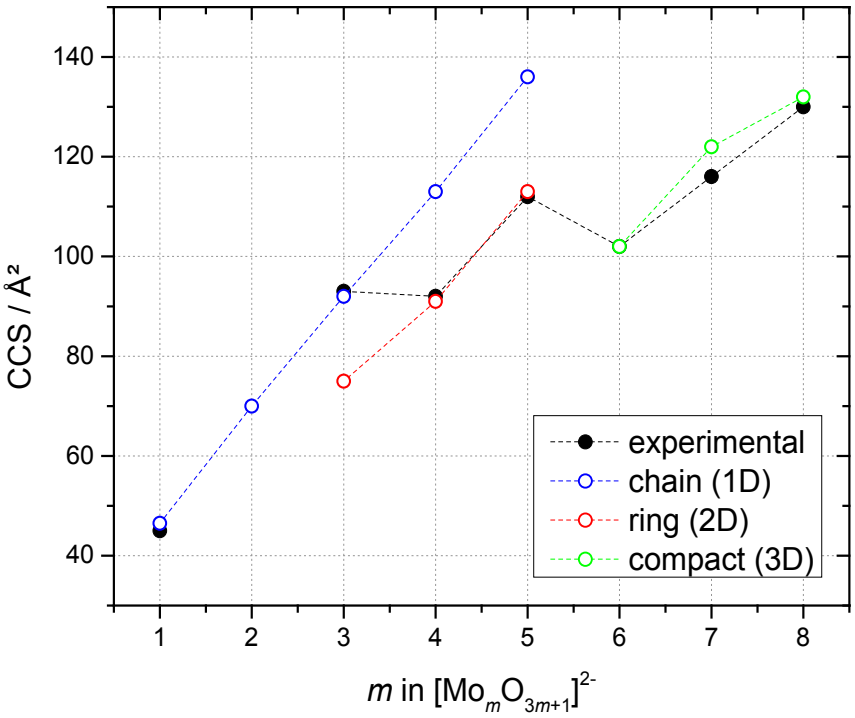

Figure 3.11: Recorded CCS values (black) as function of the number of molybdenum atoms in the cluster m, calculated CCS for different structural types in colour.

A drastic change occurs in the CCS of the next molybdate, $[Mo_6O_{19}]^{2-}$. Polyoxometalates with this sum formula are known as the Lindqvist anions with highly symmetric structure[100]. DFT calculations support this structure as the one with lowest energy and the calculated CCS of 102 Å² is a perfect fit with the experimental result. The linear increase of the collision cross sections for m = 6-8 suggests that hepta- and octamolybdate as well retain the symmetric Lindqvist core. Adding a MoO_3 moiety to a terminal oxygen atom leads to a predicted CCS of 122 Å² and is only slightly more stable than the version with the addition to a bridging oxygen (114 Å²). The most stable structure of octamolybdate $[Mo_8O_{25}]^{2-}$ differs from the preceding heptamolybdate only by having another MoO_3 moiety added to the already existing one, leading to a Mo_2O_6 group. This time however, the additional group is connected to a bridging oxygen, as calculations showed. Still, the calculated CCS of 132 Å² fits well with the experimental one (130 Å²).

This is combination of ion mobility mass spectrometry and DFT calculations proves the structural diversity of molybdates in the gas-phase.

To validate these structural changes further, infrared multiple photon dissociation (IRMPD) spectroscopy in combination with density functional theory (DFT) calculations was applied.

3.2.4 Infrared multiple photon dissociation (IRMPD) spectroscopy

For IRMPD spectroscopy, ions were selected and separated based on their CCS/z and m/z ratios and then irradiated by infrared photons originating from the Fritz Haber Institute free electron laser (FHI FEL) [154]. Due to the radiation, the ions can fragment, which is then measured by time-of-flight (TOF) mass spectrometry. This fragmentation yield is then plotted against the IR wavelength to obtain the IRMPD spectrum.

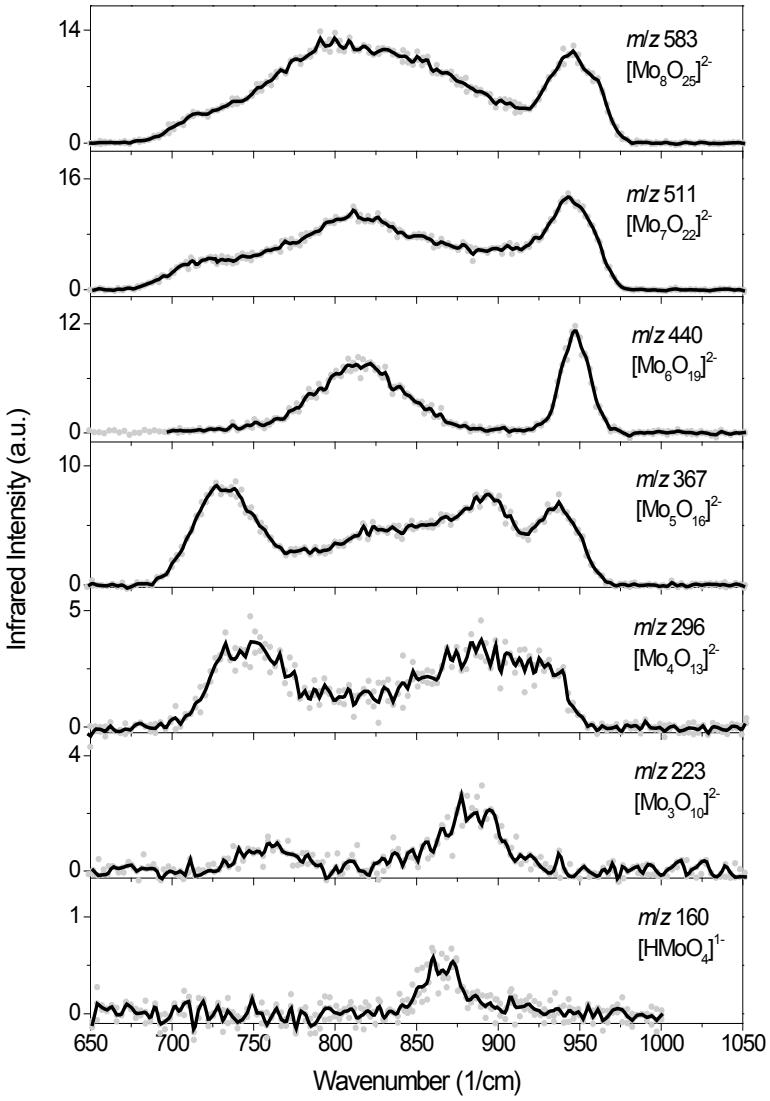

Figure 3.12: Recorded IRMPD spectra for different molybdate ions.

The IRMPD spectra of $[HMoO_4]^-$ and the $[Mo_mO_{3m+1}]^{2-}$ molybdates with m = 3-8 are shown in Fig. 3.12. Mono- and trimolybdate spectra show a broad band between 850 and 900 cm^{-1} which corresponds to the Mo=O stretching vibration. This band then broadens further for $[Mo_4O_{13}]^{2-}$ and splits in the spectrum of $[Mo_5O_{16}]^{2-}$. Furthermore, the spectra of tetra- and pentamolybdate possess another band between 730 and 750 cm^{-1} with significant intensity. The spectra of the higher molecular molybdates look completely different, however. A narrow band at around 950 cm^{-1} appears, which is accompanied by a continuously broadening band with its maximum around 800 cm^{-1}. These three different types of IRMPD spectra agree with the observation of structural three domains in the CCS (Fig. 3.11).

IR spectra calculations of the previously assigned molybdate structures were performed to validate the results. Fig. 3.13 shows the experimental spectra (red line) and the harmonic (light grey) and anharmonic (dark grey) vibrational spectra of the calculated structures left to the graphs. The calculated

spectra for $[HMoO_4]^-$ show only one signal belonging to the stretching vibration of Mo=O and with that agree well with the experimental data. Calculations for $[Mo_3O_{10}]^{2-}$ make it possible to assign the less intense band at 760 cm^{-1} to asymmetric stretching vibrations of Mo-O-Mo, which are predicted for 790 cm^{-1} in the harmonic vibrational calculations. The broad band between 850 and 900 cm^{-1} belongs again to the stretching vibration of Mo=O. This structure made up of corner-linked tetrahedra has not been found in solution or solid state so far. While $[Mo_3O_{10}]^{2-}$ can be precipitated from an aqueous solution with K^+ or Rb^+, the resulting polymeric trimolybdate chain consists of edge-sharing octa- and tetrahedra. Hence, desolvation without any counter ion might result in this linear chain.

Calculations based on the ring structure of $[Mo_4O_{13}]^{2-}$ assign the band at 750 cm^{-1} to asymmetric stretching vibrations of Mo-O-Mo within the ring structure, while the broad band between 850 and 950 cm^{-1} originates from Mo=O stretching outside of the ring. Additionally, the improved agreement between the anharmonic vibrational calculation and the experimental data suggests the dynamic nature of the single oxygen atom inside the ring, meaning it can change its position to bond to three different molybdenum atoms at a time within picoseconds. Same as with trimolybdate, this structure might be a product to the unique conditions of desolvation and non-existence of counter ions, as it is not known in solution and does not exist in solid state. If $[Mo_4O_{13}]^{2-}$ is part of a solid, its structure is composed of edge-sharing octahedral chains. Furthermore, inorganic tetramolybdate containing solids have only been obtained via solid state synthesis for the time being[155, 156].

While the experimental spectrum for $[Mo_5O_{16}]^{2-}$ looks similar to the one for tetramolybdate, it features more distinct IR bands. As with the other spectra before, the bands at 730 cm^{-1} can be assigned to the asymmetric Mo-O-Mo stretching vibration. Based on the possible ring structure of the molecule, the band at 890 cm^{-1} can be attributed to the Mo=O stretching vibrations of the MoO_3 moiety attached to the outside of the ring, and the band at 937 cm^{-1} to the Mo=O stretching vibration within the ring. Calculation of the Lindqvist-anion as structure for $[Mo_6O_{19}]^{2-}$ leads to a perfect fit regarding the band at 947 cm^{-1}, which belongs to the Mo=O stretching vibrations. This anion is known to be present only in non-aqueous environment, but can be precipitated from acidic aqueous solution as a TBA-salt, or synthesised directly in dimethylformamide[100]. In this case, the term “non-aqueous” not only includes organic solvents but also gas-phase environment without additional stabilisation.

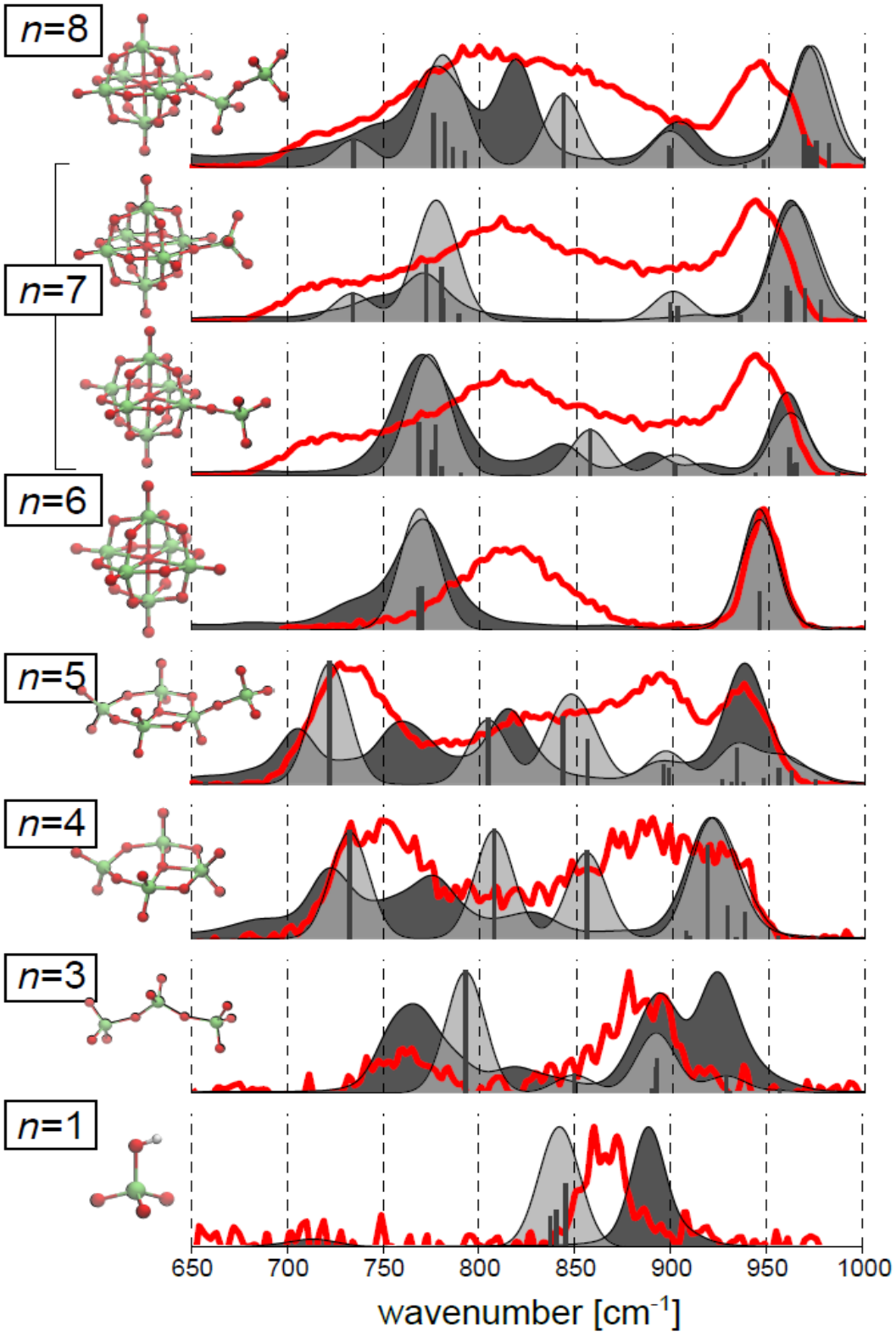

Figure 3.13: Experimental IRMPD (red) and unscaled calculated IR spectra of the investigated deprotonated molybdate species. Black sticks and light grey broadenings belong to the harmonic vibration calculations; the anharmonic calculations are shown in dark grey.

The second signal of the calculation is shifted by 50 cm^{-1} compared to the experimental data of 815 cm^{-1}, but still can be assigned to the Mo-O-Mo asymmetric stretching vibrations of the highly symmetric Lindqvist structure. In Fig. 3.13 two possible structures for heptamolybdate $[Mo_7O_{22}]^{2-}$ are displayed, with the additional MoO_3 moiety connected for one to a bridging and for another to a terminal oxygen atom. While the harmonic spectra of both structures show different additional bands, it is only the superstition of both spectra that fits with the experimental data. Taking the theoretical CCS of both structures into consideration as well, leads to the conclusion that the two structures may convert between each other in a short time scale. Lastly, the calculated IR spectra of $[Mo_8O_{25}]^{2-}$ confirm the structure suggested by CCS calculations, too.

The IRMPD spectra for protonated molybdate species with n = 2 – 7 have been recorded and fitted with DFT calculations as well. The results are shown in Fig. 3.14. The experimental spectra (Fig. 3.14, red) show the dimolybdate to possess only one band at around 890 cm^{-1}, whereas all molecules with three or more molybdenum atoms show two signals. The sharper signal around 950 cm^{-1} for the Mo=O vibration shifts continuously to higher wavenumbers with increasing *n*. The band attributed to Mo-O vibrations shifts from 850 cm^{-1} for trimolybdate to 825 cm^{-1} for heptamolybdate and becomes slightly sharper in the process.

The structures calculated for these spectra are depicted on the right side in Fig. 3.14. Two structures are possible candidates for the structure of $[HMo_2O_7]^-$: Edge-sharing or corner-sharing tetrahedra. While the calculated spectra of the edge-sharing version fits the experimental spectra better, the structure is less stable by 7 kcal compared to the corner-sharing structure. The deprotonated dimolybdate was calculated to be consistent of corner-sharing tetrahedra, hence it is more probable that this structural aspect remains the same for the protonated species, especially since the edge-sharing structure is less stable.

While trimolybdate is a chain of tetrahedra in its deprotonated form, protonation leads to rearrangement into a ring structure, same as tetramolybdate possesses in its deprotonated as well as in its protonated form. The structure of pentamolybdate also undergoes a structural transformation from deprotonated to protonated state. The 2D ring structure without an additional hydrogen turns into a 3D condensed shape based on octahedra. In the case of hexa- and heptamolybdate, protonation does not change the structure

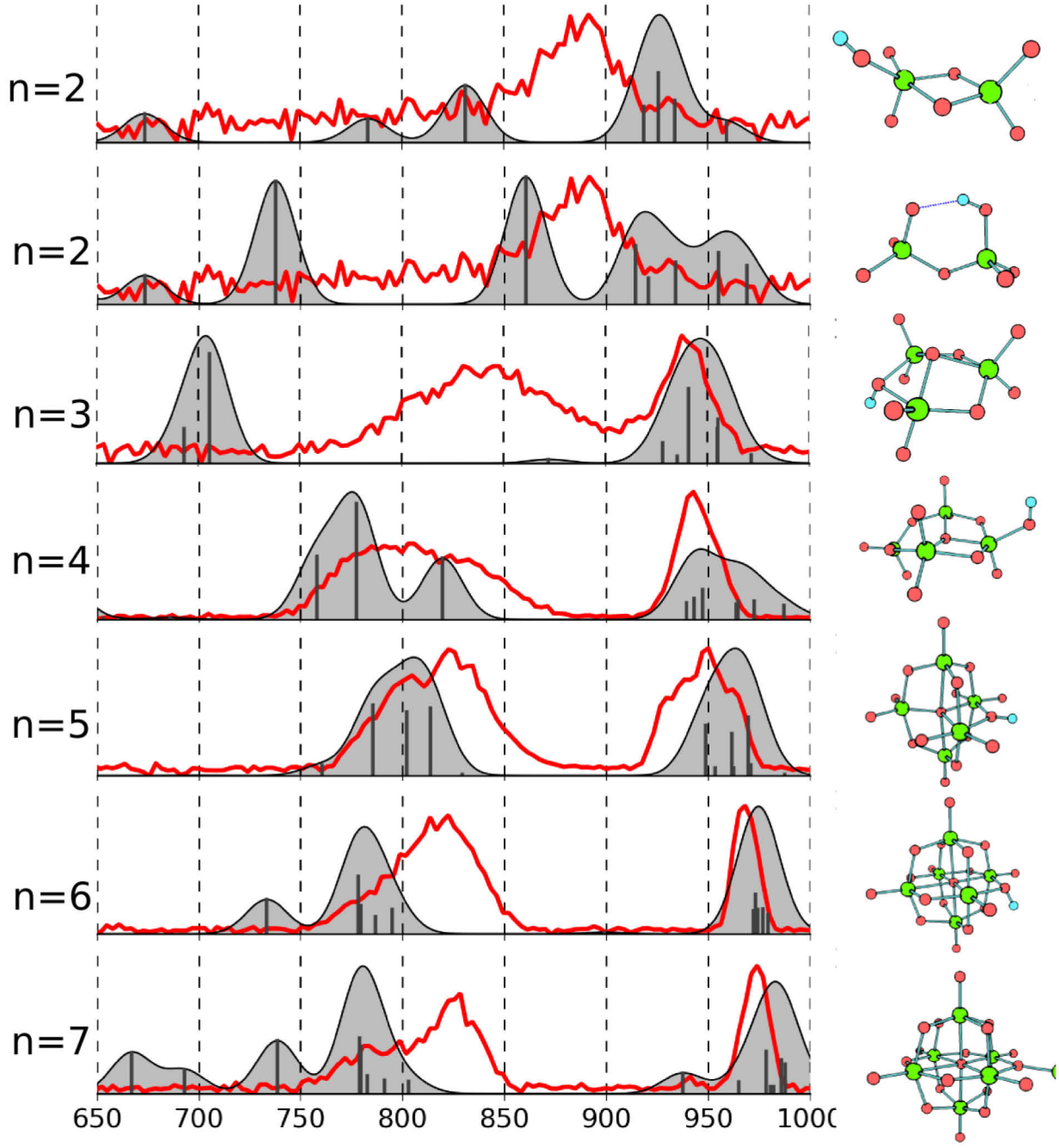

Figure 3.14: Experimental IRMPD (red) and unscaled calculated IR spectra of the investigated protonated molybdate species. Black sticks and light grey broadenings belong to the harmonic vibration calculations.

.

3.3 Raman calculation of gas-phase molybdates

The discrepancy between the species assigned to the Raman spectra and the species detected in the gas-phase leads to the question, if the species have been assigned correctly in the past, or whether a fragmentation takes place during the transfer into the gas-phase. To solve this, gas-phase Raman spectra of $[Mo_7O_{24}]^{6-}$ and the octamolybdates $[Mo_8O_{26}]^{4-}$ have been simulated. The stable structures and their corresponding uncorrected spectra can be found in Fig. 3.15 and 3.16, respectively.

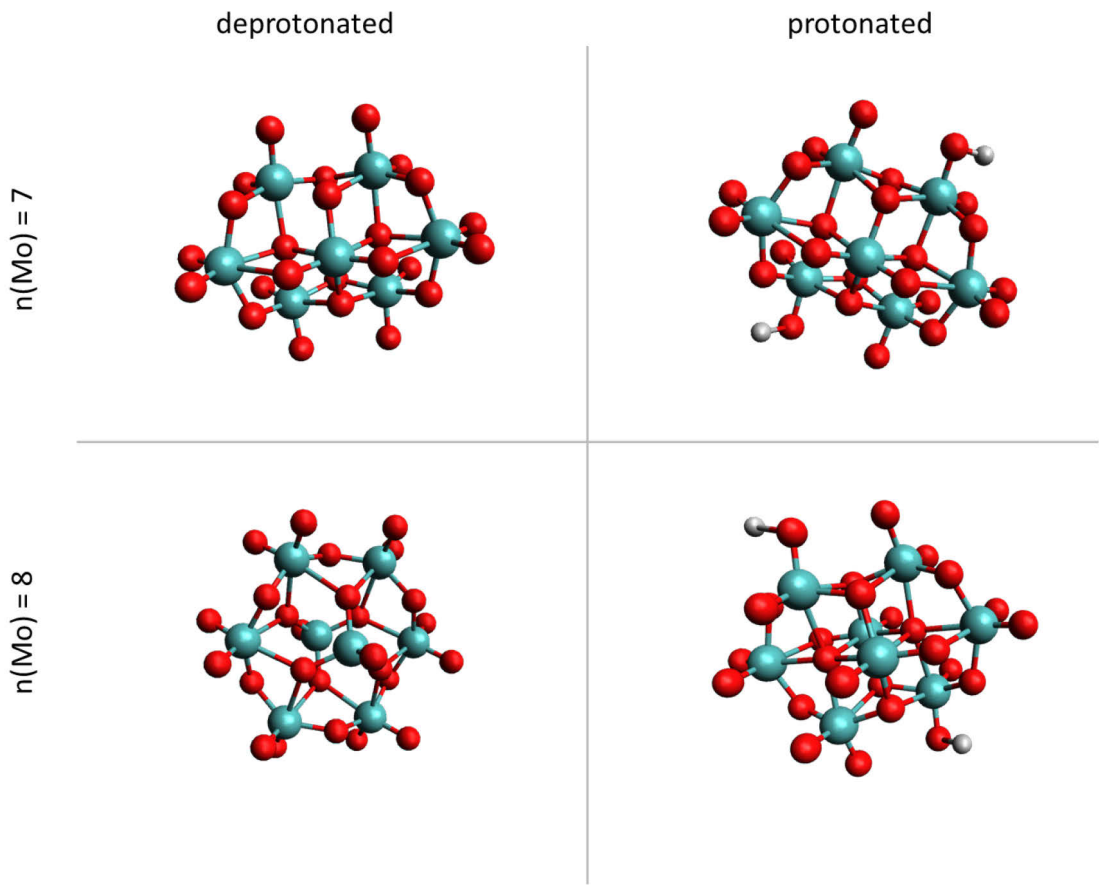

Fig. 3.15: Structures of condensed molybdate species known to literature, structures on the right were protonated to achieve stability during calculation of the Raman spectra.

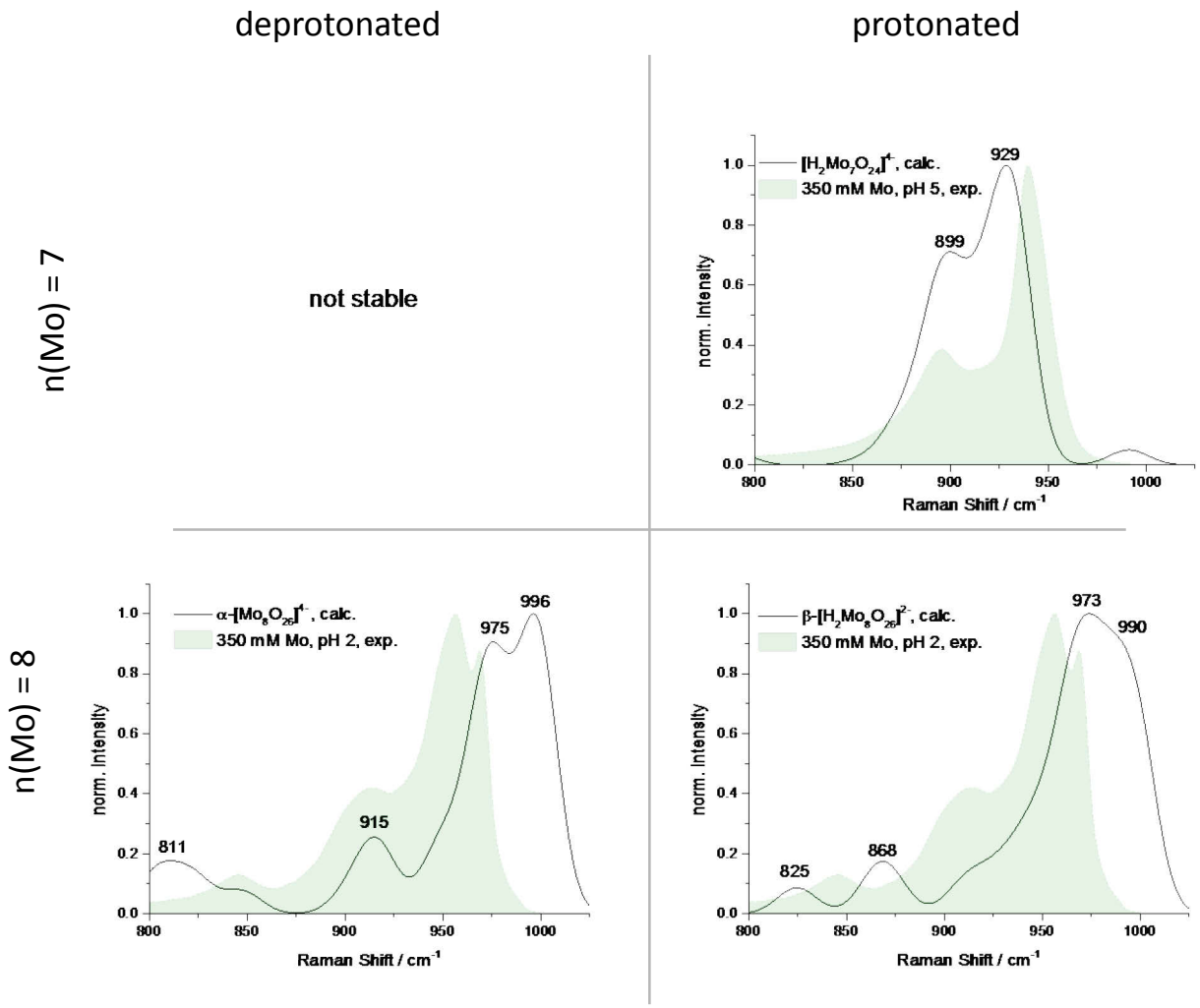

Fig. 3.17: Calculated Raman spectra for hepta- and octamolybdate species claimed to be present in aqueous molybdate solutions of higher concentrations and acidic pH values.

As it turned out, heptamolybdate and β-octamolybdate were only stable during calculation when at least two protons were added. This is not the case for α-octamolybdate, which keeps its structure in deprotonated state. For the derivation of the Raman spectrum, we tested multiple protonation sites and selected the lowest-energy structure. The spectrum of the doubly protonated heptamolybdate possesses signals at 899 and 928 cm^{-1}, belonging to stretching of the Mo-O bonds and asymmetric stretching of Mo=O bonds, respectively. This calculation fits the experimental data (350 mM Mo, pH 5, shown in Fig. 3.16) very well.

For octamolybdate $[Mo_8O_{26}]^{4-}$, two structures are claimed to be present simultaneously in aqueous solutions at low pH values and high molybdenum concentrations: the α- (HY 2039) and β-form (ICSD No. 35112). As with heptamolybdate $[Mo_7O_{24}]^{6-}$, β-octamolybdate remains stable only after adding two

protons that partially neutralize negative charge. Again, we tested multiple protonation sites and selected lowest-energy structure for the analysis. The calculated spectrum of α-octamolybdate shows signals at 811, 915, 975 and 996 cm^{-1}, which correspond to Mo-O stretching frequencies of the bridging oxygen atoms and to asymmetric and symmetric Mo-O stretching frequencies of the terminal oxygen atoms, respectively. As with heptamolybdate $[Mo_7O_{24}]^{6-}$, it turned out that β-octamolybdate is only stable during calculation if at least two protons are added to the structure. Said spectrum presents signals at 825, 868, 973 and 990 cm^{-1} (Fig. 3.12 bottom). These belong to vibrations of the bridging oxygen atoms, asymmetric and symmetric stretching vibrations of the terminal Mo-O bonds, respectively. Both calculated octamolybdate spectra agree well enough with the experimental data (350 mM Mo, pH 3), but taking into account the intensities of the signals, the calculation of β-$[H_2Mo_8O_{26}]^{4-}$ alone can represent the experimental data. Together with the postulation that α-octamolybdate should not be present in aqueous solution, this leads to the possibility that after all there is only β-octamolybdate present in aq. solution and both the signals at 956 and 969 cm^{-1} can be attributed to this species.

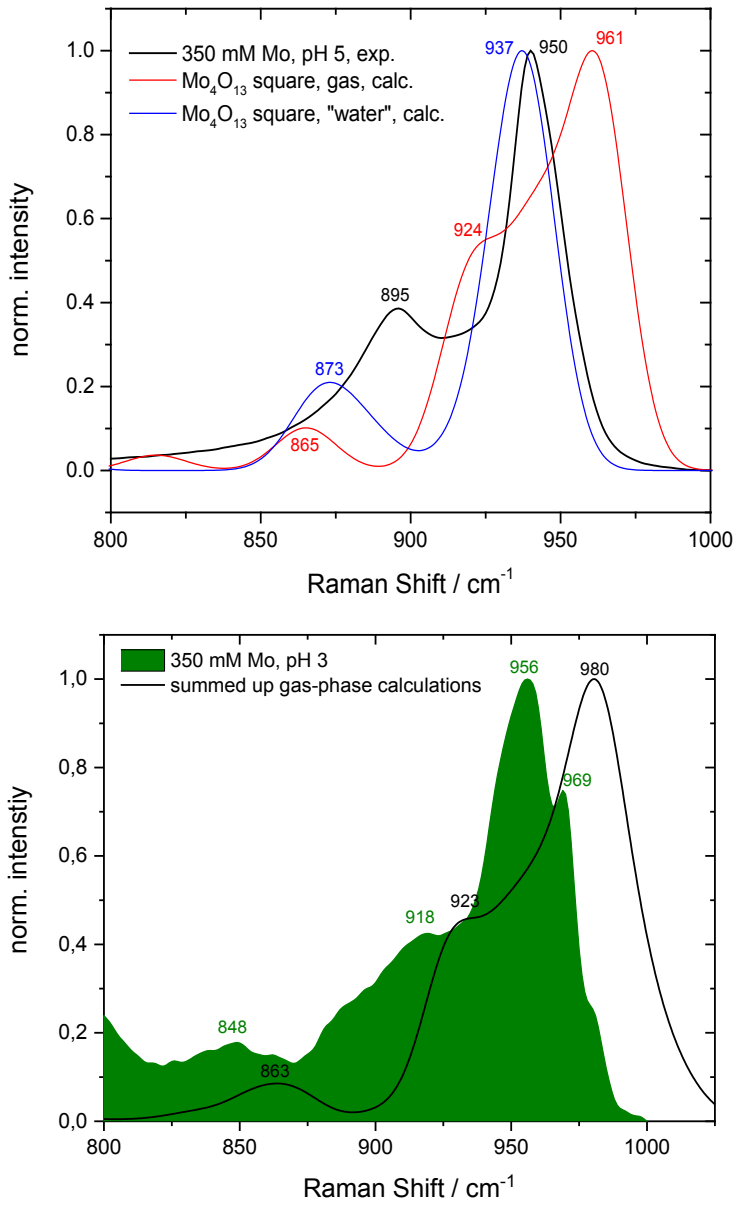

Fig. 3.18: Measured Raman spectrum of an aqueous molybdate solution at pH 3 and calculated Raman spectra of different tetramolybdate structures (top); measured Raman spectrum and the weighted summed up calculated spectra of all molybdate species present in the corresponding mass spectrometric measurement (bottom).

To double-check our assumption that only the literature-known molybdate structures are present in solution, we

compared the experimental spectrum of the 350 mM pH 5 solution with calculated spectra of the linear and square $[Mo_4O_{13}]^{2-}$ structures (Fig. 3.17), which is one of the major species in the corresponding mass spectrum. From the figure it can be seen that the gas-phase spectrum of the square structure (Fig. 3.10d) fits well with the experimental spectrum. However, there is still a high percentage of other molybdate species present in the mass spectrum of the measured solution, hence their respective Raman spectra should also be taken into account. These deprotonated and protonated species and their respective spectra in the gas-phase are shown in Tab. 3.5.

Tab. 3.5: Calculated Raman spectra of $[Mo_nO_{3n+1}]^{2-}$ molybdates in the gas-phase.

	Deprotonated	Protonated
Mo_8	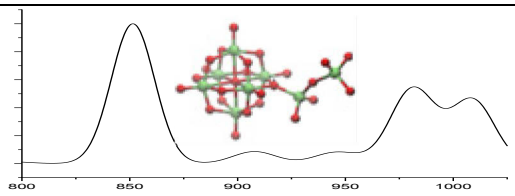	
Mo_7	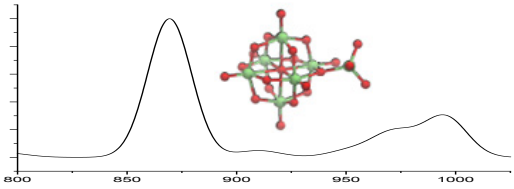	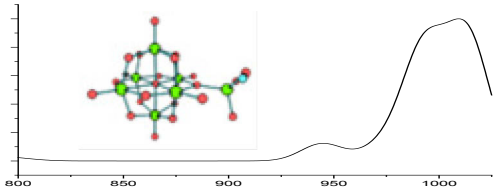
Mo_6	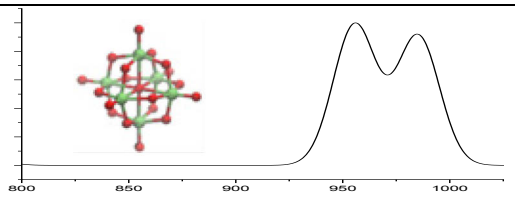	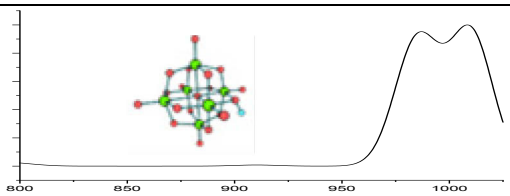
Mo_5	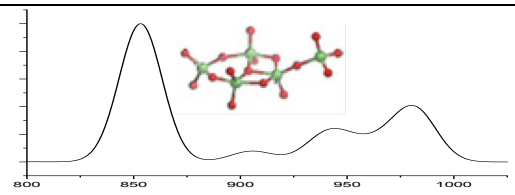	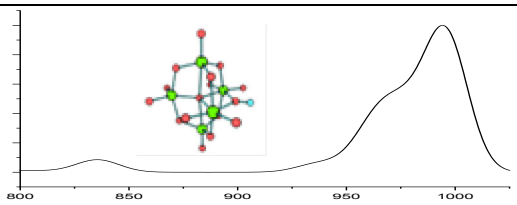
Mo_4	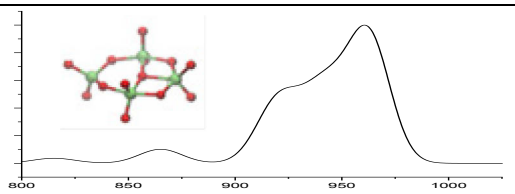	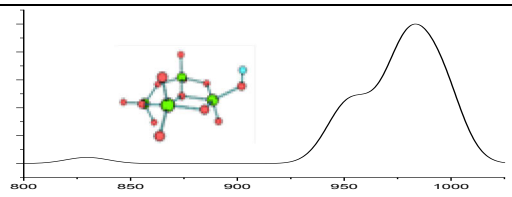
Mo_3	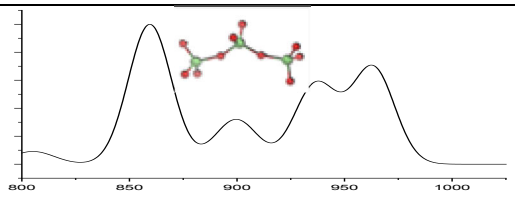	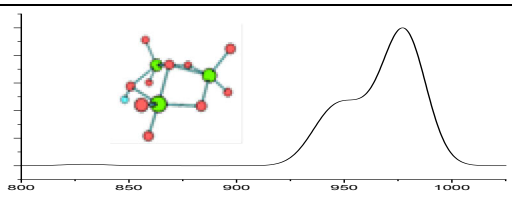
Mo_2	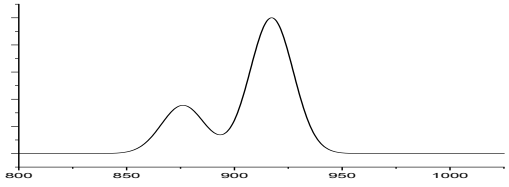	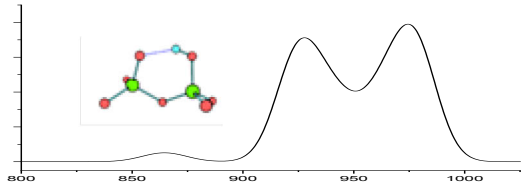
Mo_1		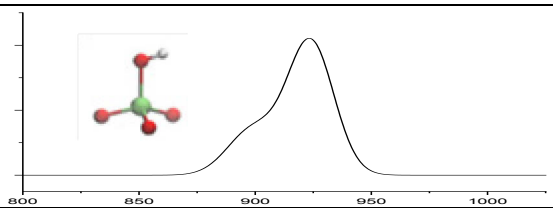

A cumulation of the Raman spectra of the in the mass spectra detected species can be found in Fig. 3.17 bottom. Here the calculated Raman spectra of molybdate species from n = 1-8 - as found in the mass spectrum - are weighted by their relative abundance and then summed up. While the wave numbers of the signals are off by up to 25 cm^{-1}, the general shape of the signals matches the experimental spectrum quite well. Hence, it cannot be clearly determined, whether the gaseous molybdate species are already present in aqueous solution or not.

3.4 Fragmentation processes in the mass spectrometer

Comparing different methods of analysing molybdate molecules in aqueous solution and in the gas-phase shows the possibility of either more structural diversity in the solution than can be described by common spectroscopic methods or the possibility of fragmentation of larger molecules during the ionisation process in the mass spectrometer. With regard to organic molecules, it has been discussed how different solvents influence the speciation in the mass spectrometer while leading to the same structural species in solution[157-159] and hence whether the solution phase is actually transferred to the gas-phase[160, 161]. Studies of Fan et al. claimed fragmentation for polyoxotungstate species to be possible[152], making room for assumptions about analogous behaviour of polyoxomolybdates or inorganic species in general.

Based on the abundance of the single species in the spectrometer, we now postulate possible fragmentation pathways of the highly condensed and charged molybdate species of $[H_2Mo_7O_{24}]^{4-}$, α-$[Mo_8O_{26}]^{4-}$, and β-$[H_2Mo_8O_{26}]^{2-}$. These are just the minimum number of added protons for the species to be stable in aqueous solution according to our calculations. Therefore a higher protonation of each species before entering the spectrometer is possible and for the highly charged heptamolybdate very likely.

At a pH value of 3, α- and β-octamolybdate are expected to be present in solution at high Mo

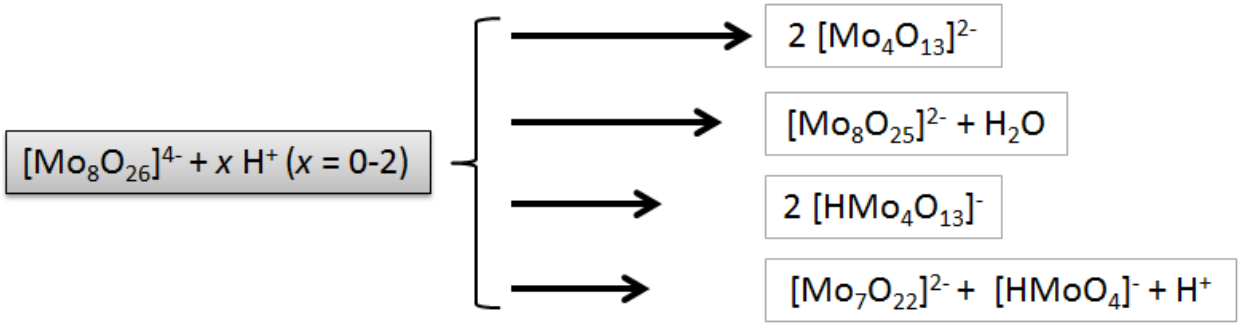

Fig. 3.18: Possible fragmentation processes of the condensed octamolybdates including a varying amount of protons. The length of the arrows symbolizes the probability of the process to take place based on the ion count in the measured spectra of a 350 mM molybdate solution with pH 3.

concentrations. In the mass spectrometer, the following species make up two thirds of the spectrum:

$[Mo_4O_{13}]^{2-}$ (29.4 %), $[HMo_2O_7]^-$ (14.6 %), $[HMo_4O_{13}]^-$ (13.6 %), $[Mo_8O_{25}]^{2-}$ (9.2 %), $[HMo_3O_{10}]^{2-}$ (6.6 %), and $[Mo_7O_{22}]^{2-}$ (6.0 %). This leads to the following fragmentation pathways of the two molybdate species:

Increasing the pH to 5 should lead to heptamolybdate as the single most dominant species, but the spectrum consists to almost three quarters of $[HMo_2O_7]^-$ (24.1 %), $[HMo_3O_{10}]^-$ (22.1 %), $[HMo_4O_{13}]^{2-}$ (18.3 %), and $[Mo_4O_{13}]^{2-}$ (7.4 %). These percentages correspond to the fragmentation patterns shown in Fig. 3.19.

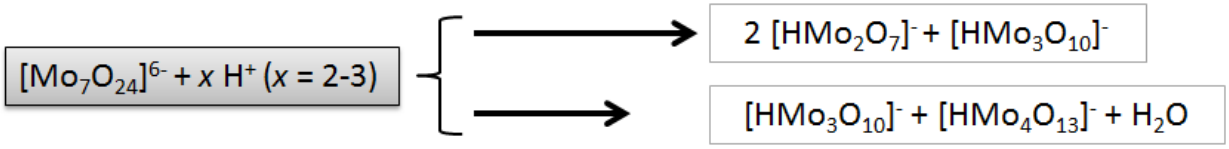

Fig. 3.19: Possible fragmentation processes of the condensed octamolybdates including a varying amount of protons. The length of the arrows symbolizes the probability of the process to take place based on the ion count in the measured spectra of a 0.35 M molybdate solution with pH 5.

It has to be clarified that the mentioned percentages are not used for absolute quantitative analysis, but only for the estimation of the most probable fragmentation patterns.

3.5 Conclusion

Combination of Raman spectroscopy measurements of aqueous molybdate solutions and theoretical calculation of Raman spectra of chosen molybdate species offers an until now unexplored way of identifying molybdate species in solution. The structural development of molybdates in the gas-phase does not follow linear cluster growth, but can be divided into three different structural domains: chains, rings, and Lindqvist-based structures.

The comparison of spectroscopic (experimental and calculated) solution data and mass spectrometric gas-phase data shows a clear difference in speciation diversity between the techniques. This leads to two possible scenarios: (1) due to its higher sensitivity, mass spectrometry displays more species than are visible with spectroscopy or (2) highly charged and condensed polyoxomolybdate species that are not stabilised by larger counter ions are fragmented during ionisation. Taking into account that said species are not found at all in the mass spectra, the last scenario is more likely. Hence, possible and plausible fragmentation pathways for condensed hepta- and octamolybdate species are demonstrated based on the count of ions in the mass spectrometer.

4. Speciation of vanadates in aqueous solution and in the gas-phase

Same as the polyoxomolybdates in chapter 3, the speciation of vanadates in aqueous solution at various vanadium concentrations (10 mM to 0.01 mM) and pH values (2-9) has been examined by Raman and UV-vis spectroscopy to relate it to the consequences for MoV oxide synthesis in chapter 6. The gas-phase composition has been investigated with electrospray ionisation mass spectrometry, while simultaenously the collision cross sections of the singled out molecules have been derived from the measurements via ion mobility spectroscopy. For more structural insights, infrared multiple photon dissociation experiments have been performed as well. The vanadium concentrations have been chosen to be lower than the molybdenum ones based on the usual hydrothermal synthesis approach in which the vanadium concentration is significantly lower than the molybdenum concentration in solution.

4.1 Speciation in aqueous solution

4.1.1 Raman spectroscopy

Raman spectra were only obtainable for solutions with the vanadium concentration of 10 mM and 5 mM, since vanadium oxide species at lesser concentration were not detectable. As it could be seen previously with molybdate solutions, solutions below 7 mM are hardly measurable. Furthermore hydrochloric acid had to be used to adjust the pH value of the 5 mM samples instead of nitric acid, since the NO_3^- signal at 1047 cm^{-1} overshadowed other signals with its intensity. Figure 4.1 shows all Raman spectra for a concentration of 10 mM and 5 mM, depending on their respective pH value.

At vanadium concentrations of 10 mM and with increasing pH value, spectral changes take place. At a pH of 2 a signal at 1047 cm^{-1}, which belongs to HNO_3 – which was used for acidification of the 10 mM V samples –, dominates the spectrum, but two small peaks at around 935 cm^{-1} and 1001 cm^{-1} are also arising.

The latter signal is also present for pH values of 3 and 4, whereas it shifts slightly to lower wavenumbers at pH 5.[142, 162] assigned this to the stretching vibrations of the vanadyl bond in decavanadate species $[V_{10}O_{28}]^{6-}$ and its protonated derivatives. These can be assigned to the stretching vibrations of the vanadyl bond in decavanadate species $[V_{10}O_{28}]^{6-}$ and its protonated derivatives. [142, 162, 163]

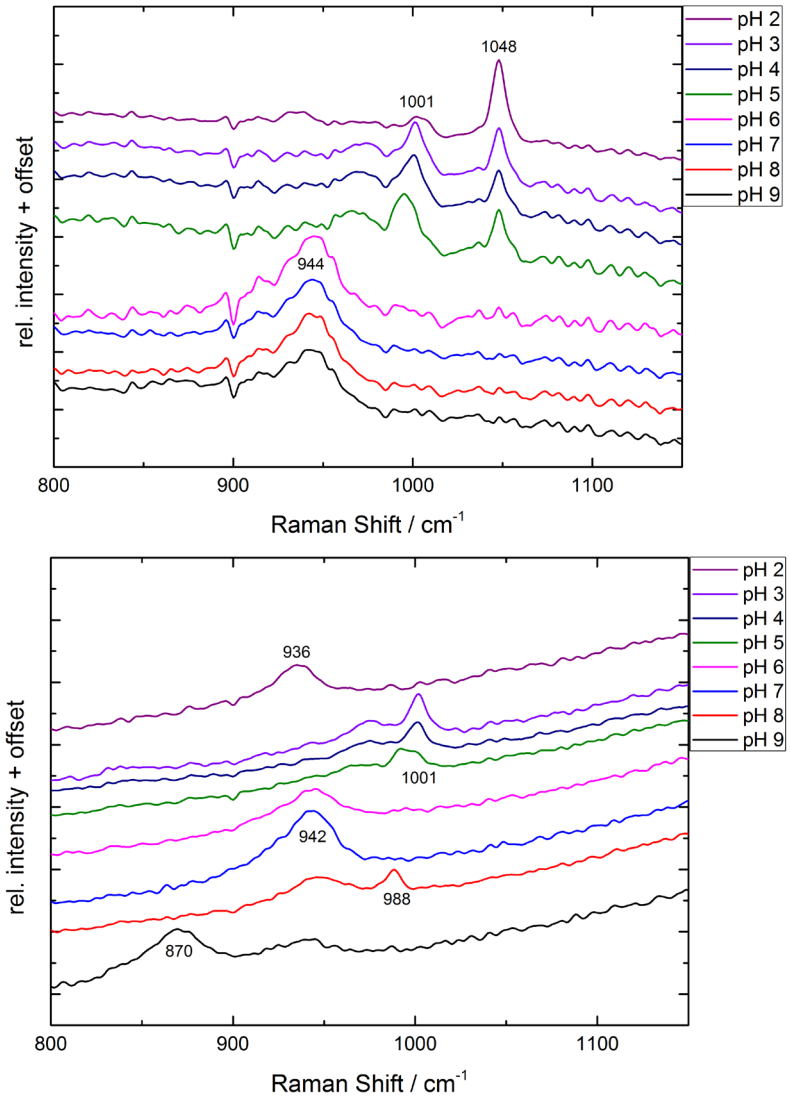

Figure 4.1: Raman spectra of 10 mM (top) and 5 mM (bottom) vanadate solutions at different pH values, measured with a Raman immersion probe at 785 nm.

From pH 6 and higher on the only visible signal is a broad peak at 944 cm^{-1} which is attributed to the symmetric VO_2 stretching vibration of polymeric $[VO_3]_n^{n-}$. Comparing this to the distribution diagram published by Baes & Mesmer[1], their distribution diagram agrees concerning the presence of decavandate from pH 2 to 5, and claims trivanadate $[V_3O_9]^{3-}$ to be the dominant species in this concentration regime and pH values from 6 to 9. This fits with our observation of $[VO_3]_n^{n-}$ in the spectra, since $[V_3O_9]^{3-}$ belongs to these kind of polymeric metavanadates.

At only half the vanadium concentration, the Raman spectra show a more diverse picture. The solution at pH 2 possesses only one signal at 936 cm^{-1}, followed by three almost identical spectra for pH 3-5 with a signal at 1001 cm^{-1} and another possible feature at around 970 cm^{-1}. The following pH values of 6 and 7 show only one signal at around 942 cm^{-1}, which then decreases at pH 8, and another signal at 988 cm^{-1} appears. Lastly, at pH 9 the signal at 942 cm^{-1} is almost gone. Instead, a band at 870 cm^{-1} dominates the spectrum.

Again, the signal at 1001 cm^{-1} (and the adjoining feature at 970 cm^{-1}) can be assigned to decavanadate $[V_{10}O_{28}]^{6-}$, and the band at around 942 cm^{-1} to polymeric $[VO_3]_n^{n-}$ like $[V_3O_9]^{3-}$. It is possible, that the signal at 936 cm^{-1} in the solution of pH 2 belongs to the same structural species type, as well. The new peak at 877 cm^{-1} is assigned to the symmetric stretching vibration of VO_2 in the monomeric $[VO_4]^{3-}$[142, 162]. The signal at 988 cm-1 remains unidentified up to this point.

Using these peak assignments to determine the relative concentration of species in the solutions leads to the species distribution in Fig. 4.2. It is obvious, that the distribution of vanadate species is straighter forward than of molybdate species, because there are maximum two species present at the same time.

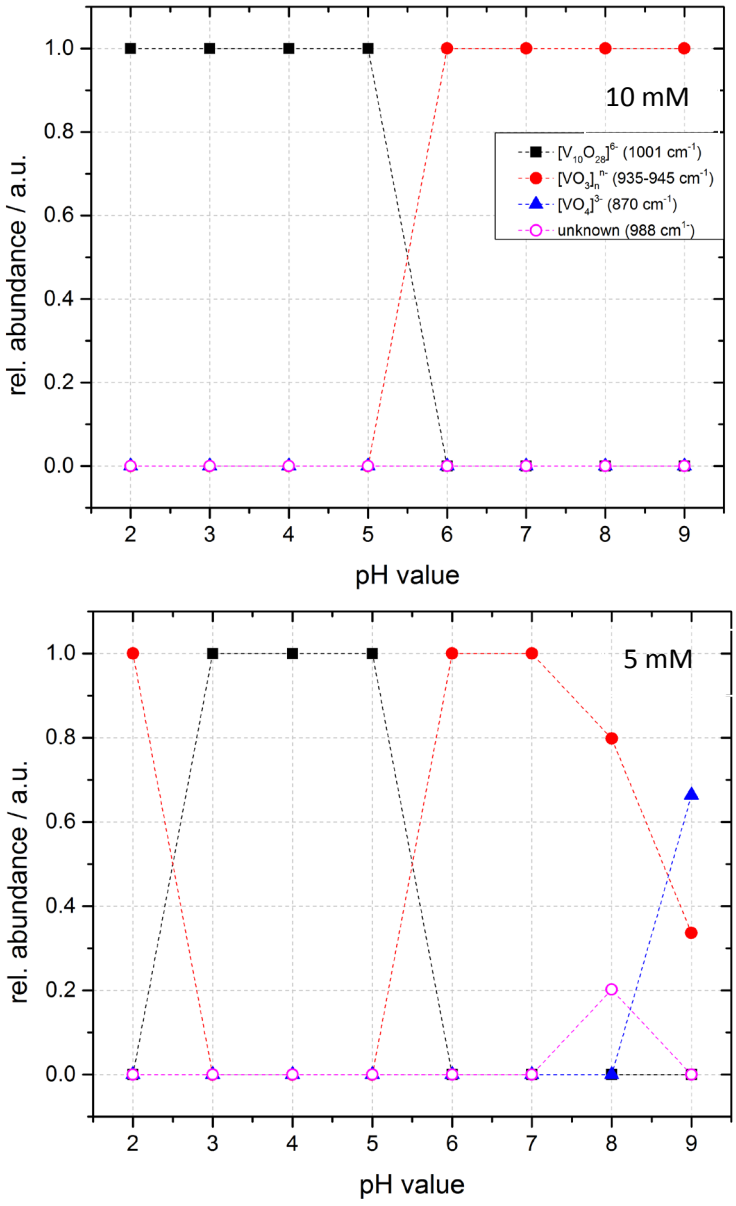

Fig. 4.2: Relative concentrations of vanadate species in aqueous solution depending on the pH value, derived from spectral deconvolution of Raman measurements.

In summary, decavanadate $[V_{10}O_{28}]^{6-}$ appears to be present at vanadium concentrations of 10 mM from pH 2 to 5, and at concentrations of 5 mM from pH 3 to 5. Polymeric $[VO_3]_n^{n-}$ dominates at 10 mM from

pH 6 to 9, and at 5 mM from pH 6 to 8. Still, it is also present at pH 9, but $[VO_4]^{3-}$ is dominating the spectra. Assuming that the polymeric metavanadate is trivanadate $[V_3O_9]^{3-}$ in this case and in all solutions, the measured Raman spectra agree almost completely with the known distribution diagram of vanadate species in aqueous solutions[1].

4.1.2 UV-vis spectroscopy

UV-vis spectra of the vanadate solutions with the highest concentration of 10 mM can be divided into two groups. The solutions with pH 2 to 5 show a signal at 201 nm and 260 nm, whereas the solutions from pH 6 to pH 9 possess bands at 237 nm and 281 nm. The edge at 325 nm is due to the change of lamps in the spectrometer.

Signals around 200 nm can be attributed to the charge transfer between terminal oxygen atoms and vanadium atoms, whereas the signal at 260 nm stems most likely from the charge transfer between bridging oxygen atoms to vanadium. This is often assigned to decavanadate species[164] and fits well with the Raman results for pH 2 to 5. The signals present at higher pH values can be attributed to metavanadate[165] and fit therefore also with the results of the Raman measurements.

Lower concentrations of 5 mM display the same signals for pH 8 and 9. The solutions of pH 2, 3, 6, and 7 show only one signal at 201 nm, belonging to a charge transfer between terminal oxygen and vanadium atoms. This being the sole signal hints at a monomer with only one type of V-O bonds. Lastly, solutions with pH 4 and 5 show the same signals as at a vanadium concentration of 10 mM (200 nm and 260 nm), leading to the assumption that decavanadate is dominant in these solutions.

Vanadium concentrations of 1 mM and below show identical spectra with only one signal at 200 nm, except for the solutions at pH 9. In these cases, there is a local maximum at 260 nm (1 mM solution) or none at all. For the solutions with a local maximum absorption at 200 nm, the presence of mononuclear species can be assumed since only the charge transfer between terminal oxygen and vanadium is detectable. For the remaining three solutions at pH 9, the existence of a different kind of monovanadate might be a plausible assumption. The UV-vis spectra of the 10 mM solutions fit with the aforementioned Raman measurements and the literature, but at lower concentrations there is no complete agreement between the different spectroscopic measurements and the speciation claimed to be present in literature, according to which decavanadate and trivanadate should be dominant species until 1 mM and partially even 0.1 mM vanadium.

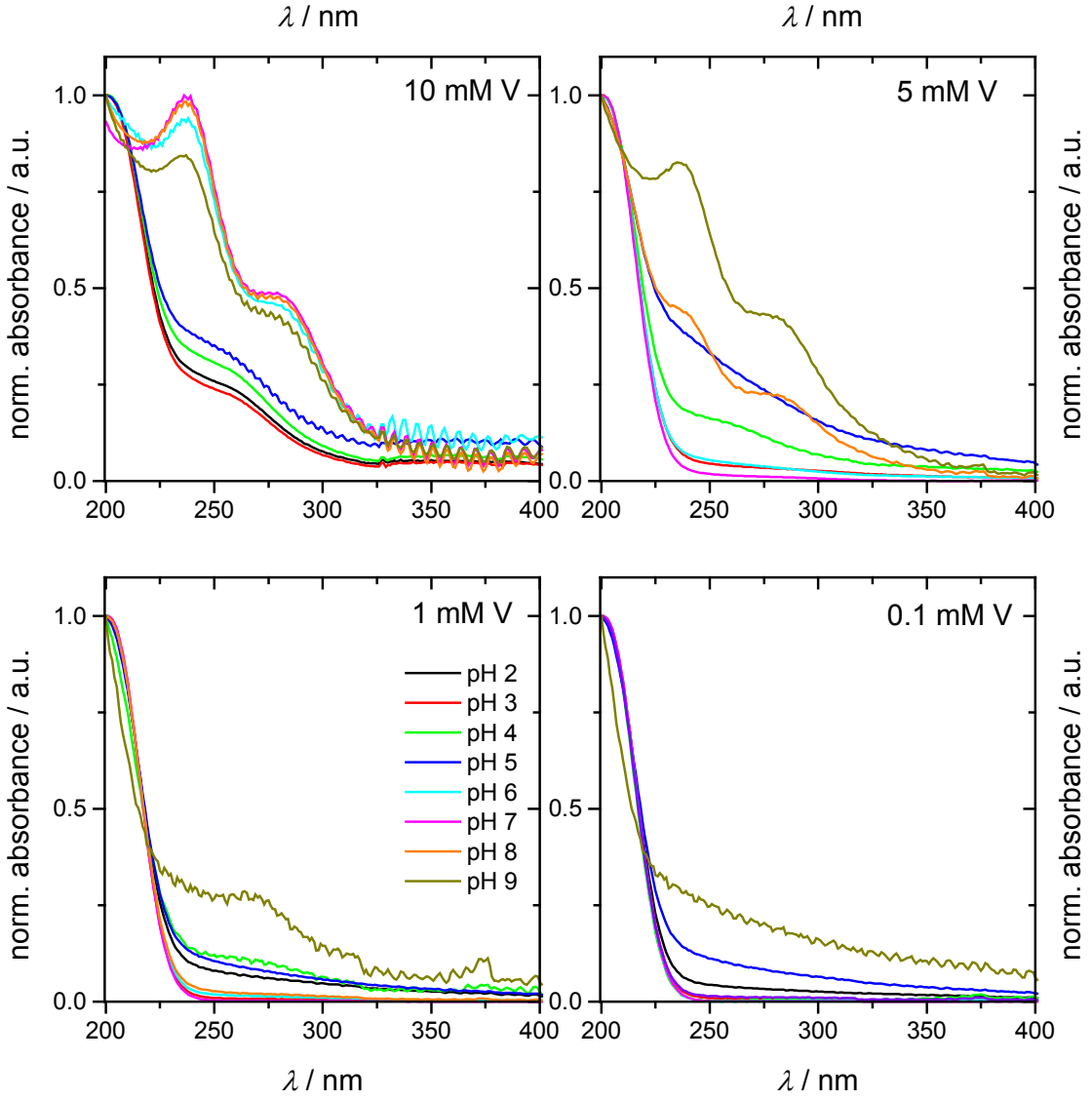

Fig. 4.3: UV-vis spectra of different vanadate solutions, sorted by V concentration and pH value.

4.2 Speciation in the gas-phase

4.2.1 Influence of ionisation parameter changes to the vanadate speciation

In the case of molybdate solutions, the variation of ionisation parameters did not have any influence on the speciation in the gas-phase. To see, if this is the same case for vanadates, three different voltages in the mass spectrometer were varied, the corresponding spectra are shown in Fig. 4.4.

The varied voltages are as follows: Middle voltage V_{mis}, which is applied in a narrow region in the middle of the entrance funnel, and leads to higher collision of the molecules if the voltage is lowered; entrance voltage V_{ent}, which resembles the radio frequency in the entrance of the ion funnel and is responsible for more heating and with that harsher conditions, if it is increased; and the injection voltage V_{inj}, which is the voltage applied for the injection of the ions into the drift tube, and leads to harsher conditions in the form of increased collisional activation if raised.

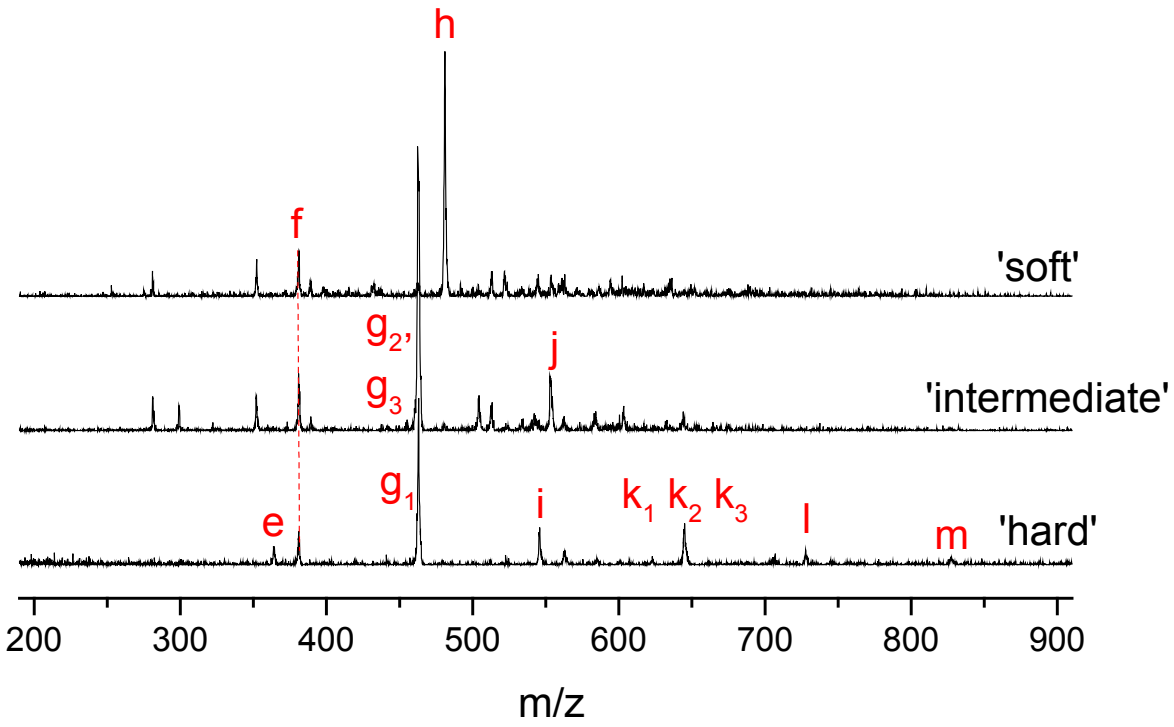

Fig. 4.4: Mass spectra of aqueous vanadate solution of 5 mM vanadium and pH 2 under different ionisation parameters.

The in Fig. 4.6 denoted conditions “soft”, “intermediate”, and “harsh” correspond to the following combinations of the three aforementioned voltages:

Soft: V_{mid} = 40 V; V_{ent} = 180-200 V, V_{inj} = 30 V

Intermediate: V_{mid} = 15 V; V_{ent} = 180-200 V, V_{inj} = 60 V

Harsh: V_{mid} = 15 V; V_{ent} = 360-380 V, V_{inj} = 150 V

The labels of the marked m/z ratios in Fig. 4.4 belong to the species found in Tab. 4.1.

Tab. 4.1: Label assignment of vanadate species found under different ionisation voltages.

label	assignment	*m/z*	
		observed	expected
e	$V_4O_{10}^{\bullet-}$	364	363.7
f	$HV_4O_{11}^{-}$	381	380.7
g_1 **g_2/g_3**	$V_5O_{13}^{-}$ $V_{10}O_{26}^{2-}$	463	462.7
h	$H_4V_{10}O_{28}^{2-}$	481	480.7
i	$V_6O_{15}^{\bullet-}$	546	545.6
j	$V_{12}O_{31}^{2-}$	554	553.6
k_1 **k_2/k_3**	$V_7O_{18}^{-}$ $V_{14}O_{36}^{2-}$	645	644.5
l	$V_8O_{20}^{\bullet-}$	728	727.5
m	$V_9O_{23}^{-}$	827	826.4

It is clearly visible that the different conditions lead to a variety of species present in the mass spectra, especially the change in species from intermediate to harsh conditions is prominent. The spectrum at harsh conditions is dominated by the signal for pentavanadate g_1 $[V_5O_{13}]^-$, and accompanied by heptavanadate k_1 $[V_7O_{18}]^-$, two different structural forms of $[V_{14}O_{36}]^{2-}$ (k_2 & k_3), hexavanadate $[V_6O_{15}]^{\bullet-}$ (i), tetravanadates $[HV_4O_{11}]^-$ (f) and $[V_4O_{10}]^{\bullet-}$ (e), octavanadate $[V_8O_{20}]^{\bullet-}$ (l), and nonavanadate $[V_9O_{23}]^-$ (m). Going to intermediate conditions changes the spectrum drastically, specifically in the regard of the signal at m/z 463 which first belonged to pentavanadate. At softer conditions two different structures of decavanadate $[V_{10}O_{26}]^{2-}$ (g_2 & g_3) are present instead. Additionally, $[V_{12}O_{31}]^{2-}$ (j) and again $[HV_4O_{11}]^-$ (f) are visible in the spectrum as well.

Going to even softer conditions makes it possible to detect the protonated form of the octahedral decavanadate $[H_4V_{10}O_{28}]^{2-}$ (h) which is claimed to be present in solution at this vanadium concentration and pH value. Furthermore $[HV_4O_{11}]^-$ (f) is still present as only species from the other measurements.
Hence, in the case of vanadates the ionisation conditions have a great influence of the species present in the mass spectra, leading to more compact and higher nuclear species. When the same conditions were applied to molybdate solutions, no change in speciation was detected, showing that the highly condensed molybdate species fragment either way during desolvation. The protons necessary for charge compensation and thus stability are more tightly bound to vanadate structures than to molybdate ones.

4.2.2 Mass spectrometry

Mass spectra for all vanadate solutions have been recorded under the same soft ionisation conditions as stated in the previous sub-chapter. The mass spectra of the examined vanadate solutions are dominated by more than just one signal at any given vanadium concentration and pH value. A variety of different species, ranging from three to ten vanadium atoms in the cluster, can be found in most of the solutions, whereby monovanadates are usually only found at higher pH values and low concentrations.
For example, at a concentration of 10 mM vanadium and a pH of 3, the following species can be found: $[V_3O_8]^-$ (*m/z* 281), $[HV_7O_{19}]^{2-}$ (*m/z* 331), $[V_8O_{21}]^{2-}$ (*m/z* 372), $[HV_4O_{11}]^-$ (*m/z* 381), $[V_5O_{13}]^-$ (*m/z* 463), $[H_4V_{10}O_{28}]^{2-}$ (*m/z* 481), $[H_4V_5O_{15}]^-$ (*m/z* 499). The respective mass spectrum is shown in Fig. 4.5.
The mass spectrum for a solution of a lower concentration (e.g. 0.1 mM) and a pH of 9, however, is dominated by species of $[H_2VO_4]^-$ (*m/z* 116), and $[HV_3O_9]^-$ (*m/z* 143). Compared to molybdate species[149], the measured vanadates do not completely follow one or two formal series. The only series which can be attributed are $[V_{2m+1}O_{5m+3}]^-$ (m = 1-3) and $[HV_{4m+2}O_{10m+6}]^-$ (m = 1-2).

Again, Walanda et al.[166, 167] detected a multitude of protonated and deprotonated vanadate species with up to 17 vanadium atoms in the cluster at a solution pH value of 4.5. The solutions they investigated had a vanadium concentration of 1 mM as well, but they used a higher capillary voltage. Thus, it comes hardly as a surprise that the most dominant species in their measurements is $[H_2VO_4]^-$. A predominance diagram of vanadate species, dependent on the vanadium concentration and the pH value of the solution, was created based on the aforementioned MS data (Figure 4.6).

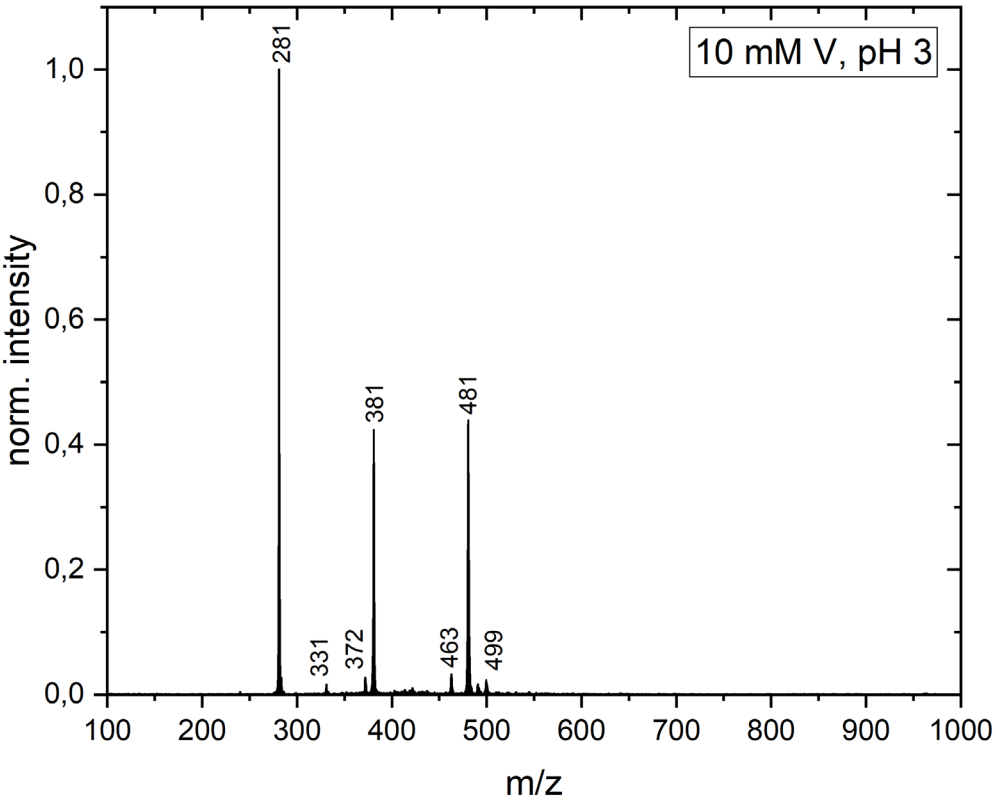

Fig. 4.5: Mass spectrum of 10 mM vanadate solution adjusted to pH 3.

The solutions with the highest vanadium concentration of 10 mM are dominated by trivanadate $[V_3O_9]^-$ and decavanadate $[H_xV_{10}O_{28}]^{x-6}$. The solutions of 5 mM vanadium concentration show a similar distribution across the chosen pH range. At 1 mM, all solutions except for pH 4 and 5 (which are dominated by decavanadate) show a wide abundance of trivanadates (pH 5-9) and decavanadates (pH 3-4), whereas at even lower concentrations of 0.1 mM, almost only monovanadates are present in the spectra for pH values of 5 and higher.

Comparing this predominance diagram with the known diagrams in literature[1, 100] reveals similar results. According to literature, decavanadate $[V_{10}O_{28}]^{6-}$ and its protonated derivatives are present at pH values from 2 to almost 6, even down to concentrations of 0.1 mM with a pH of 4. Furthermore, trivanadate $[V_3O_9]^-$ dominates from pH 6 to pH 8 at concentrations from 10 mM down to 0.3 mM. The rest is dominated by monovanadates in the examined concentration and pH range. This fits quite well regarding decavandate and also the monovanadates. Only trivanadate is not that dominant at higher concentrations and pH values, it is only one of many species present in roughly the same concentration.

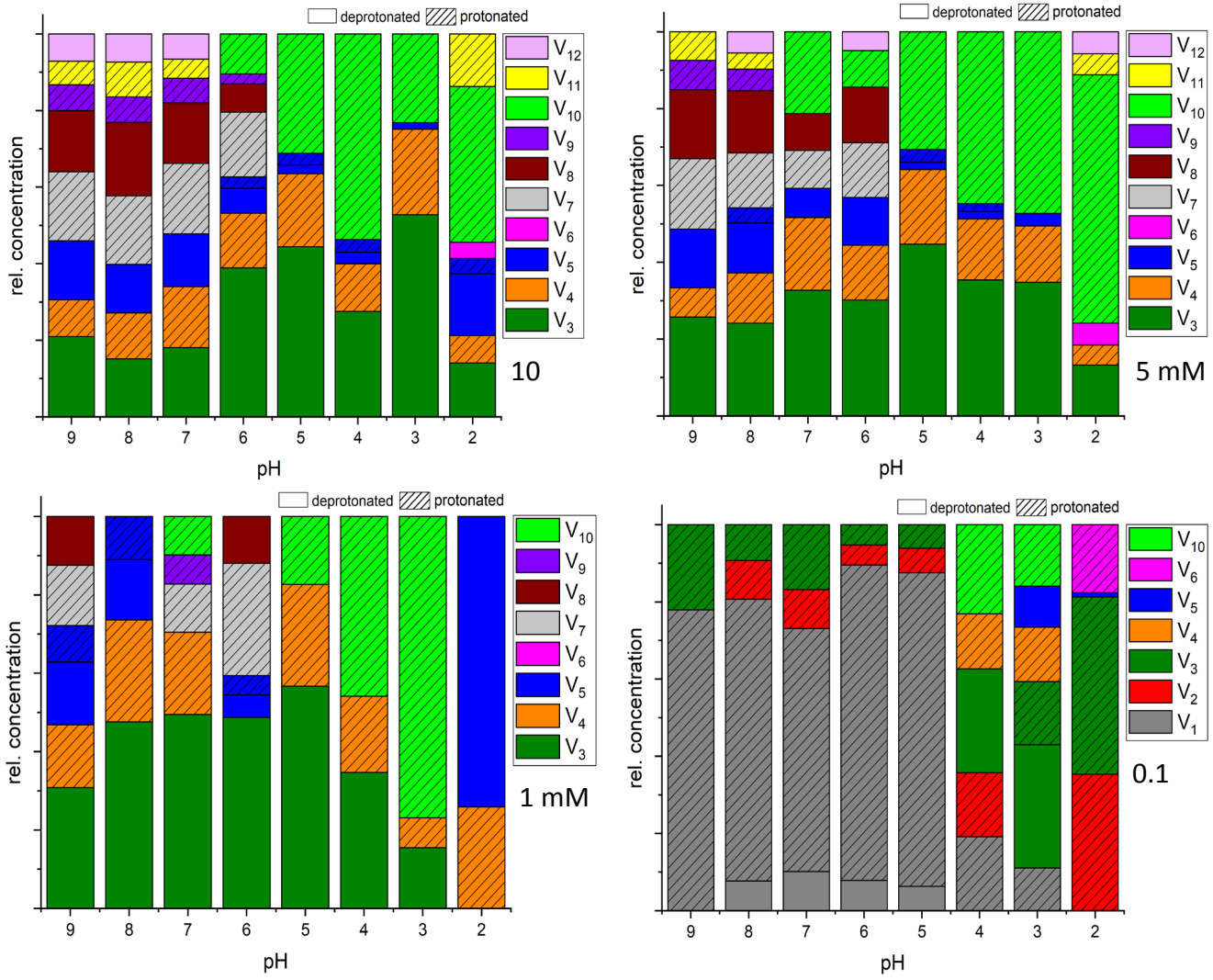

Figure 4.6: Predominance diagram of all vanadate species present in the examined solutions, depending on their pH value and V concentration.

4.2.3 Ion mobility and collision cross sections

Ion mobility measurements make it possible to monitor how many species with the same m/z ratio are present in the mass spectrum. Plotting the ion abundance against the drift time through the drift tube, leads to peaks as shown in Fig. 4.7. Each species possesses its unique drift time and can therefore be determined or singled out. As can be seen, in the case of the m/z 645 signal, there are four distinct peaks and thus four distinct species present independent of the ionisation conditions, of which three can be assigned. From these drift times, the collision cross section of the vanadates can be derived as has been explained in chapter 3.2.2.

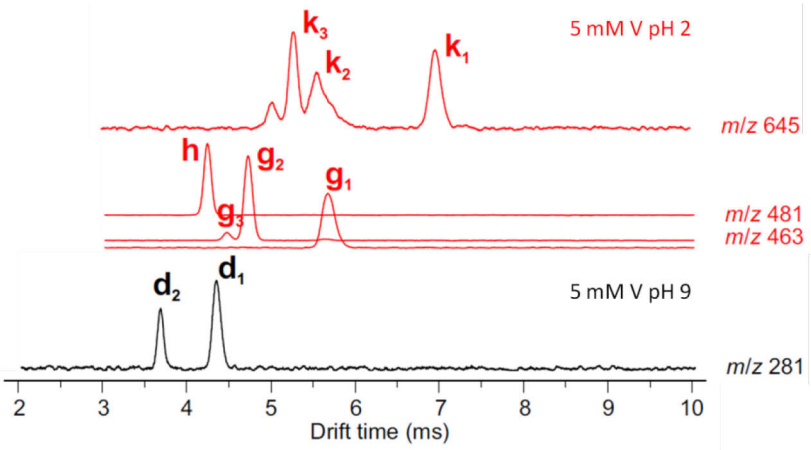

Fig. 4.7: Drift times of different vanadate species.

There is a variety of different structural possibilities for the respective signals and sum formulas. Structures, which have been used to calculate CCS for comparison, are shown in Fig. 4.8 and the respective CCS, measured and calculated, can be found in Tab. 4.2.

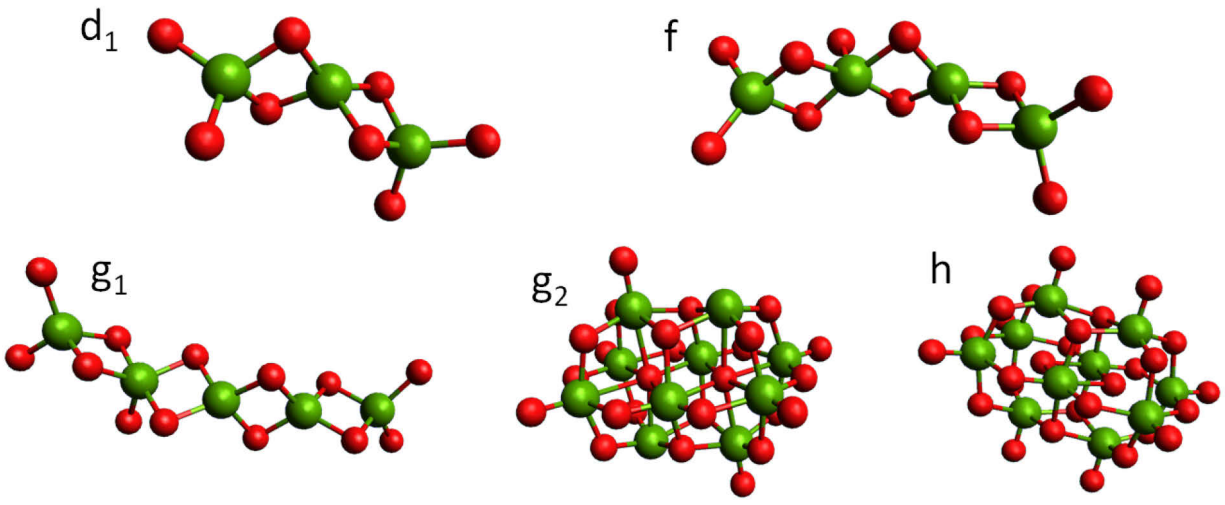

Fig. 4.8: Possible structures for vanadates found in the mass spectra and used for CCS calculations.

Tab. 4.2: Different vanadate species found in the mass spectra together with their respective measured CCS, compared to the CCS of the structures suggested in Fig. 4.8.(* calculation only for deprotonated $[V_{10}O_{28}]^{6-}$)

label	assignment	*CCS*	
		observed	calculated
d_1	$V_3O_8^-$	60.1	74.4
d_2	$V_6O_{16}^{2-}$	-	-
f	$HV_4O_{11}^-$	76.7	95.9
g_1	$V_5O_{13}^-$	84.2	110.7
g_2/g_3	$V_{10}O_{26}^{2-}$	144.2 (**g_2**) / - (**g_3**)	183.7
h	$H_4V_{10}O_{28}^{2-}$	132.1	122.7*
k_1	$V_7O_{18}^-$	105.8	-
k_2/k_3	$V_{14}O_{36}^{2-}$	- (**k_2**) / 155.1 (**k_3**)	-

When it comes to collision cross sections, a deviation of the calculated value from the measured one of about 10 % is considered to be a good fit. For the structures shown above, only the calculated value for decavanadate $[H_4V_{10}O_{28}]^{2-}$ appears fitting. The calculation took place without the four protons present, hence it can be expected that the value for the calculated CCS is bigger and more fitting if the protons were taken into account. This agreement shows that the decavanadate structure found in the mass spectrum under soft conditions is the same as in the known crystal structure.

Losing two oxygen atoms seems to lead to a rearrangement of the decavanadate structure, since the calculated and measured CCS show a strong discrepancy. In general, all measured structures appear to be more compact than the suggested ones used for the CCS calculations.

4.2.4 Infrared multiple photon dissociation

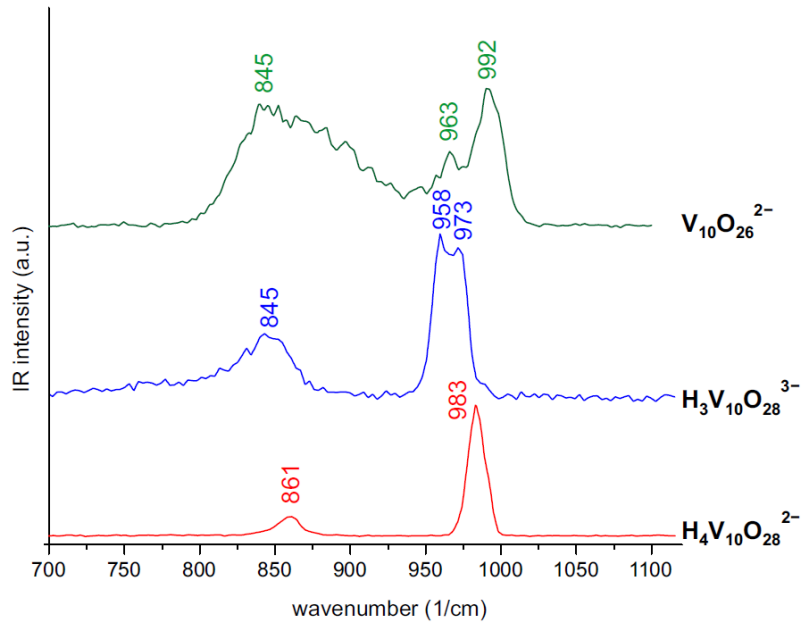

Fig. 4.9: IR spectra of different decavanate species as found in mass spectra.

To get an impression about the structural diversity among the detected vanadate species, infrared spectra of the single species have been measured. As it was mentioned in the chapter before, it is likely that decavanadate $[H_4V_{10}O_{28}]^{2-}$ structurally rearranges when losing two water molecules to form $[V_{10}O_{26}]^{2-}$. The IR spectra of different decavanadate structures are shown in Fig. 4.9. Protonated decavanadate with 28 oxygen atoms shows two narrow signals in the IR spectrum: one around 850 cm^{-1} (asymmetric V-O-V stretching vibrations) and one around 970 cm^{-1} (V=O stretching vibrations). This is comparable with the assignments based on IR measurements of decavanadate containing minerals[168]. When two water molecules are deducted from the structure, the signal for the asymmetric V-O-V vibrations becomes very broad and reaches from 800 to 925 cm^{-1}. The V=O signal also blue shifts to 992 cm^{-1}. This might be another indication for the structural rearrangement.

Fig. 4.10 and 4.11 show an overview of all IR spectra of singly and doubly charged vanadate species, respectively. Regarding singly charged species, the structures present in the alkaline solution $[H_2VO_4]^-$ (a), $[HV_2O_6]^-$ (c), and $[V_3O_8]^-$ (d1) only show signals for the V=O stretching vibrations, albeit shifting to higher bonding energy. This indicates that these species most likely belong to one type of structure.

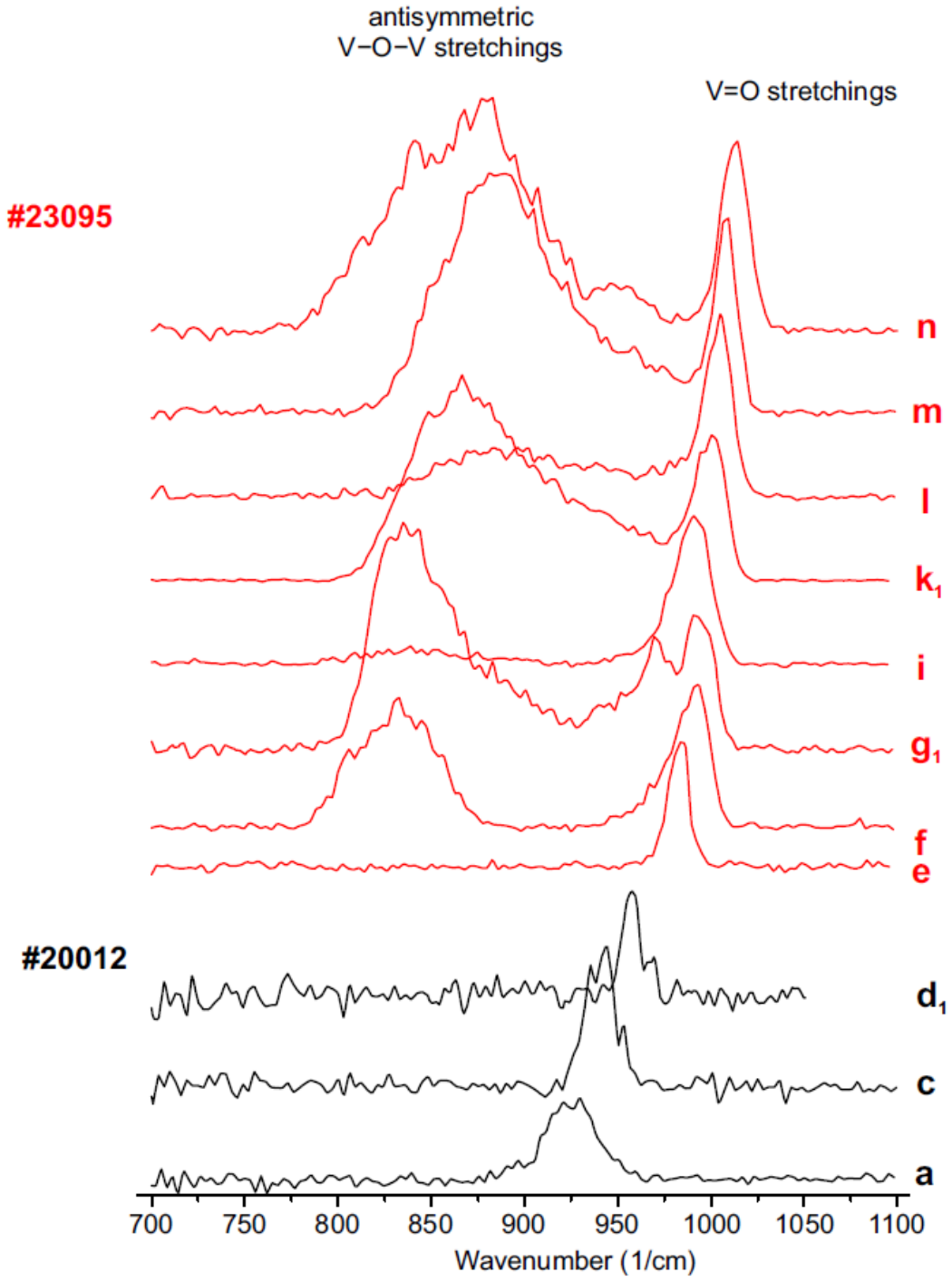

Fig. 4.10: Measured IR spectra of singly charged vanadate clusters of two different solutions. #23092: 5 mM V pH 2; #20012 5 mM V pH 9.

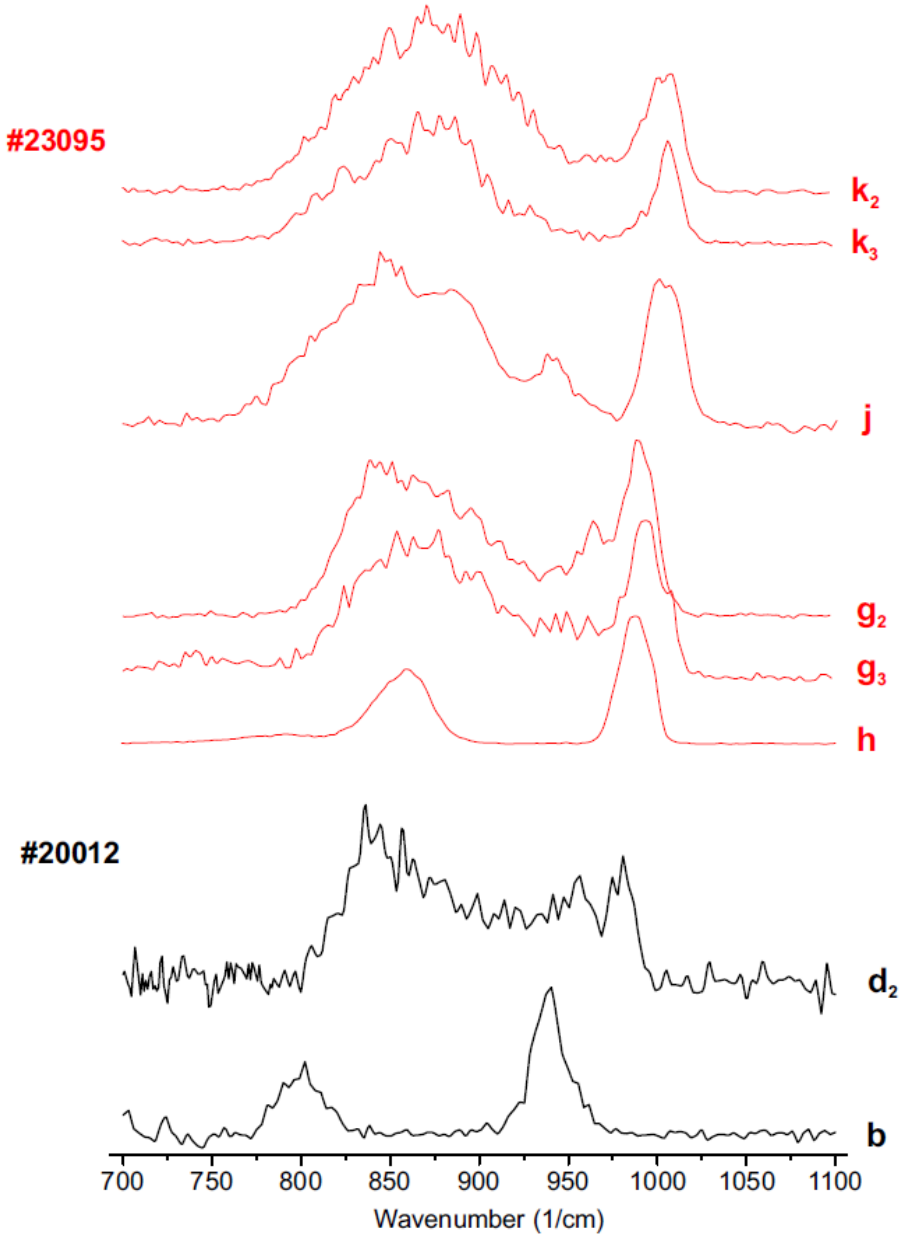

Fig. 4.11: Measured IR spectra of doubly charged vanadate clusters of two different solutions. #23092: 5 mM V pH 2; #20012: 5 mM V pH 9.

Increasing the nuclearity from three to four vanadium atoms (f) leads to the appearance of bands in the V-O-V stretching vibration area. The maxima of these bands as well as the maxima of the V=O

vibrational bands shift to higher wavenumbers with growing number of vanadium atoms in the clusters. Furthermore, the bands of the V-O-V vibrations become broader.

The presumably radical species (e, i, l), however, show only very weak bands in the region of V-O-V stretching vibrations, if any. This indicates a great structural difference between radical and non-radical vanadate species. At any rate, the singly charged species can be divided into at least three structural groups: the small vanadate clusters with up to three or four vanadium atoms, the bigger clusters from four vanadium atoms upwards, and the radical clusters.

All doubly charged vanadate species possess signals in both the wavenumber area of asymmetric V-O-V stretching vibrations and V=O stretching vibrations. The smallest molecule $[V_4O_{11}]^{2-}$ (b) shows two narrow signals at 800 cm^{-1} and 940 cm^{-1}. Adding two vanadium atoms leads to two not clearly separable signals. However, this is not due to the structure of the species, but the poor spectral quality due to the low concentration of the vanadate in the mass spectrum.

Going from decavanadate to clusters with fourteen vanadium atoms shows no obvious change in spectra, only the V=O vibration signal shifts continuously to higher wavenumbers – as is the case for the singly charged species as well – and the band in the V-O-V stretching vibration area becomes slightly broader. It appears that in the case of doubly charged vanadates no different structural regimes can be found.

4.3 Conclusion

Until now, there are still uncertainties about the presence of different vanadate species in aqueous solution under different conditions like the pH value or vanadium concentration. Spectroscopic investigations of a wide array of vanadate solutions have shown that only three different species are present in the concentration regime of 10 mM and 5 mM vanadium: decavanadate $[V_{10}O_{28}]^{6-}$, polymeric metavanadate $[VO_3]_n^{n-}$, and $[VO_4]^{3-}$.

Transferring these species from solution into gas-phase leads to a multitude of different species visible in the mass spectrum. However, compared to molybdates, vanadates turned out to be very sensitive to the voltages applied during ionisation and transfer within the spectrometer. Thus, applying very soft conditions and minimising the collision probability, makes it possible to detect highly molecular species in the mass spectrum, as has been shown for decavanadate $[V_{10}O_{28}]^{6-}$.

Under harsher conditions, decavanadate loses two of its oxygen atoms, causing a structural rearrangement, as it is suggested by comparing calculated and measured collision cross sections, and recording infrared multiple photon dissociation spectra. Furthermore, the recorded IRMPD spectra of all singly and doubly charged vanadates found in the mass spectra suggest three different structural motifs for different groups of vanadates: small vanadate clusters with up to three or four vanadium atoms, bigger clusters from four vanadium atoms upwards, and radical clusters.

DTF calculations to determine the structure of the vanadate species present in the gas-phase will be carried out in the future.

5. Speciation of mixed MoV species in aqueous solution and in the gas-phase

The consequences for POM speciation in mixed MoV solutions have been investigated in hindsight to them serving as precursor species for the synthesis of $MoVO_x$ with M1 structure, as has been pointed out before. Further investigation of the structural dependency on total metal concentration, and with that precursor species was performed with Raman spectroscopy regarding the speciation in the liquid phase, and ESI-MS for the speciation in the gas-phase.

5.1 Speciation in aqueous solution

5.1.1 Raman spectroscopy

Both metavanadate $[VO_3]^-$ and vanadyl species $[VO]^{2+}$ have been used as vanadium source for mixed MoV solutions. Furthermore, different total metal concentrations of 4:1 Mo/V solutions were chosen for examination. The Mo-V ratio of 4:1 was chosen, because this ratio is usually applied for $MoVO_x$ synthesis. If necessary, the pH value of the solutions was adjusted to around 4.2, which is also the pH value for the precursor solution applied in hydrothermal synthesis.

The corresponding Raman spectra for all six solutions are shown in Fig. 5.1. The top spectra show the solutions produced with NH_4VO_3 as V source, and show four distinct features. Signals at 915, 950, and around 968 cm^{-1} can be attributed to α- and β-$[Mo_8O_{26}]^{4-}$ present in solutions, which might be substituted with one or two vanadium atoms like in the known mixed species β-$[Mo_7VO_{26}]^{5-}$[114], α-$[Mo_7VO_{26}]^{4-}$, α- or β-$[H_2Mo_6V_2O_{26}]^{5-}$[115]. The substitution fits with the shift of the Raman bands to 950 and 966 cm^{-1} compared to the 956 and 969 cm^{-1} usually attributed to octamolybdates. The remaining signal at 994 cm^{-1} belongs to stretching vibrations of free V=O bonds which cannot be attributed unambiguously.

When the total metal concentration in the solution is decreased, the signal at 994 cm^{-1} starts to dominate the spectrum, whereas the signals for octamolybdate decrease. The latter is not surprising, since higher condensed molybdate species are rarely present at concentrations this low[100].

Using $VOSO_4$ instead of NH_4VO_3 leads to the spectra shown in Fig. 5.1 bottom. The spectrum at 250 mM metal concentration shows an intense signal at around 870 cm^{-1}, a smaller feature at 966 cm^{-1} with a shoulder at around 950 cm^{-1}, and another low intensity signal at roughly 990 cm^{-1}. The first signal is widely attributed to the supramolecular Keplerate species $\{Mo_{72}V_{30}\}$, which serves as a crucial precursor species for the synthesis of M1 structure MoV oxide[169]. The remaining signals can be assigned to the same species as in the spectra with $[VO_3]^-$.

Also, these signals behave the same like in the case of metavanadate-based MoV solutions with decreasing metal concentration: the V=O stretching signal increases compared to the molybdate signals. Additionally, the signal at 870 cm^{-1} of the Keplerate species shifts slightly to lower wavenumbers and loses intensity compared to the remaining isopolyoxometalate species. A summary of all signals and their assignments can be found in Tab. 5.1.

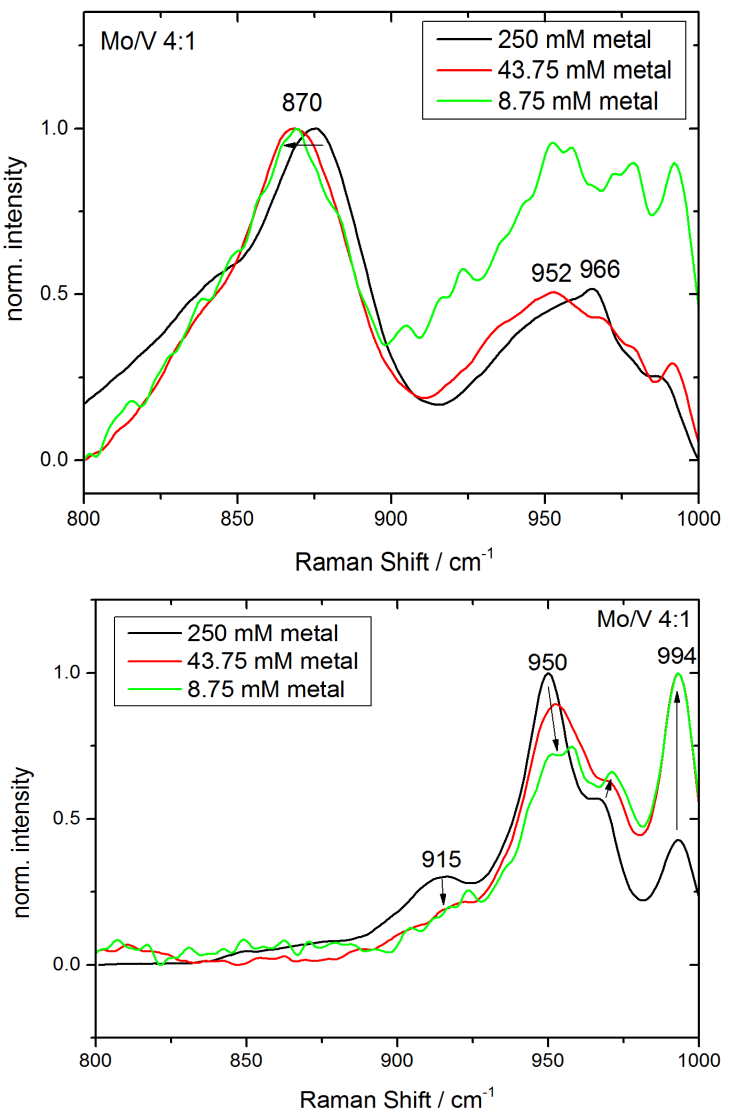

Fig. 5.1: Raman spectra of aqueous MoV solutions with a Mo/V ratio of 4:1 and different concentrations. Solutions with $[VO_3]^-$ as V source at the bottom, with $[VO]^{2+}$ species at the top.

These results clearly support the assumption that vanadyl species and with that V(IV) play a central role in the formation of the Keplerate and hence the final M1 structure[117, 170]. This cannot only be explained by the difference in oxidation state of vanadium, but also by the different structure and charge state which comes with the coordination of the metal atom.

Tab. 5.1: Assignments of Raman signals in mixed MoV solutions.

MoV solutions with $[VO]^{2+}$			MoV solutions with $[VO_3]^-$		
Band / cm^{-1}	Vibration	Species	Band / cm^{-1}	Vibration	Species
870		$\{Mo_{72}V_{30}\}$	915	ν_{as}(Mo-O_t)	$[Mo_8O_{26}]^{4-}$
952	ν_s(Mo-O_t)	α-$[Mo_8O_{26}]^{4-}$	950	ν_s(Mo-O_t)	α-$[Mo_8O_{26}]^{4-}$
966	ν_s(Mo-O_t)	β-$[Mo_8O_{26}]^{4-}$	968	ν_s(Mo-O_t)	β-$[Mo_8O_{26}]^{4-}$
990	ν(V=O)	$[VO]^{2+}$	994	ν(V=O)	$[VO_3]^-$

5.1.2 UV-vis spectroscopy

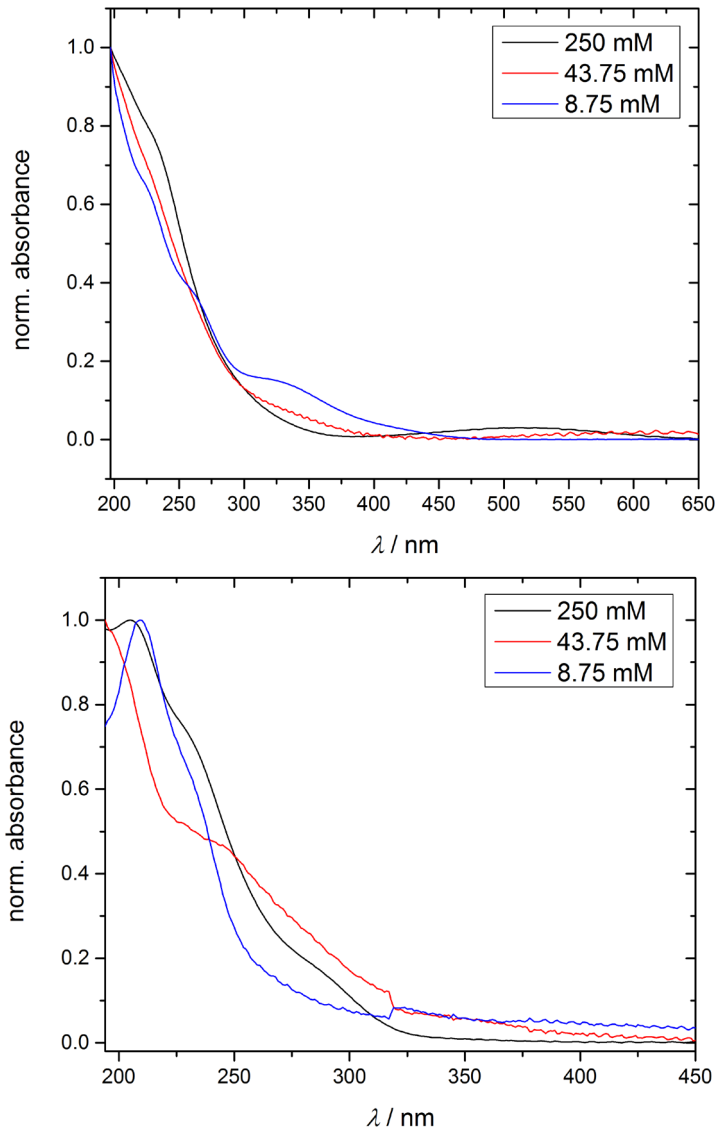

Fig. 5.2: UV-vis spectra of mixed MoV solutions (Mo/V 4:1) with different V precursors at different total metal concentrations. Top: $VOSO_4$ as V source, bottom: NH_4VO_3.

As well as the Raman spectra, the UV-vis spectra of the MoV solutions with different vanadium precursors differ a lot. The spectra are shown in Fig. 5.2 with the vanadyl containing solutions on top, and the metavanadate containing in the bottom.

Of all solutions with $[VO]^{2+}$, only the one with the highest metal concentration (black line) shows a broad signal between 475 and 550 nm. This is generally attributed to intervalence charge transfer from V^{4+} to Mo^{6+} and taken as an indicator for the presence of Keplerate $\{Mo_{72}V_{30}\}$[116]. This signal vanishes with decreasing concentration, indicating a drastic reduction of Keplerates in the solution. Instead, signals at 228, 265 and 331 nm become more pronounced. The latter signifies the charge transfer from oxygen to vanadium, whereas the band at 228 nm

belongs to the charge transfer from oxygen to molybdenum, and the signal 265 nm can belong to both a charge transfer from O^{2-} to Mo^{6+}[146] and from O^{2-} to V^{4+}[171]. This supports the assumption that with lower total metal concentration there is less Keplerates and instead more isopolyoxometalate species present in solution.

The solutions with metavanadate as vanadium source show no signals above 350 nm at any concentration, indicating that no Keplerate species is present in solution. Instead, a signal at 204 nm and shoulders at 230 and 285 nm are present for the highest metal concentration, attributable to charge transfer from oxygen to vanadium and/or molybdenum for 204 and 230 nm, and to a charge transfer between oxygen and molybdenum which is indicative of heptamolybdate $[Mo_7O_{24}]^{6-}$.

Lowering the metal concentration to 43.75 mM leads to only one signal at 247 nm, and further lowering to 8.75 mM to a signal at 209 nm and a shoulder at 232 nm. The latter can be attributed to charge transfers from oxygen to vanadium as well as to molybdenum both indicative of either monovanadate species or heptamolybdate as mentioned before.

All bands and their assignments are summed up in Tab. 5.2.

Tab. 5.2: Assignments of UV-vis signals in mixed MoV solutions.

MoV solutions with $[VO]^{2+}$			**MoV solutions with $[VO_3]^-$**		
λ / nm	Charge transfer	Species	λ / nm	Charge transfer	Species
228	$O^{2-} \rightarrow Mo^{6+}$	MoO_x	204-209	$O^{2-} \rightarrow Mo^{6+}$ $O^{2-} \rightarrow V^{5+}$	MoO_x VO_x
265	$O^{2-} \rightarrow Mo^{6+}$ $O^{2-} \rightarrow V^{4+}$	MoO_x VO_x	230-247	$O^{2-} \rightarrow Mo^{6+}$ $O^{2-} \rightarrow V^{5+}$	MoO_x VO_x
331	$O^{2-} \rightarrow V^{4+}$	VO_x	285	$O^{2-} \rightarrow Mo^{6+}$	$[Mo_7O_{24}]^{6-}$
450-550	$V^{4+} \rightarrow Mo^{6+}$	$\{Mo_{72}V_{30}\}$			

5.2 Speciation in the gas-phase

Mass spectra of the different solutions have been measured. Herein, the measurement conditions already applied in the investigation of molybdate solutions have been used, since molybdenum is the main component of these mixed MoV solutions. The spectra of the different solutions with 43.75 mM total metal concentration are shown in Fig. 5.3. All present species present in the mass spectra and their

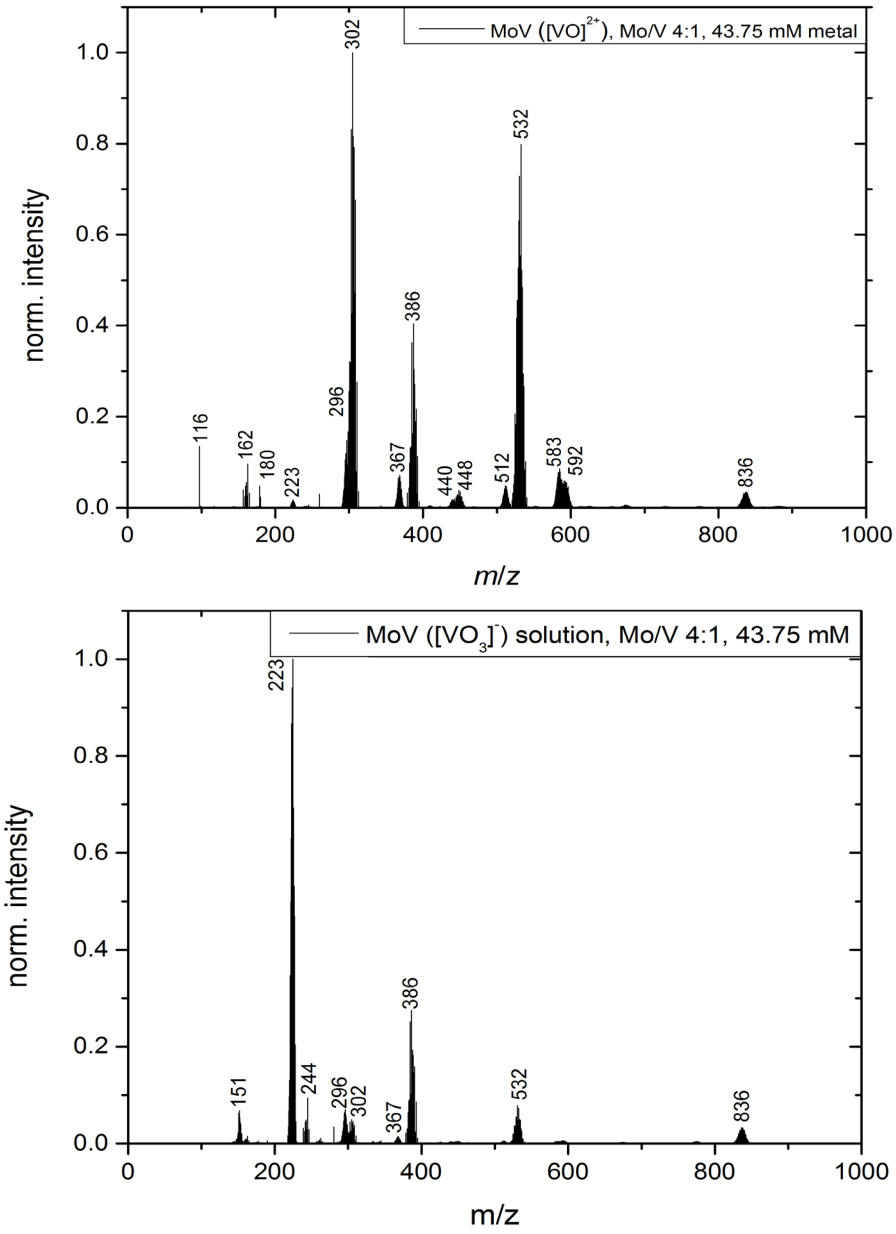

Fig. 5.3: Mass spectra of aqueous mixed MoV solutions with $VOSO_4$ (top) and NH_4VO_3 (bottom) as vanadium source.

respective normalised intensities are listed in Tab. 5.3.

Tab. 5.3: All species found in the mass spectra of respective MoV aqueous solutions with their normalised intensities at each metal concentration.

species	m/z	MoV sol. with $[VO]^{2+}$ Norm. intensity / %			MoV sol. with $[VO_3]^-$ Norm. intensity / %		
		250 mM	43.75 mM	8.75 mM	250 mM	43.75 mM	8.75 mM
$[MoO_3]^-$	145				29.77		
$[Mo_2O_7]^{2-}$	151	8.68		3.63		6.85	6.27
$[HMoO_4]^-$	162		9.67	2.84	40.75	1.52	3.58
$[MoO_5]^-$	179		4.83		45.65		
$[Mo_3O_{10}]^{2-}$	223	9.07	1.70	100		100	100
$[Mo_4O_{13}]^{2-}$	296	57.64	14.78	10.00		7.06	3.51
$[HMo_2O_7]^-$	302	79.02	100	11.30	12.47	4.98	7.99
$[Mo_5O_{16}]^{2-}$	367		6.55	3.35		1.46	1.41
$[Mo_6O_{19}]^{2-}$	440	12.56	1.77	0.54			0.69
$[HMo_3O_{10}]^-$	448		3.84	0.78	2.26		
$[Mo_7O_{22}]^{2-}$	512		4.85	1.46			1.16
$[Mo_8O_{25}]^{2-}$	583	12.82	7.77	0.75			0.50
$[HMo_4O_{13}]^-$	592	14.12	5.84	0.75	1.12		0.37
$[H_2VO_4]^-$	116	5.31	3.65		3.72		
$[V_4O_{11}]^{2-}$	189						0.65
$[V_3O_8]^-$	280	19.69				3.47	2.38
$[HV_4O_{11}]^-$	380	100					

Tab. 5.3 continued.

species	m/z	MoV sol. with $[VO]^{2+}$ Norm. intensity / %			MoV sol. with $[VO_3]^-$ Norm. intensity / %		
		250 mM	43.75 mM	8.75 mM	250 mM	43.75 mM	8.75 mM
$[MoVO_6]^-$	243	6.09		2.25	100	9.44	11.66
$[MoV_4O_{14}]^{2-}$	263				10.64	1.12	0.61
$[Mo_3V_4O_{17}]^{2-}$	315			0.14			
$[HMoV_2O_9]^-$	343	7.77		0.17			0.80
$[MoV_7O_{16}]^{2-}$	354	23.58					
$[Mo_2VO_9]^-$	386		40.45	23.01	56.00	27.52	
$[MoV_3O_{11}]^-$	423				1.74		
$[HMo_2V_2O_{12}]^-$	486				0.79		
$[MoV_4O_{13}]^-$	506	12.05					
$[Mo_2V_9O_{24}]^{2-}$	516	56.48					
$[Mo_3VO_{12}]^-$	532		79.85	15.29	19.36	7.82	13.15
$[Mo_3V_7O_{28}]^{2-}$	542	12.69		0.66			
$[Mo_3V_9O_{30}]^{2-}$	614			0.29			0.57
$[Mo_4VO_{15}]^-$	675	4.14			3.30		
$[HMo_4V_2O_{18}]^-$	775	10.10		0.29	0.57	0.42	0.90
$[H_2Mo_5VO_{19}]^-$	836	9.58	3.45	4.32	3.54	3.31	3.39

Despite the evident presence in solution, no Keplerate structures have been found in the mass spectra. These mixed and other Keplerates were detected in the mass spectrometer before, but the conditions applied differ drastically from the ones in this work.[172] Robbins et al. have synthesised isomolybdate and mixed MoV Keplerate clusters with either organic ligands or organic counter ions, and then dissolved them in acetonitrile. This results in the same effect as with the previously examined isopolyoxomolybdates: The condensed and highly charged structure is stabilised by the ligands and counter ions and is hence transferred into the mass spectrometer intact. In aqueous solution with only ammonia as possible counter ion, no stabilisation occurs.

As can be seen from the presented data, there are different isopolymolybdate and –vanadate species present in the solutions as well as a multitude of mixed MoV oxoanions with different Mo/V ratios. Adding up all concentrations of one type of oxoanion and plotting these against the metal concentration

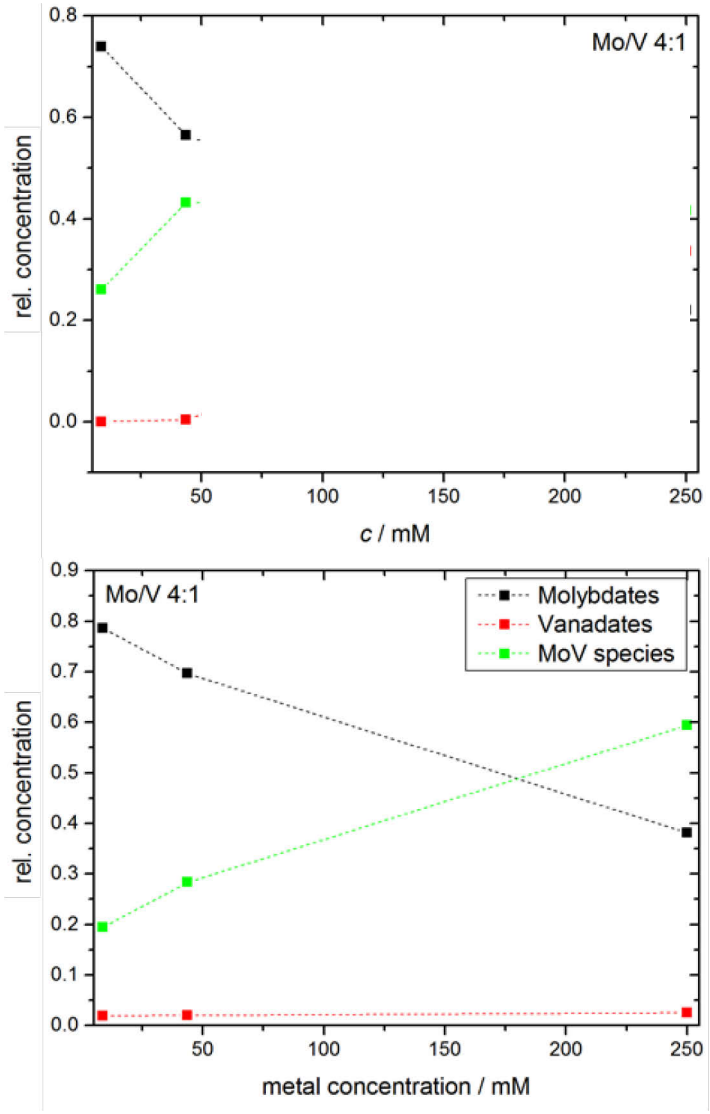

Fig. 5.4: Relative concentrations of molybdate, vanadate, and molybdovanadate species depending on the total metal concentration in solution. Vanadyl containing solutions top, metavanadate containing bottom.

of the respective solution can give information about the presence of species in solution, since for example highly nuclear iso-POM species are very unlikely to fragment from mixed MoV species. These plots are shown in Fig. 5.4.

In the case of vanadyl containing solutions, the relative concentration of vanadates is around 0 %, indicating that all vanadium atoms are incorporated into molybdovanadate species. In turn, their concentration increases with the metal concentration of the solution, whereas the relative concentration of molybdates decreases strongly. The results of the 250 mM sample are muted in the figure, since needle clogging appeared and hence these results do not depict reality.

Solutions with metavanadate demonstrate similar tendencies, but in this case even at the highest metal concentrations the vanadate concentration stays close to 0 %. Instead, the mixed species clearly dominate the spectrum and the presence of molybdate species decreases.

The relative concentrations for the single isopolymolybdates, isopolyvanadates, and molybdovanadates in vanadyl containing solutions are shown in Fig. 5.5 and 5.6. In the case of molybdates, small species with four or less molybdenum atoms tend to be present. This is reasonable since the Mo concentration decreases and therefore smaller clusters are preferred. For vanadates it is noteworthy, that at the highest metal concentration of 250 mM free vanadium sulphate agglomerates form either in solution or during the ionisation process.

In the case of 250 mM metal concentration, the molybdate concentration continuously decreases with increasing metal concentration, while the free vanadate (or vanadyl sulphate) concentration increases, lead to the assumption that the molybdovanadates become richer in molybdenum content. In general, the MoV species are expected to exhibit higher molybdenum content, because the Keplerate $\{Mo_{72}V_{30}\}$ is expected to be present in solution, and it possesses a Mo/V ratio of 2.4. However, since the relative concentration of free vanadium and the content of vanadium in the mixed MoV species increases, there is molybdenum missing from the equation. The reason for this is most likely the extensive clogging of the needle during ionisation for this sample solution. Due to the very high metal concentration and presence of macromolecular species, a solid has formed at the tip of the needle which might not only have inhibited the stabilisation of the ion spray, but also contained the missing molybdenum concentration. Hence, no conclusion can be drawn from the mass spectra of the 250 mM MoV solution.

For lower MoV concentrations, the distribution of isopolyoxometalate species and mixed molybdovanadates in the mass spectra agree well with the speciation shown in the Raman spectra: The concentration of mixed species increases with the total metal concentration while simultaneously the presence of molybdates decreases. This is reflected in the Raman spectra with the increase of the Keplerate signal with increasing concentration. Thus, tentative conclusions can be drawn from the mass spectra if no needle clogging takes place.

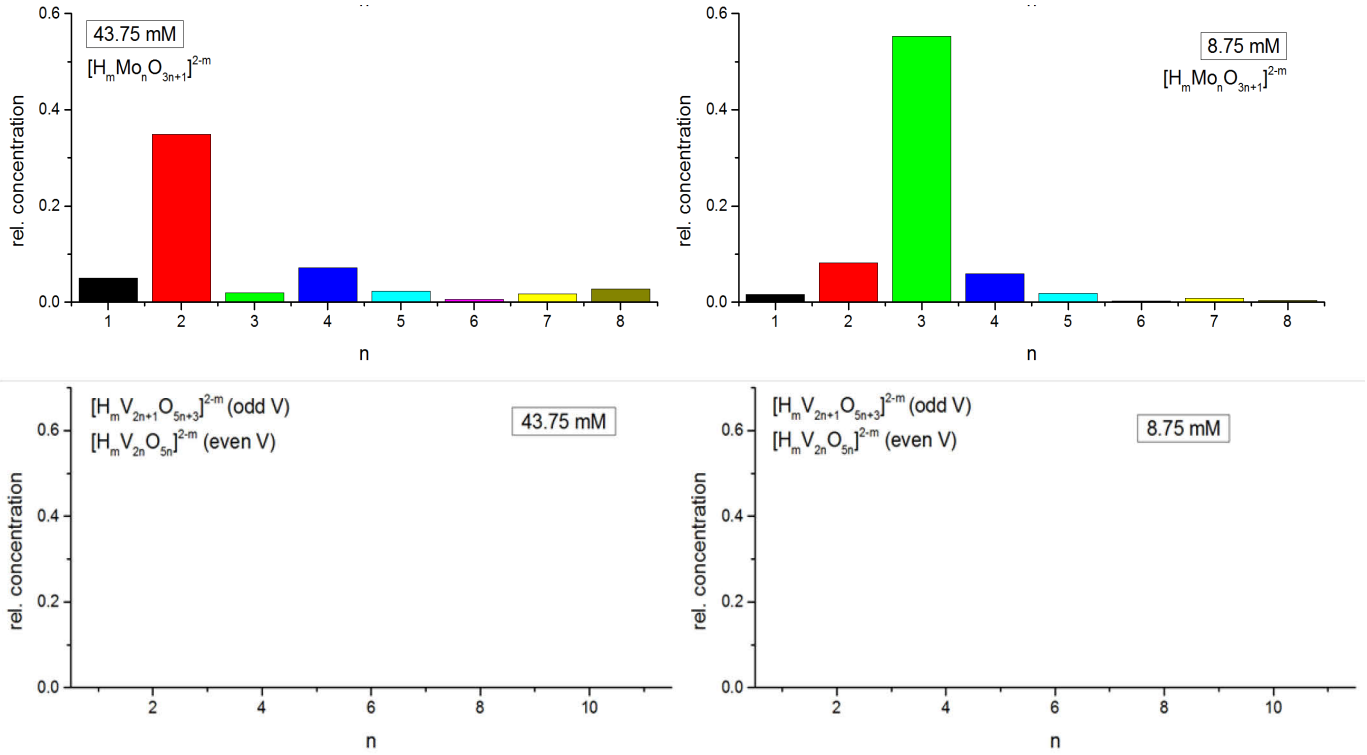

Fig. 5.5: Relative concentrations of isopolymolybdate and isopolyvanadate species in mass spectra of mixed MoV solutions containing vanadyl as V source.

The iso-POM species and molybdovanadate species of the solutions with metavanadate are shown in Fig. 5.7 and 5.8 below. In the case of these solutions, no needle-blocking has been observed for any concentration. Molybdate speciation changes from mostly trimolybdate $[Mo_3O_{10}]^{2-}$ at the two lowest concentrations to being dominated by monomolybdates at the highest metal concentration in solution. This is a good indication that most of the molybdenum is included in the mixed species. Also the very low content of free vanadates tends to form smaller species with increasing total metal concentration, even though there is an outlier in form of heptavanadate for the highest metal concentration of 250 mM. Hence, almost all vanadium should be incorporated in the mixed species as well.

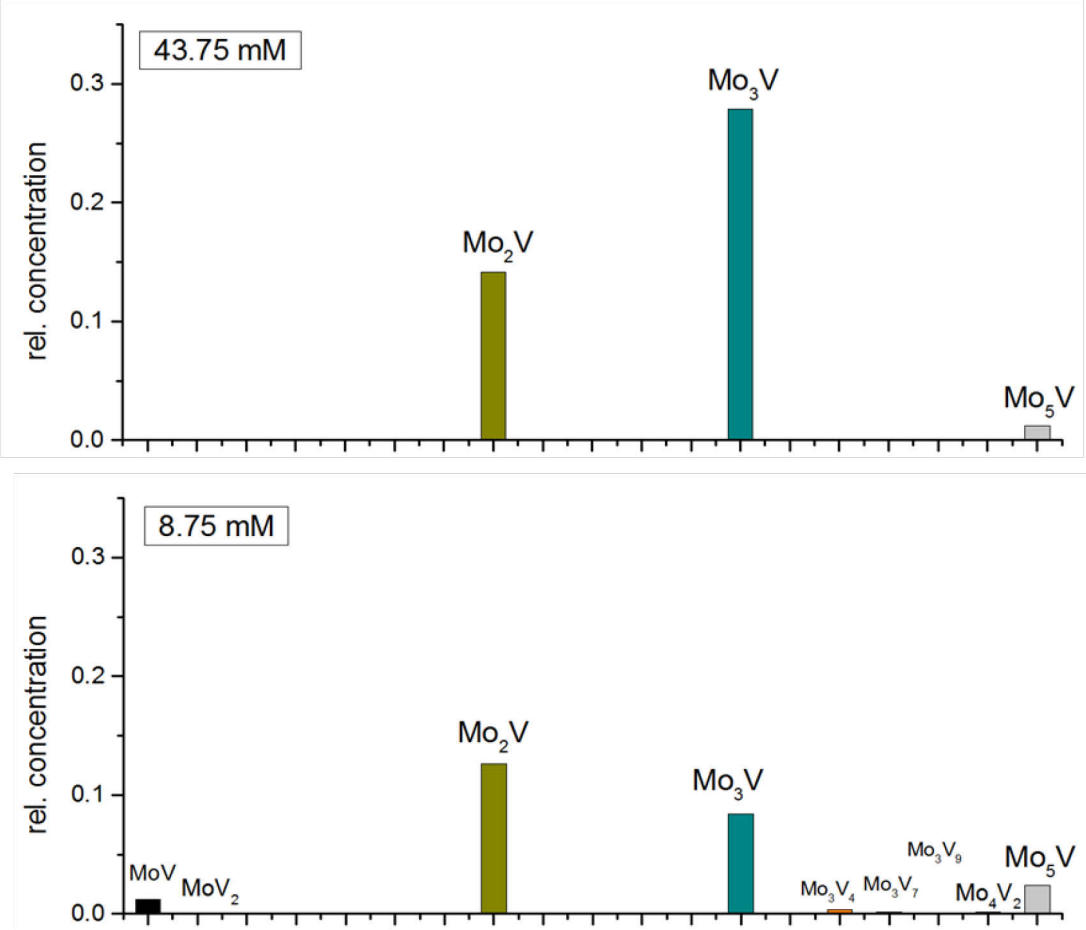

Fig. 5.6: Relative concentrations of mixed MoV species in mass spectra of mixed MoV solutions containing vanadyl as V source.

As is shown in Fig. 5.8, this is the case. At a concentration of 8.75 mM there are many species with high vanadium content present alongside others with more molybdenum. Increasing the concentration to 43.75 mM leads to a decrease of these vanadium-rich species, while the Mo-rich $[Mo_2VO_9]^-$ arises. Finally at 250 mM, there is a plethora of different MoV species present, whereas the majority of them is richer in molybdenum than in vanadium.

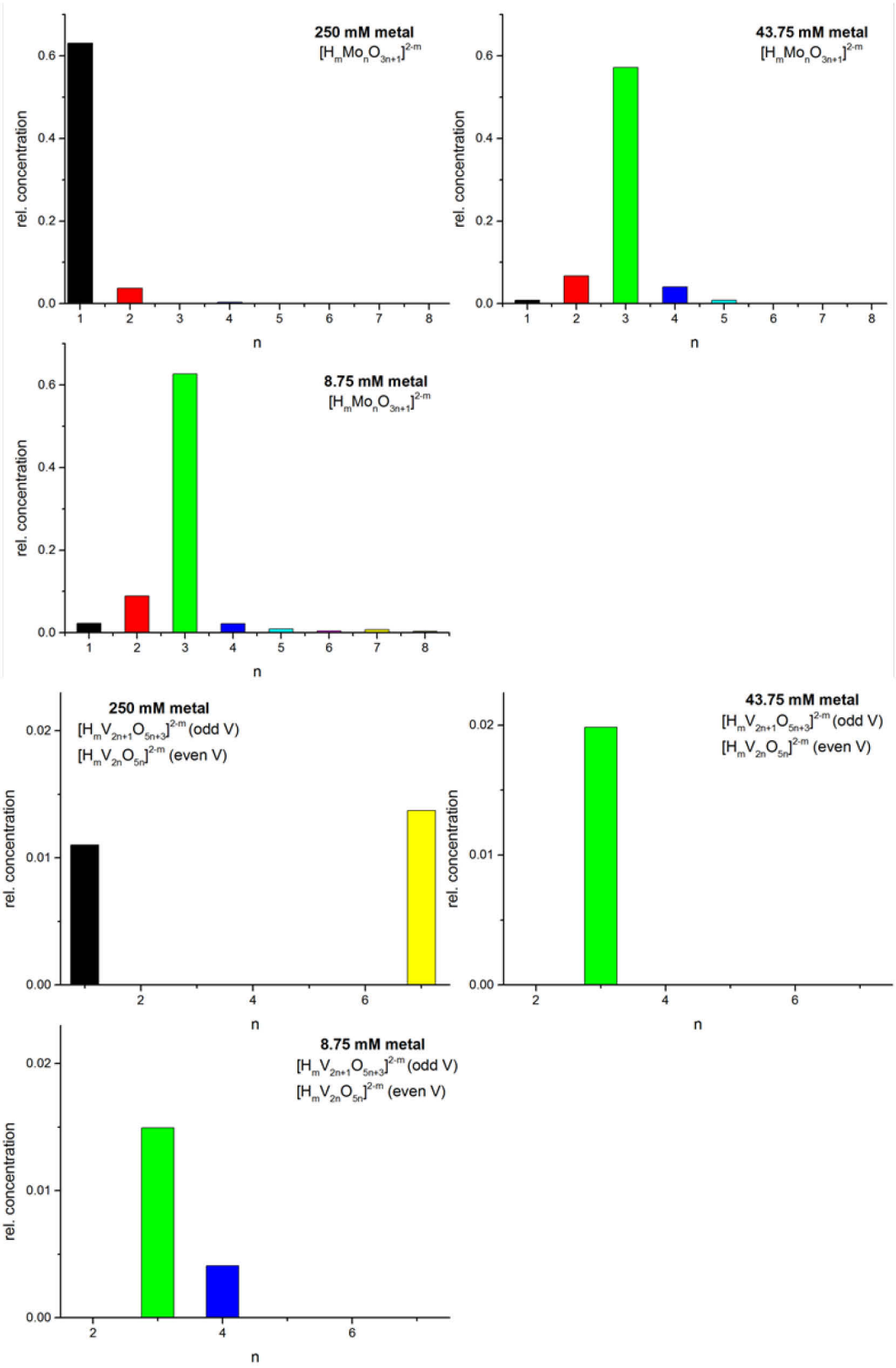

Fig. 5.7: Relative concentrations of isopolymolybdate and isopolyvanadate species in mass spectra of mixed MoV solutions containing metavanadate as V source.

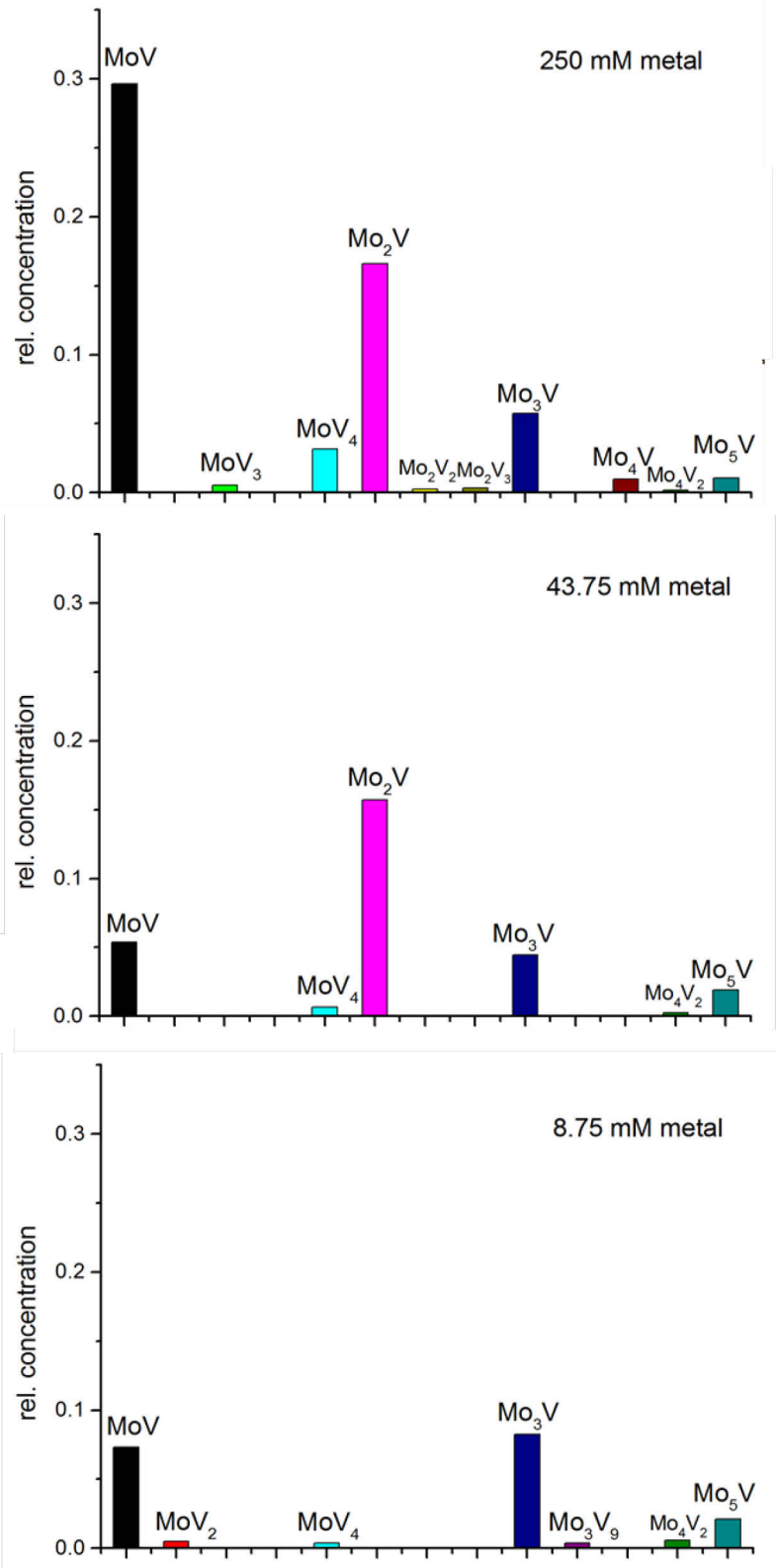

Fig. 5.8: Relative concentrations of mixed MoV species in mass spectra of mixed MoV solutions containing metavanadate as V source.

When taking a look at the Raman spectra of these samples, there are no new bands present in solution which cannot be attributed to known isopolyoxometalate species. Still, it is possible that these signals belong to substituted species. For example, β-$[Mo_7VO_{26}]^{5-}$ has been found in solution by NMR spectroscopy[114] and indications for α-$[Mo_7VO_{26}]^{4-}$, and α- as well as β-$[H_2Mo_6V_2O_{26}]^{5-}$ have been discovered[115]. It is likely, that the signals similar to octamolybdate can be attributed to this kind of mixed species.

With as many different species present in the mass spectra as for these solutions, it is difficult to draw definite conclusions about the species in solution from the ones in the gas-phase. However, if only taking the kind of species (molybdate, vanadate, molybdovanadate) into account, a correlation and agreement between the different techniques can be observed.

5.3 Conclusion

Using vanadyl or metavanadate containing precursors leads to a difference in speciation in aqueous mixed MoV solutions. Raman spectra of vanadyl containing solutions indicate the presence of Keplerate structure {Mo72V30} for all three concentrations, whereas the spectra of metavanadate containing solutions only show signals for isopolyoxometalate species like $[Mo_8O_{26}]^{4-}$. UV-vis spectra support these indications. Hence, mixed Keplerate species are only formed when $[V{=}O]^{2+}$ is directly available in solution as linker. Metavanadate is not transformed to fit in the structure.

Transferring the species into gas-phase via mass spectrometry results in a multitude of different species in all cases, especially molybdates and molybdovanadates are present in various forms. Needle-clogging is an issue at the highest concentration and does not allow conclusions for the solution with synthesis conditions (250 mM total metal concentration, $[VO]^{2+}$) from the mass spectral data. Vanadium is almost completely incorporated in the mixed MoV species in most cases, and these mixed species tend to become molybdenum-richer with increasing total metal concentration.

Mixed MoV species are also found in the solutions with metavanadate, as the found Raman signals might belong to substituted octamolybdate species. However, no Keplerates are formed in these solutions. Still, mass spectral analysis shows a variety of molybdovanadates species in which almost all vanadium is incorporated.

6. Synthesis of MoV based oxides and their catalytic properties

M1 structured mixed metal oxides have been of interest for the catalytic oxidative dehydrogenation of light alkanes for over two decades. Two of the most prominent examples for these materials are MoVTeNb and MoV oxide. Due to its complexity, the M1 structure reacts sensitively to changes in synthesis parameters, which can lead e.g. to four different crystal structures like in the case of $MoVO_x$ or to no formation of the M1 phase at all. Also, the synthesis parameters can influence the concentration of vanadium in the mixed oxide which subsequently affects the catalytic activity as has been described in chapter 1.1.5.

In the previous chapters, investigations of isopolyoxometalates and molybdovanadates in aqueous solution and in the gas-phase have shown the dependence of the speciation on the pH value and metal concentration. Hence, this chapter deals for one with the effect for dilution on the synthesis of $MoVO_x$ and its structure, and for two with the effects of small amounts of a third transition metal to substitute vanadium in the M1 structure. Lastly, the catalytic properties in the ODH of ethane of the substituted $(MoV)O_x$ compounds are investigated.

6.1 Diluted synthesis

MoV oxides have been synthesized via hydrothermal synthesis in an autoclave setup at different extents of dilution. The standard M1 $MoVO_x$ synthesis is carried out with a Mo/V ratio of 4:1 and a total metal concentration of 250 mM (200 mM Mo, 50 mM V) in the precursor solution whose pH value was 3.7 when the two metalate solutions were mixed. Fig. 6.1 shows the Raman spectra of the MoV precursor solution during the heating process. As shown in the previous chapter in Fig. 5.1, the spectra are dominated by a signal around 871-876 cm^{-1} belonging to the Keplerate structure $\{Mo_{72}V_{30}\}$. At room temperature, signals for octamolybdate species and vanadyl vibrations can be found at 961 cm^{-1} and 993 cm^{-1}, respectively.

During heating up, the Keplerate signal at 876 cm^{-1} almost vanishes between 155 and 165 °C, indicating a lack of stability at the common synthesis temperature of 200 °C. Hence, Keplerate $\{Mo_{72}V_{30}\}$ cannot be the direct precursor species to M1 in the case of MoV oxide. This has been shown as well in the case of quaternary M1 $MoVTeNbO_x$ as the Keplerate structure breaks down at low temperatures once telluric acid is added[173]. Still, Keplerate $\{Mo_{72}V_{30}\}$ contains the structural motif $\{(Mo)Mo_5\}$ which is an essential component of the final M1 structure.

After 17 hours at 200 °C, 78.84 g of a black solid (internal sample number 25193, denoted MoV-Org) were obtained, corresponding to a yield of 94.25 %. Raman spectra have not been recorded during

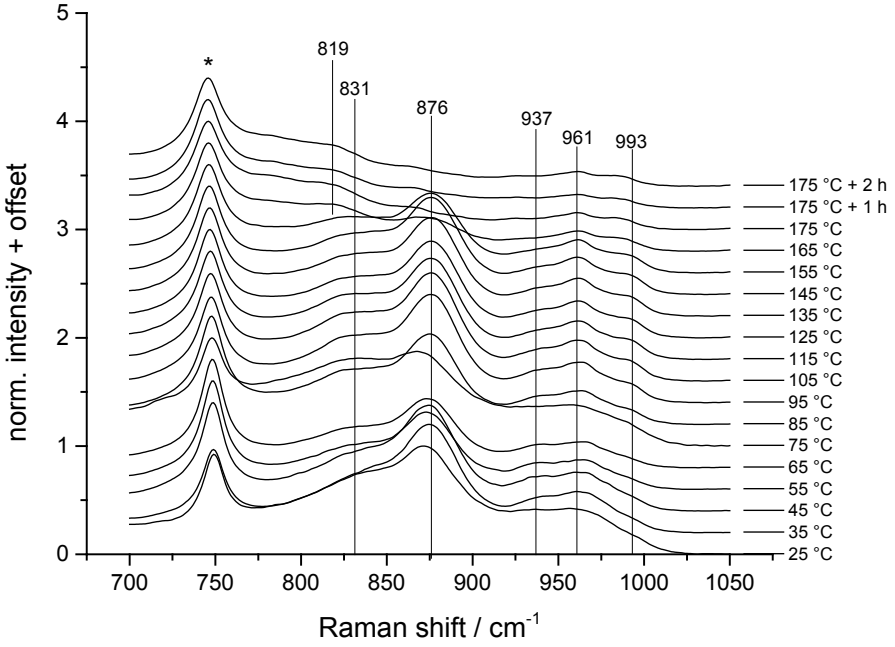

Fig. 6.1: Raman spectra of hydrothermally heated 4:1 MoV solution (200 mM Mo, 50 mM V). * denote the band of the Raman probe.

synthesis due to the instability of the probe to acidic medium above 175 °C. The Raman spectra of the cooled down synthesis solution, the mother liquor and the corresponding freshly obtained solid suspended again in dist. water are shown in Fig. 6.2 left.

Taking a look at these spectra after hydrothermal synthesis, it is obvious that the same signals characteristic for the M1 structure at 841, 871, and 918 cm^{-1}[117] can be found in the spectra of the synthesis solution and the obtained solid. The signals in the mother liquor belong to remaining octamolybdate (956 cm^{-1}) and vanadyl (980 cm^{-1}) species.

To compare the synthesis with the speciation detected in solution and in the gas-phase at 25 °C, the concentration of metals was reduced by a factor of 5.7 to yield a total metal concentration of 43.75 mM for the first diluted synthesis (int. sample number 26672, denoted MoV-Dil1). The Raman spectra recorded after synthesis are shown in Fig. 6.2 right.

For MoV-Dil1 the intensity of the bands in the mother liquor decreases compared to the ones of the

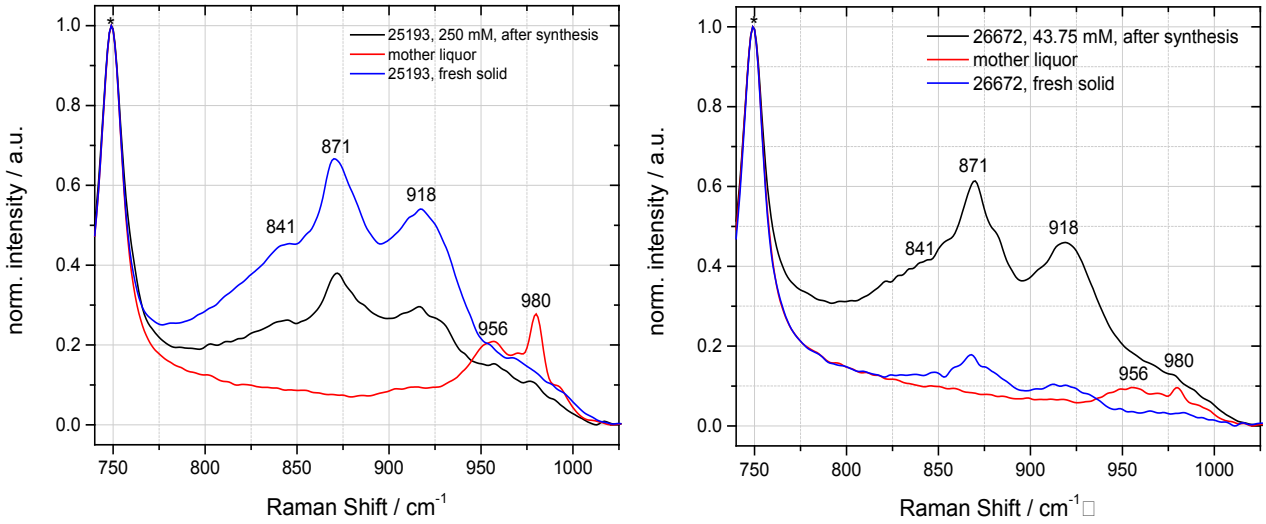

Fig. 6.2: Raman spectra of the product suspension right after synthesis (black lines), and the mother liquor (red lines) and suspended fresh solid (blue lines).

synthesis solution. This is probably originates from the fact that there are less free metalate ions present due to the reduced concentration have been used up in the formation of $MoVO_x$. This grade of dilution resulted in 10.24 g of a black solid, equivalent to a yield of only 69.8 %.

Diluting the precursor solution further to 12.5 mM did not lead to any solid obtainable from the glass frit after the washing with water right after synthesis. Concentrations of 8.75 mM (MoV-Dil2, 0.3 % yield) and 0.125 mM produced 8 mg of solid and less, respectively.

XRD measurements of all obtained samples are depicted in Fig. 6.3. MoV-Org (red line) consists of phase-pure M1 structure, albeit not completely crystalline. For MoV-Dil1 the measurements revealed that about 10 % of the sample is made up of hexagonal MoO_3-type structure, in which molybdenum is substituted by vanadium to a certain extent as indicated by the shift of the reflexes away from pure MoO_3. The remaining 90 % belong to poorly crystallized M1. This is shown as blue line in Fig. 6.3, the orange numbers labelling the reflexes belonging to the partially substituted hexagonal MoO_3. This structure (ICSD 75417) is similar to that of M1 in the regard that it features large channels in the *a*-*b*-

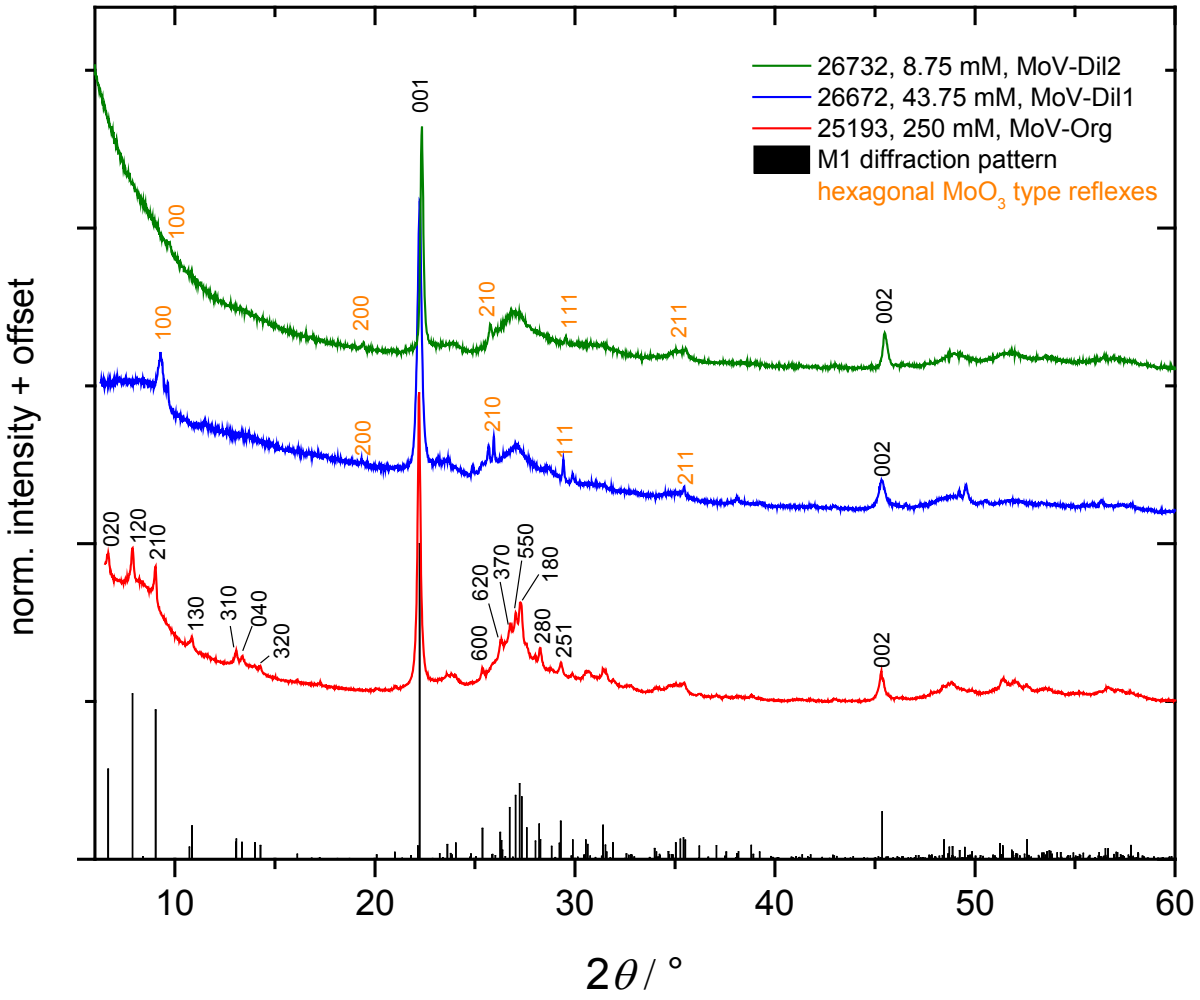

Fig. 6.3: X-ray diffractograms of MoV-Org (25193, red line), MoV-Dil1 (26672, blue line), and MoV-Dil2 (26732, green line). Reflexes of M1 structure in black, additional hexagonal MoO_3-type reflexes in orange.

plane and layer stacking in the direction of the *c*-axis. It has previously been detected under hydrothermal synthesis condition, as well[97].

A diffractogram of MoV-Dil2 was obtained and is shown in Fig. 6.3 as well as a green line. As in the case of MoV-Dil1, there are hexagonal MoO_3-type structures present. Due to the highly amorphous nature of the sample, it is difficult to ascertain the exact percentage of the occurring phases, but it can be roughly estimated that of the crystalline components present the M1 phase makes up 97 % of the sample, while the remaining 3 % are composed of the partially vanadium substituted hexagonal MoO_3- type structure.

Chemical analysis of the solids and mother liquors was performed with x-ray fluorescence. However, for MoV-Dil2 the obtained solid was not enough for fluorescence measurements. Instead, EDX measurements have been performed to have comparable data for all samples. The results of all five samples are listed in Tab. 6.1 and 6.2 below.

Tab. 6.1: Elemental composition based on XRF measurements and yield of obtained solid and their corresponding mother liquors after hydrothermal synthesis with diluted MoV precursor solution.

Sample #	Total metal concentration / mM	Mo / at%	V / at%	Yield / %
25193 / MoV-Org	250	69.45	30.55	94.25 (78.84 g)
26672 / MoV-Dil1	43.75	63.89	36.11	69.8 (10.24 g)
26562	12.5	-	-	-
26732 / MoV-Dil2	8.75	-	-	0.3 (0.008 g)
26578	0.125	-	-	< 0.5

Tab. 6.2: Elemental composition of synthesised MoV oxides based on EDX measurements.

Sample #	Mo / at%	V /at%	Mo/V
25193 / MoV-Org	72.78	27.22	2.67
26672 / MoV-Dil1	69.12	30.88	2.24
26732 / MoV-Dil2	68.84	31.16	2.21

Taking into account the mass spectral and spectroscopic analysis of the precursor solutions of these three samples, it might be possible to obtain an answer as to why the yield decreases with the metal concentration in solution. One possibility is the decrease of Keplerate $\{Mo_{72}V_{30}\}$ concentration. However, it has been shown that this structure is not directly the precursor in M1 synthesis as shown above in Fig. 6.2.

Another way of argumentation can be that there is a high number of free vanadyl species present in the precursor solution of MoV-Org according to mass spectrometric measurements (Fig. 5.4). Vanadyl acts

as a linker at elevated temperatures and organises the structural reorganisation from the {(Mo)Mo_5} motif to M1 structure. Hence, it is of great importance for the formation of solid M1 $MoVO_x$ that there is a certain concentration of available vanadyl present in solution. At lower total metal concentrations in solution, all present vanadium is used as building blocks for the mixed MoV species and hence these free vanadate species disappear. Thus, the formation of the M1 structure is hampered during synthesis and less solid is obtained.

As can be seen from Tab. 6.2, the ratio of molybdenum to vanadium decreases with the dilution of the synthesis. Hence, the obtained solid becomes vanadium-richer, the further the total metal concentration of the precursor solution is decreased. This agrees with the XRF and EDX data in Tab. 6.1 and 6.2 that show the obtained solid of the respecitve syntheses to get vanadium-richer with decreasing total metal concentration. In addition, the results of the gas-phase studies described in chapter 5.2 are hinting at this development. Herein, the mixed MoV species detected in the mass spectrometer became vanadium-richer with decreasing metal concentration as well. Still, the mass spectral data cannot be used to predict the outcome after hydrothermal synthesis, since the spectra were obtained at room temperature and the speciation of polyoxometalates changes under hydrothermal conditions[97]. Liquid-phase analysis like shown for the Raman analysis of the precursor solutions (chapter 5.1) or of the suspended solid right after synthesis as shown in Fig. 6.3 below do not allow drawing any kind of conclusion regarding the elemental composition.

Lastly, every material possesses a certain value of solubility. Under the same synthesis conditions, the same amount of ionic components will remain in solution if the concentration of the ions is larger than the solubility value. In the case of $MoVO_x$ it is thus possible, that the solubility at 25 °C is quite low, but gains influence in relation to the total metal concentration. This means, that there might always be the same amount of metalates dissolved in solution, whereas the actual oversaturation needed for crystallisation is drastically lowered with the metal concentration in the precursor solution.

Also, transmission electron microscopy (TEM) was performed for the samples MoV-Org, MoV-Dil1, and MoV-Dil2. The obtained pictures are shown in Fig. 6.4. At first glance, all samples show rod-shaped particles with the size of various micrometers and ragged edges (top row) and no clear distinction can be made. Going to higher magnifications renders the typical layer structure of M1 visible (middle row), whereas amorphous parts are visible as well in the cases of MoV-Dil1 and MoV-Dil2. This observation agrees with the x-ray diffractograms which clearly depict the increasing anisotropic character of the samples obtained via diluted synthesis.

Magnification to the nanometre scale shows the distinct structural characteristics of M1, namely the flower-like {Mo_6} moiety, in the case of MoV-Org, albeit it is highly defective. The same is visible for the diluted samples MoV-Dil1 and MoV-Dil2. However, for the samples obtained under diluted conditions, amorphous appearing zones are visible (bottom row). These can have various origins. In general, either

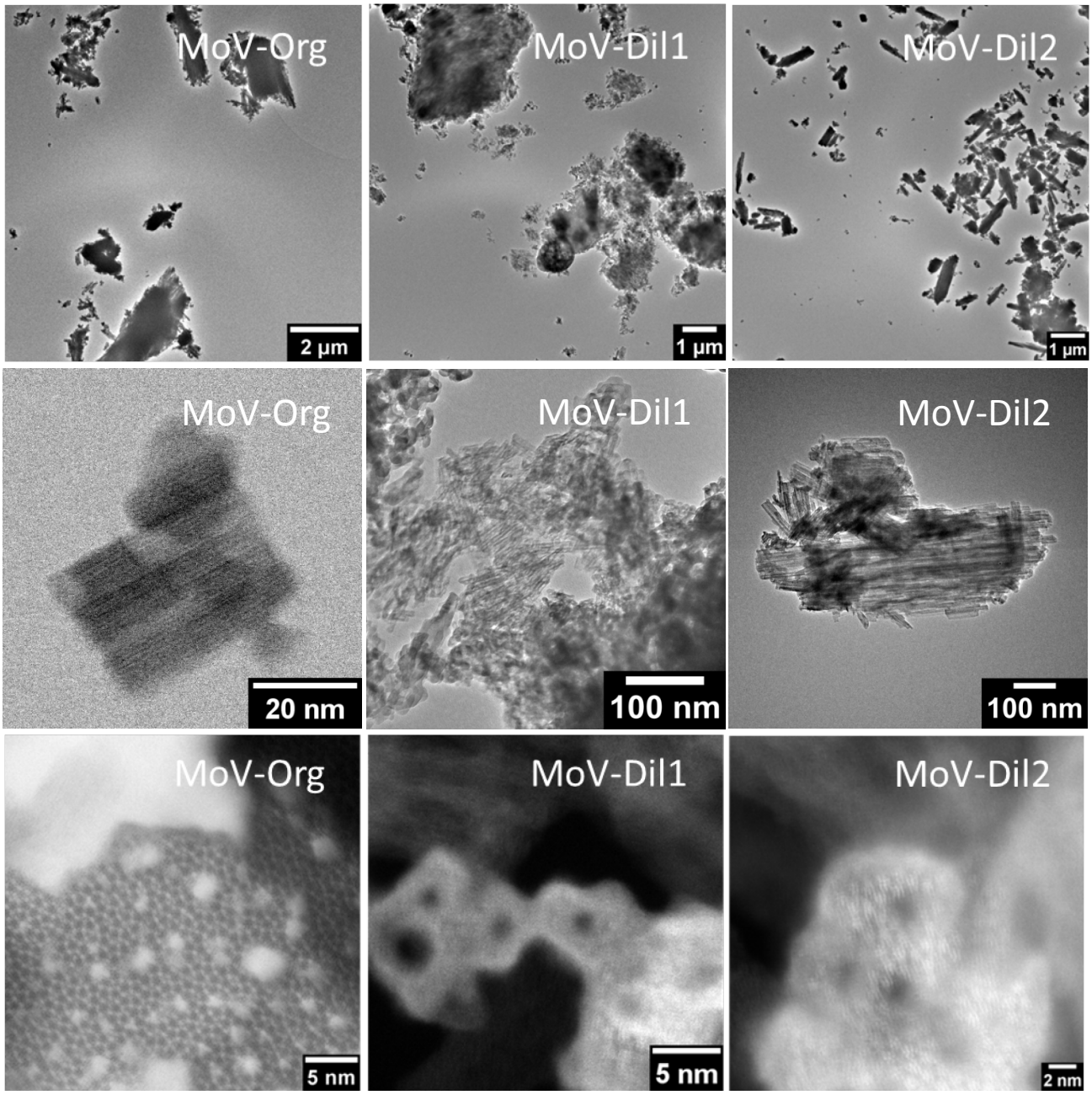

Fig. 6.4: TEM images of MoV-Org (left), MoV-Dil1 (middle), and MoV-Dil2 (right).

layers of the *a*-*b*-plane are out of orientation or focus, which can be caused by steps in the 3D structure,

or it is actual amorphous material. In this case, it might also be hexagonal vanadium substituted MoO_3 which has been detected via XRD measurements (Fig. 6.3). The increase of vanadium concentration in the samples MoV-Dil1 and MoV-Dil2 might coincide with the appearance of these vanadium enriched amorphous phases.

Summarised, this clearly shows, that even at the very low metal concentration of 8.75 mM in the precursor solution the basic M1 structure can be formed. However, this also indicates the precursor species present in the isometalate solutions – which are crucially dependend on the concentration as has been shown in chapters 3 and 4 – have no significant influence on the formation of the M1 structure on a molecular level. As long as the molybdenum concentration is high enough, the pentagonal $\{Mo_6\}$ moieties are formed and can be linked via free molybdate or vanadate species.

The defectiveness of the structure in the two dimensional *a*-*b*-plane then depends on the condensation mechanism dictated by the concentration of the remaining Mo or V linker species. Thus, even though the $\{Mo_6\}$ moieties are formed, there are less and smaller seeds for condensation present with decreasing metal concentration, so that even with cooling down of the synthesis solution the oversaturation needed for further condensation is not achieved.

On the other hand, the effect of the concentration on the defects in the *a*-*b*-plane does not effect the three dimensional arrangement. The characteristic layers in direction of the *c*-axis form independet of the structural arragement in the *a*-*b*-plane, as can be seen from Fig. 6.5. Therein the layer structure with

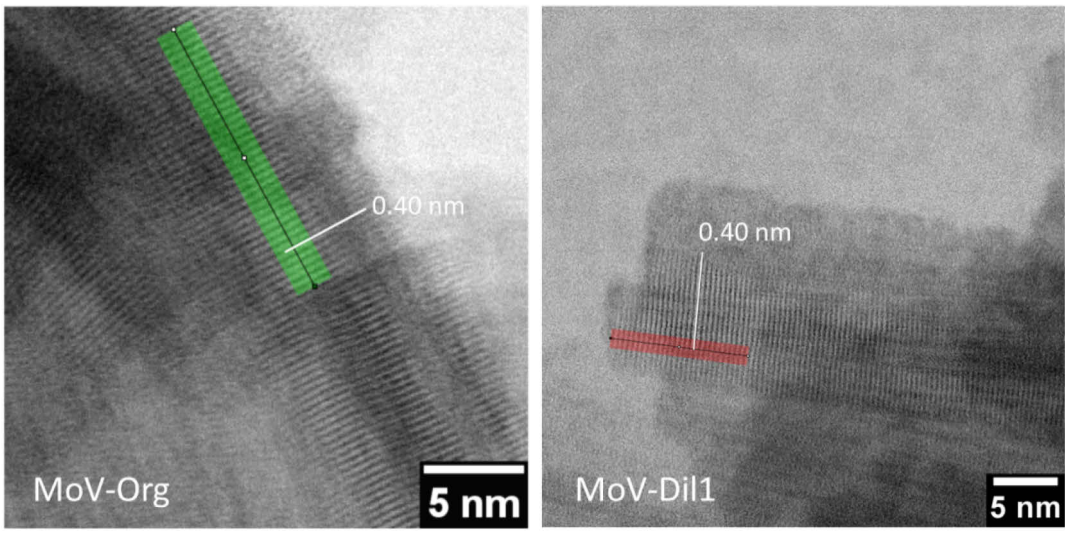

Fig. 6.5: TEM images of MoV-Org (left), and MoV-Dil1 (middle) with the direction of the *c*-axis depicted as coloured bar.

its width of 0.40 nm between layers is clearly visible.

The presence of large defects in the two dimensional structure of MoV-Org hints furthermore at the subsequent rearrangement to a more ordered M1 structure due to activation treatment.

To examine the reversibility of the crystallisation process and further the solubility of $MoVO_x$, the obtained MoV-Org solid was subjected to the same hydrothermal synthesis procedure with the same chemical potential, i.e. 7.70 g of MoV-Org in 260 mL in dist. water and a pH value of 3.7 before heating up and holding the high temperature for 17 hours. To record Raman spectra and thus follow the structural changes during this treatment, the temperature was reduced from 200 °C to 175 °C. These spectra are shown in Fig. 6.6.

As visible in the Raman spectra in the top row of Fig. 6.6, first changes appear at temperatures of 125 °C and more. The M1 band at 842 cm^{-1} shifts to 821 cm^{-1} and the bands at 975 and 990 cm^{-1} appear. The

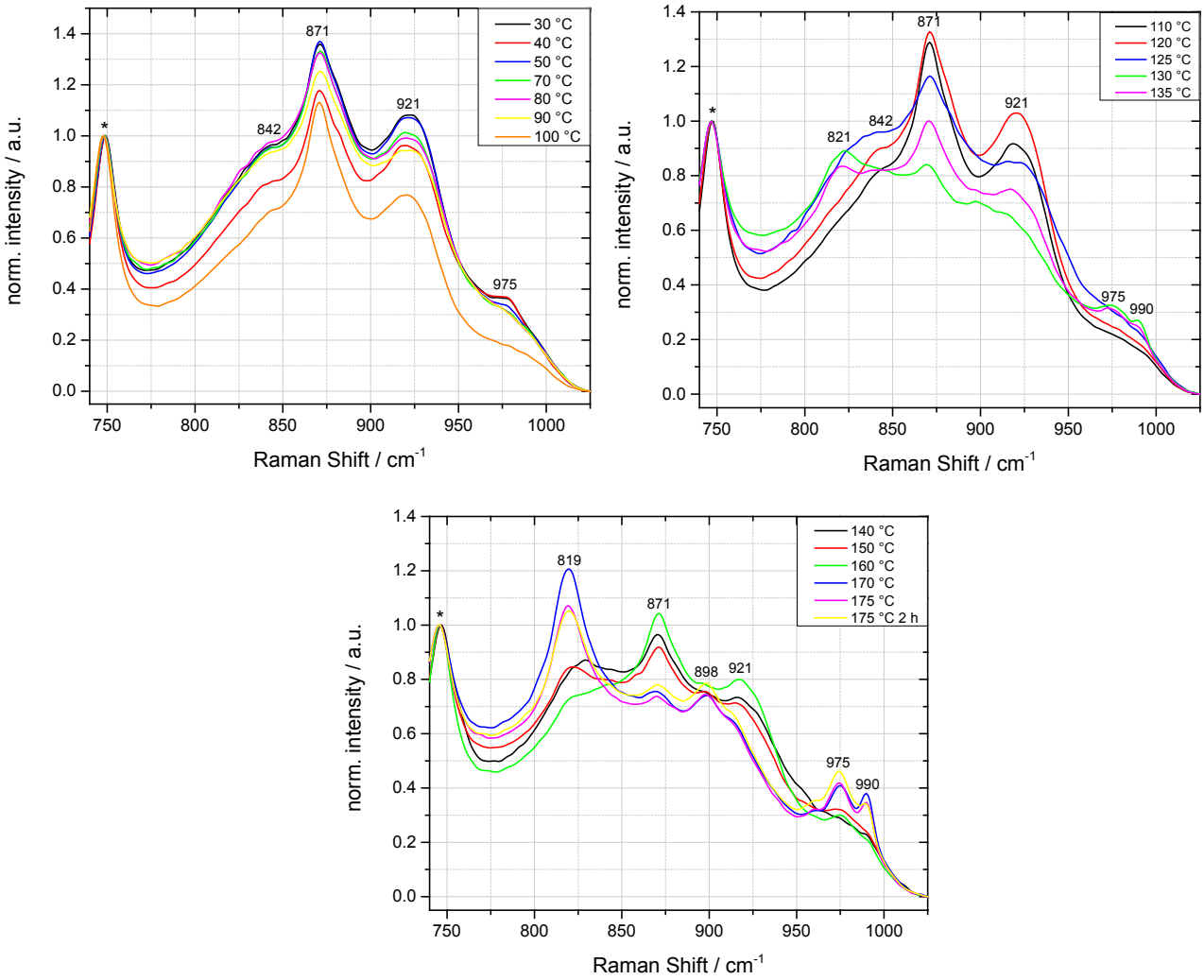

Fig. 6.6: Raman spectra of the suspended and subsequently heated MoV-Org; * indicates the signal of the Raman probe.

latter two belong to the heat-shifted signals of octamolybdate or hexagonal MoO_3 structures species, which have previously been reported to be present under hydrothermal conditions[97], and vanadyl species, respectively. The band at 821 cm^{-1} becomes stronger and shifts slightly to 819 cm^{-1} with increasing temperature (Fig. 6.6 bottom). Simultaneously the band at 921 cm^{-1} decreases slightly and shifts to 898 cm^{-1}, while the signals at 975 and 990 cm^{-1} become very prominent features.

The appearance of the band at 898 cm^{-1} agrees with the presence of structures of the hexagonal MoO_3 type as indicated by the signal at 975 cm^{-1}. Hence, heating the obtained MoV-Org structure again under hydrothermal conditions changes the structure and might even induce decomposition, but after cooling down the solution – as depicted in Fig. 6.7 left – leads again to the same M1 structure as before, rendering the M1 crystallisation process irreversible. However, the mother liquor after hydrothermal treatment of MoV-Org (Fig. 6.4 right) shows slightly different signal intensities compared to the mother liquors of the directly synthesised MoV-Org and MoV-Dil1. For the hydrothermally treated MoV-Org (blue line) shows the vanadyl band at 993 cm^{-1} as being the most intense, indicating that compared to

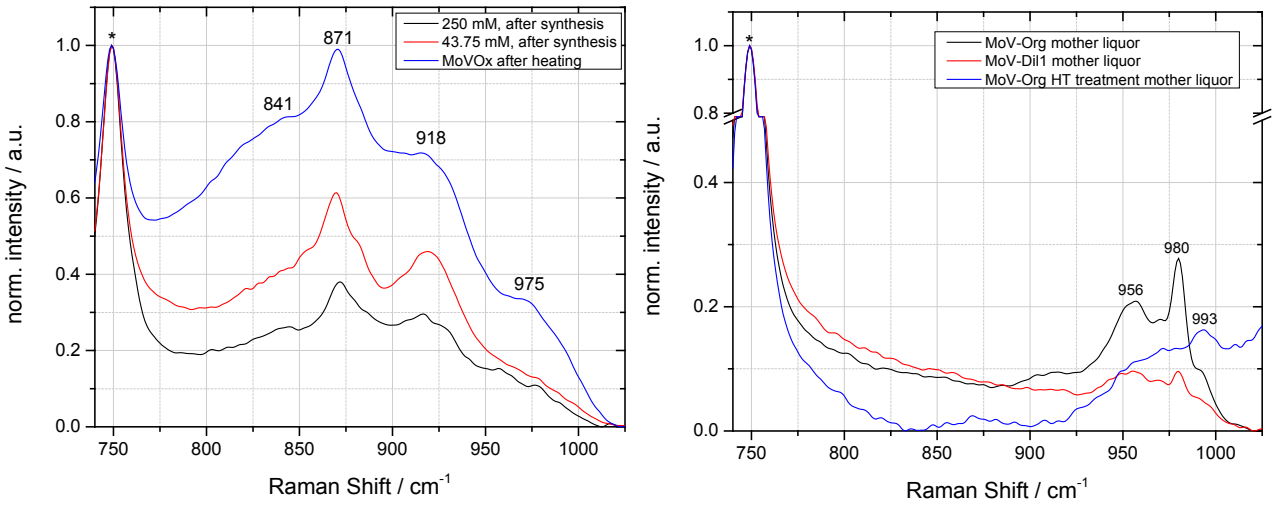

Fig. 6.7: Raman spectra of MoV-Org (black line), MoV-Dil1 (red line) and the suspended and subsequently heated MoV-Org (blue line) right after synthesis/hydrothermal treatment (left) and the corresponding mother liquors (right); * indicates the signal of the Raman probe.

MoV-Org and MoV-Dil1 predominantly vanadium has been washed out of the M1 structure. XRF analysis of the respective mother liquors shows the same value of vanadium concentration in solution after the hydro thermal treatment of MoV-Org and directly after the synthesis if MoV-Org (both 0.2 g/L vanadium), while the molybdenum concentration decreases from 5.4 g/L after synthesis to 1.3 g/L after

HT treatment and thus confirms the assumption. These chemical analysis data of the solid samples and the respective mother liquors is shown in Tab. 6.3.

Tab. 6.3: Content of molybdenum and vanadium in the synthesised/hydrothermally treated MoV oxides and their corresponding mother liquors based on XRF analysis.

Sample #	Total metal concentration / mM	Mo / at%	V / at%	Mo/V
25193 / MoV-Org	250	69.45	30.55	2.27
Corrsp. mother liquor		63.33	4.61	13.7
25193 / MoV-Org after HT	250	68.67	31.33	2.19
Corrsp. mother liquor		70.37	13.78	5.1
26672 / MoV-Dil1	43.75	63.89	36.11	1.77
Corrsp. mother liquor		72.13	4.55	15.8
26732 / MoV-Dil2	8.75	-	-	-
Corrsp. mother liquor		44.05	7.08	6.22

In conclusion, the dilution of the precursor solution has a greater impact on the formation of the M1 structure than the speciation of the polyoxometalates. While the POM speciation is indeed influenced by the concentration, mixing the molybdate and vanadate solution leads to almost identical Raman spectra regardless of the concentration. After synthesis however, it is clearly visible that with decreasing concentration in the precursor solution the number of defects and tendencies to amorphous structures increase in the *a*-*b*-plane, and at the same time the concentration of vanadium in the structure. Still, the three dimensional layer structure forms in any case, while rearrangement to a highly crystalline M1 structure is not obtained just by hydrothermal treatment, but thermal activation is a necessary step for this.

Subjecting the synthesised MoV-Org to the same treatment as during synthesis leads to the same M1 structure after cooling down. However, significant amounts of vanadate species were found in the resulting mother liquor.

6.2 Substitution of vanadium

While vanadium plays a crucial role for the activity of the catalyst in the oxidative dehydrogenation reaction of alkane, it can also hinder the selectivity to the desired product by passivating the surface and/or promoting total combustion by segregating to the catalyst surface via the structures heptagonal channels along the c-axis[77]. Hence, it is of interest to reduce the vanadium content – preferably in the aforementioned channels – while still maintaining the highest activity possible. In the case of mixed MoV oxide, this also means retaining the sensitive M1 structure. One approach to this is to replace a miniscule part of the original vanadium concentration by metals with a different oxidation state but an ionic radius which still fits in the heptagonal channels of the M1 structure.

For this reason, 1 % of the vanadium content in the precursor solution was replaced by various transition metals to then treat it hydrothermally in a microwave setup. The chosen metals and their respective ionic radii are listed in Table 6.4. In all cases, one gram or more of black solid was obtained. The diffractograms of all solid precursors are shown in Fig. 6.8. All solids show the characteristic M1 structure and are phase-pure, whereby the samples with manganese and cobalt are only poorly crystallised along the *a*- and *b*-axis. This could stem from the fact that both manganese and cobalt do not prefer the octahedral coordination due to their possible high-spin state and thus contort the structure, leading to broadening of the reflexes.

Tab. 6.4: Chosen metal ions and their respective ionic radii in octahedral coordination environment.

Metal	Ionic radius / Å
V^{+IV} / V^{+V}	0.58 / 0.54
Ti^{+IV}	0.605
Mn^{+II} (low-spin high-spin)	0.67 / 0.83
Co^{+II} (low-spin high-spin)	0.65 / 0.745
Zn^{+II}	0.74
Te^{+VI}	0.56
Cr^{+II}	0.615
As^{+III}	0.58

Since the aim was to substitute 1 % of the original nominal vanadium content, it is of interest how the concentration of vanadium has changed. Original synthesis with the usual V concentration of 5 mM in the precursor solution leads to a solid with a vanadium content of 30.82 at% among all present metals. Compared to that, the substitutions with all elements but tellurium have led to a reduction of the atomic percentage of vanadium. The molybdenum content has decreased for the synthesis with tellurium as well, as it has done in the case with iron as well. The latter can be attributed to the above average content of iron, which might have displaced molybdenum. All chemical analysis and BET surface measurement results can be found in Tab. 6.5.

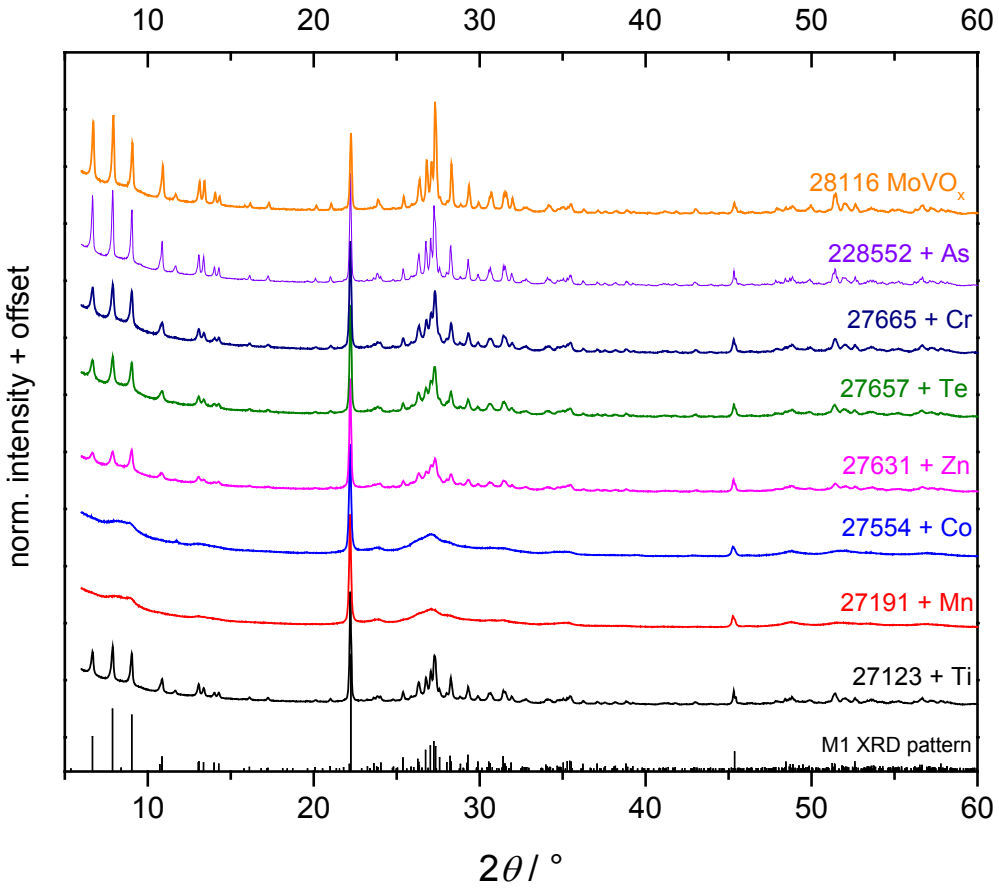

Fig. 6.8: X-ray diffractograms of all catalysts, including reference MoVOx.

Tab. 6.5.: Chemical composition and BET surface area of synthesised MoV oxides.

Sample #	substituent	Mo / at%	V / at%	Subst. / at%	Surface / m²/g	Yield / g
27123	Ti	70.09	29.71	0.20	18.8	2.40
27191	Mn	69.27	30.5	0.23	38.0	1.41
27554	Co	69.29	30,51	0.20	20.2	1.67
27631	Zn	69.95	29.80	0.25	21.2	1.81
27657	Te	68.43	31.35	0.22	21.7	1.50
27665	Cr	69.86	29.84	0.30	19.4	1.60
28552	As	69.00	31.00	**	6.3	1.06
28116	-	69.18	30.82	-	9.5	0.94

** arsenic oxide is volatile, therefore no detection in XRF

The surface area of unsubstituted MoVOx is below 10 m²/g with 9.5 m²/g. All substituted samples – except for the one with copper – surpass this value by mostly more than 100 %. The manganese containing sample possesses even more than four times the surface area of the unsubstituted MoVOx with 38 m²/g. While a high surface area is generally desired due to the possibility of higher catalytic activity, the strong increase just by adding a small amount of another metal rather hints to more amorphous material present, which cannot be detected by XRD measurements.

Still, XRD and scanning electron microscopy (SEM) studies have not shown any hint at second phases. However, this might stem from the very low concentration of the substituent metals in the overall solid which exceeds the detection limit of the experimental techniques.

SEM images of the different solid precursors are shown in Fig. 6.9. All samples show the needle-like morphology of the M1 structure, whose crystallisation along the c-axis results in this kind of crystal shape. From the images it is also visible that for example the solids with manganese and cobalt possess a less pronounced needle structure and instead more amorphous crystallites. This agrees well with the poorer crystallisation which is visible in the respective diffractograms (Fig. 6.8).

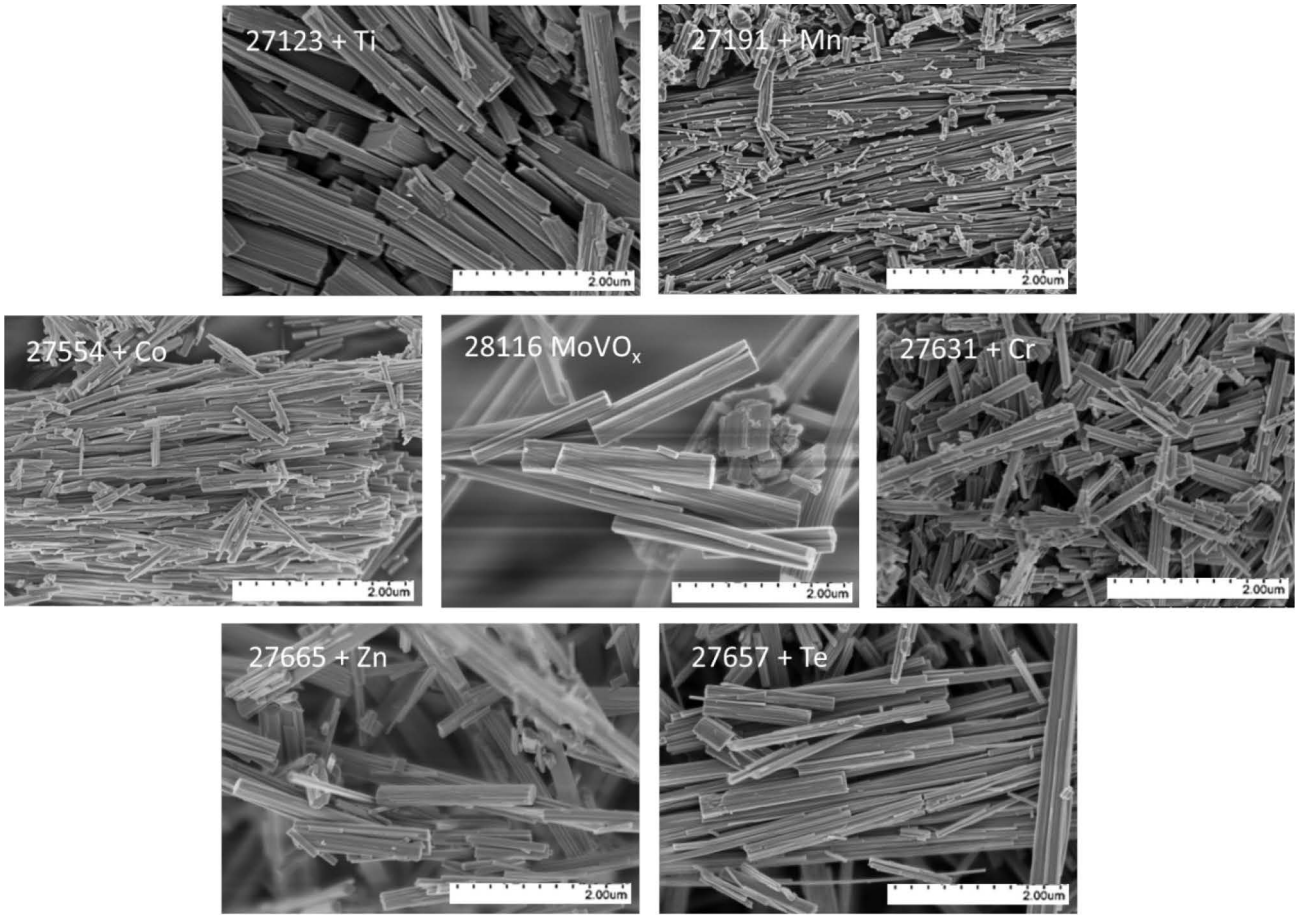

Fig. 6.9: Scanning electron microscopy images of (un)substituted MoV oxides.

6.3 Oxidative dehydrogenation of ethane

The oxidative dehydrogenation of ethane has been tested for two different gas feed compositions: ethane/O_2/N_2 10:5:85 and 10:10:80, the latter being more oxidising. The ethane conversion in percent and the conversion rate in mol_{ethane} per gram catalyst and second for both feeds are shown in Fig. 6.10 below.

For the first feed, the graphs are labelled A and B. Looking at the conversion in percent, it is visible that all substituted catalysts perform better than the original one without a third metal incorporated. Only at the last temperature of 290 °C the unsubstituted sample shows an ethane conversion higher than the solids with additional titanium, tellurium and arsenic. The zinc substituted sample exhibits the highest conversion of 12 % at 290 °C, whereas MoVMn and MoVCo show the highest conversion values

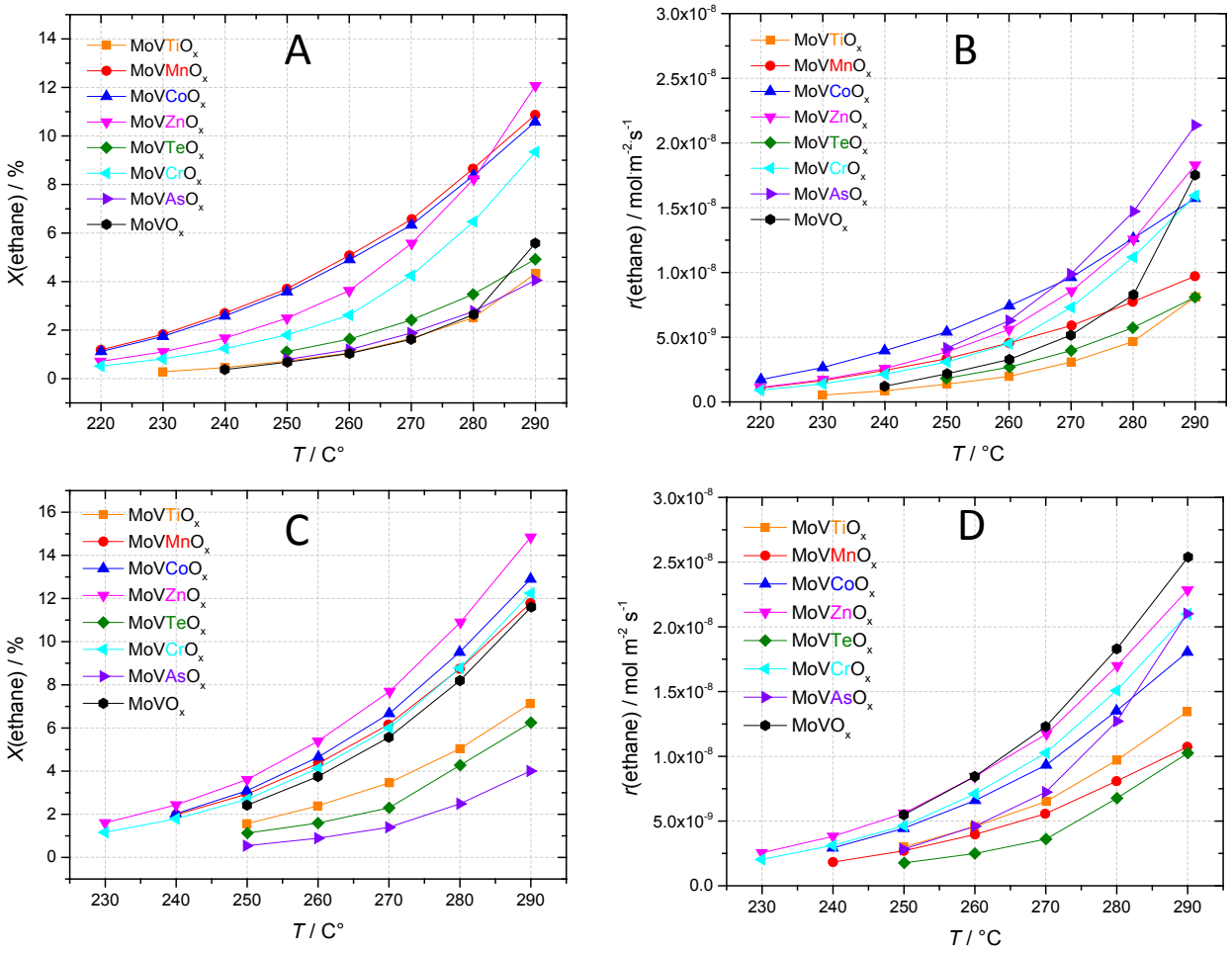

Fig. 6.10: Ethane conversion percent and conversion rate in mol(ethane)/(m^2_{cat}·s) for the gas feed composition of ethane/oxygen/nitrogen 10:5:85 inn A and B, respectively. Conversion and conversion rate for the gas feed composition 10:10:80 in C and D, respectively.

throughout the rest of the temperature range.

Calculating the conversion depending on the surface area of the respective catalysts leads to the conversion rate depicted in Fig. 6.5 B. This results in major changes in the ranking. Over the temperature range from 220 °C to 280 °C the order changes to As > Zn > Co > Cr > $MoVO_x$ > Mn > Te > Ti. These drastic changes originate from the large surface area of MoVMn with 38 m^2/g and the small SA of MoVAs with 6.9 m^2/g. At the temperature of 290 °C, unsubstituted $MoVO_x$ increases drastically in conversion rate, while the remaining ranking stays the same.

Changing to an oxygen richer feed with the composition of 10:10:80 (ethane/O_2/N_2) shows slight differences to the other gas feed. Still, there are two "groups" of catalysts visible in the graphs, but while MoVTe, MoVAs, MoVTi, and $MoVO_x$ belonged to the group with lower ethane conversion in the 10:5:85 feed, $MoVO_x$ has now drastically increased its conversion and is now in one "conversion group" with MoVZn, MoVMn, MoVCo, and MoVCr. The highest ethane conversion shows again MoVZn with 15 % at 290 °C, but this time there is no change in activities at the highest temperature – the ranking (Zn > Co > Cr > Mn > $MoVO_x$ > Ti > Te > As) stays the same over the complete temperature range.

When again the surface area of the respective solids is taken into account, unsubstituted $MoVO_x$ shows the highest conversion rate. The new order of catalyst activity is $MoVO_x$ > Zn > As > Cr > Co > Ti > Mn > Te.

Summed up, there is a similar behaviour of the catalysts visible in both gas feed compositions. While there are always two "groups" visible in the graphs – regardless conversion percent or conversion rate – the more oxidising feed with 10:10:80 compositions leads to higher conversions and conversion rates by roughly 25 % compared to the 10:5:85 feed composition. This hints at a dependency of the conversion rates on the O_2 content in the gas feed. To verify this, the ethane conversion rates have been plotted against the oxygen content of the feed at two different temperatures. This is shown in Fig. 6.11.

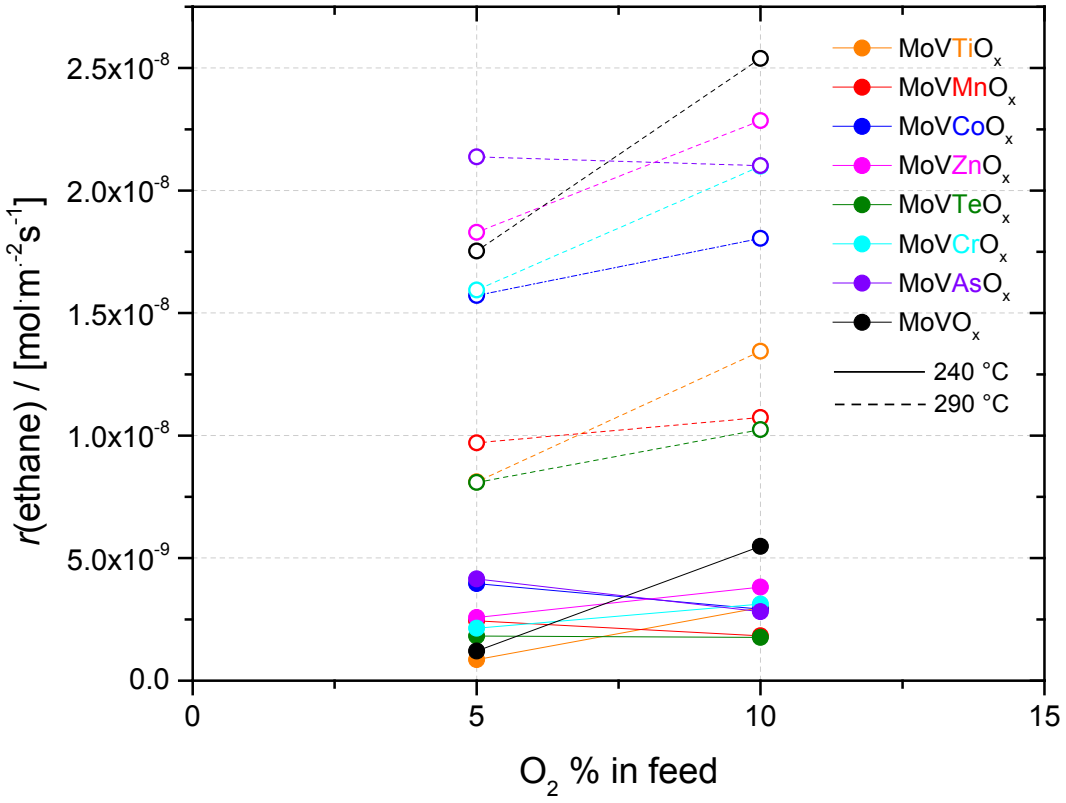

Fig. 6.11: Ethane conversion rate in mol(ethane)/(m^2_{cat}·s) depending on the O_2 content of the gas feed. Straight line indicates rates at 240 °C, dashed line at 290 °C.

It is clearly visible, that the oxygen content influences the activity of all catalysts except for MoVAs and MoVMn at 290 °C. At lower temperatures of 240 °C, unsubstituted $MoVO_x$ and MoVTi show a positive dependency, i.e. the rate increases with increasing O_2 content, while MoVAs and MoVCo display a clearly negative dependency. The remaining solids do not show remarkable changes.

This dependency is visible in the apparent activation energies (Tab. 6.6) as well: a drastic change in apparent activation energies can be observed. Unsubstituted $MoVO_x$ possesses an apparent activation energy of 112.3 kJ/mol in the ODH of ethane, and with that the highest value among all samples at 5 % O_2 in the gas feed. MoVCo and MoVMn show an E_A between 91 and 95 kJ/mol, whereas MoVTe and MoVAs show the lowest apparent activation energies with 84.8 and 88.1 kJ/mol, respectively.

This behaviour turns around when switching to oxygen richer conditions. Herein, MoVTe and MoVAs possess by far the highest activation energies with almost 120 kJ/mol in both cases. Among the other samples, unsubstituted $MoVO_x$ still remains the one with the highest E_A of 96 kJ/mol, while all other substituted samples show apparent activation energies of 90 kJ/mol and below.

Tab. 6.6: Apparent activation energies of (un)substituted MoV based oxides in different ethane/O_2/N_2 gas feed compositions.

Sample #	Substituent	E_A / kJ/mol (10:5:85)	E_A / kJ/mol (10:10:80)
27123	Ti	105.6	88.8
27191	Mn	91.9	83.6
27554	Co	94.4	87.5
27631	Zn	101.7	85.5
27657	Te	84.8	116.1
27665	Cr	103.4	90.4
28552	As	88.1	117.9
28116	-	112.3	95.9

High activation energy indicates the possibility of a stronger reaction rate increase with increasing temperature. Comparing the ethane conversion rates with the apparent activation energies of the catalysts in the respective gas feeds finds this to be true. Samples with higher activation energy show a stronger increase in ethane conversion over the temperature range.

During the oxidative dehydrogenation reaction of ethane, four different products are formed in both feed compositions: ethylene, acetic acid, carbon dioxide, and carbon monoxide. The selectivity-conversion plots for the respective products in the gas feed of 10:5:85 ethane/oxygen/nitrogen are shown in Fig. 6.12.

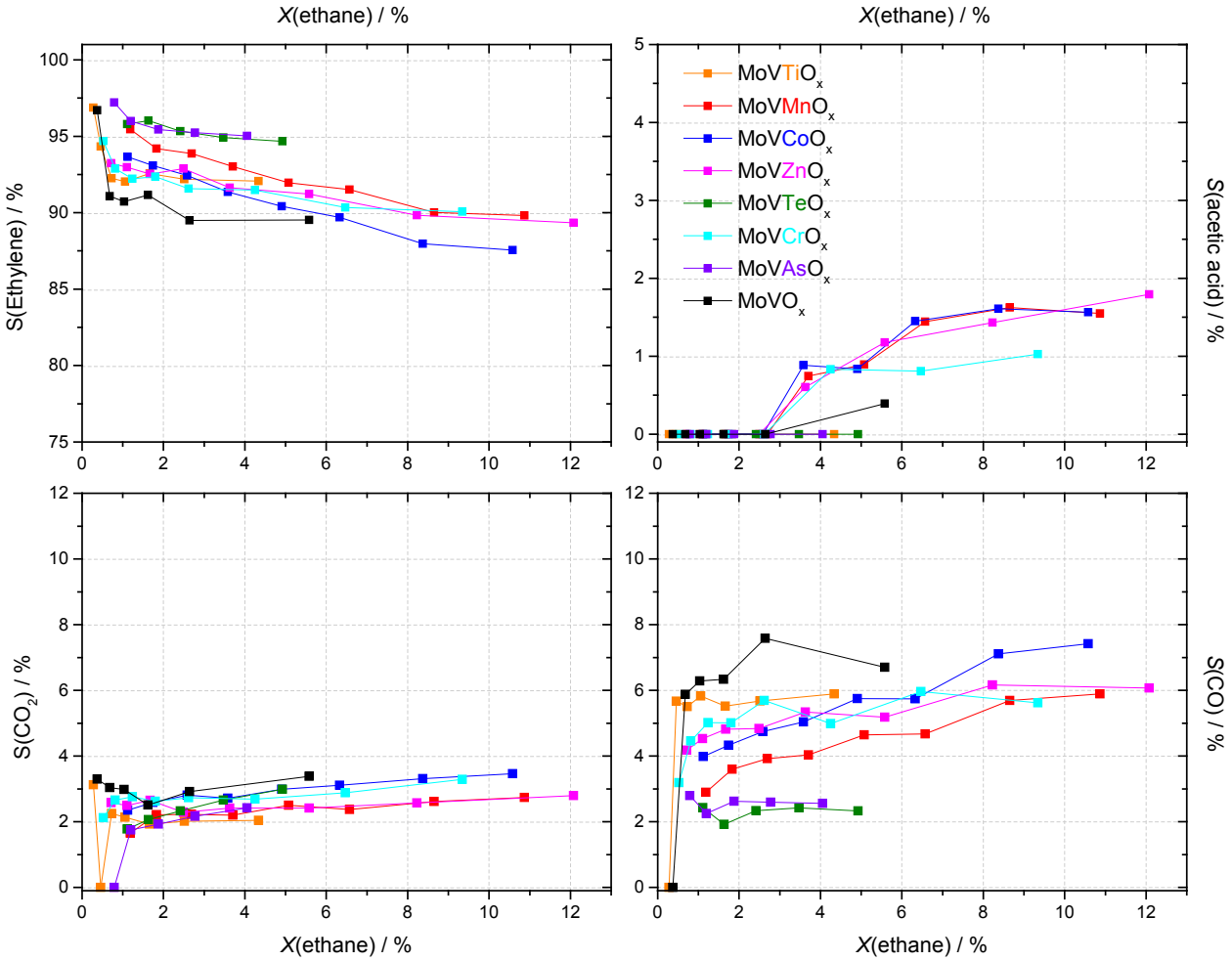

Fig. 6.12: Selectivity to ethylene, acetic acid, CO_2 and CO depending on the ethane conversion. Gas feed composition ethane/O_2/N_2 10:5:85, 200 mg catalyst, 20 mL/min, 200-290 °C.

For ethane conversions > 1 %, the slope of selectivity decrease flattens in all solids. In this range, MoVCo and MoVMn show slope-wise the most significant loss in selectivity, with a decrease from 93.9 % to 87.5 % and from 95.6 % to 89.8 %, respectively. On the other hand, MoVTe, MoVAs, MoVTi, and unsubstituted $MoVO_x$ decrease in ethylene selectivity only barely over their respective conversion ranges. These are the same catalysts, which perform ethane oxidation at lower conversions in the applied temperature range from 200 to 290 °C, while the manganese and cobalt substituted MoV oxides are among the ones with the highest conversions. It is obvious that lower conversion rates are more favourable for the formation of ethylene in these catalysts. The corresponding ethylene formation rates at 290 °C for both gas feed compositions are listed in Tab. 6.7.

Tab. 6.7 Ethylene formation rates at 290 °C for all MoV based samples at different ethane/O_2/N_2 gas feed compositions.

sample	Ethylene formation rate / $mol_{ethylene}/m^2s$ 10:5:85	Ethylene formation rate / $mol_{ethylene}/m^2s$ 10:10:80
MoVTi	$1.58 \cdot 10^{-8}$	$2.62 \cdot 10^{-8}$
MoVMn	$1.91 \cdot 10^{-8}$	$2.09 \cdot 10^{-8}$
MoVCo	$3.41 \cdot 10^{-8}$	$4.15 \cdot 10^{-8}$
MoVZn	$3.78 \cdot 10^{-8}$	$4.66 \cdot 10^{-8}$
MoVTe	$1.60 \cdot 10^{-8}$	$1.94 \cdot 10^{-8}$
MoVCr	$3.23 \cdot 10^{-8}$	$4.21 \cdot 10^{-8}$
MoVAs	$4.55 \cdot 10^{-8}$	$4.34 \cdot 10^{-8}$
MoV	$3.91 \cdot 10^{-8}$	$8.04 \cdot 10^{-8}$

While the selectivity to carbon dioxide for all catalysts stays between 2 and 4 % for all conversions, the selectivity to carbon monoxide ranges between 2 to 8 %. As a results, the ratio of CO to CO_2 is roughly 1 for MoVTe and MoVAs, whereas it lies around 2 for all other substituted catalysts and $MoVO_x$.

The ethane formation rates in this work have been determined at a temperature which is significantly lower than in the known literature. Still, it is possible to gain a rough estimation of the conversion rates at higher temperatures by extrapolation. At 330 °C and a gas feed composition of 10:10:80, an orthorhombic M1 $MoVO_x$ has been reported with an ethylene formation rate of $4.16 \cdot 10^{-7}$ mol/m²s[174]. The unsubstituted $MoVO_x$ prepared in this work only possesses a quarter of this rate with $1.01 \cdot 10^{-7}$ mol/m²s under the same conditions.

At 385 °C, $MoVTeO_x$ (Te/Mo = 0.09) has shown a formation rate of $6.74 \cdot 10^{-7}$ mol/m²s[175], whereas the substituted MoVTe in this work reaches a formation rate of $3.92 \cdot 10^{-7}$ mol/m²s. However, the gas feed composition applied in the work of Aouine et al. was 20:30:50 and consisted with that of twice as much ethane as in our catalytic tests. Hence it might be possible that our MoVTe reaches the same formation rates in the same gas feed with only a fraction of tellurium content (Te/Mo = 0.003).

Acetic acid is only a very minor product in this reaction, which is formed by all catalysts but MoVTe and MoVAs at ethane conversions > 3 %, but never exceeds a selectivity off 1.9 %.

An increase of oxygen concentration in the gas feed does not only lead to slight differences in the possible value of ethane conversion, but is also reflected in the selectivity to the single reaction products, as is demonstrated in Fig. 6.13. In the 10:10:80 ethane/O_2/N_2 gas feed, the level of selectivity decrease to ethylene is similar in all catalysts, whereby MoVTe and MoVAs are the only catalysts with selectivity above 90 % at their highest conversions, while MoVCo exhibits still the lowest ethylene selectivity of 87.5 %.

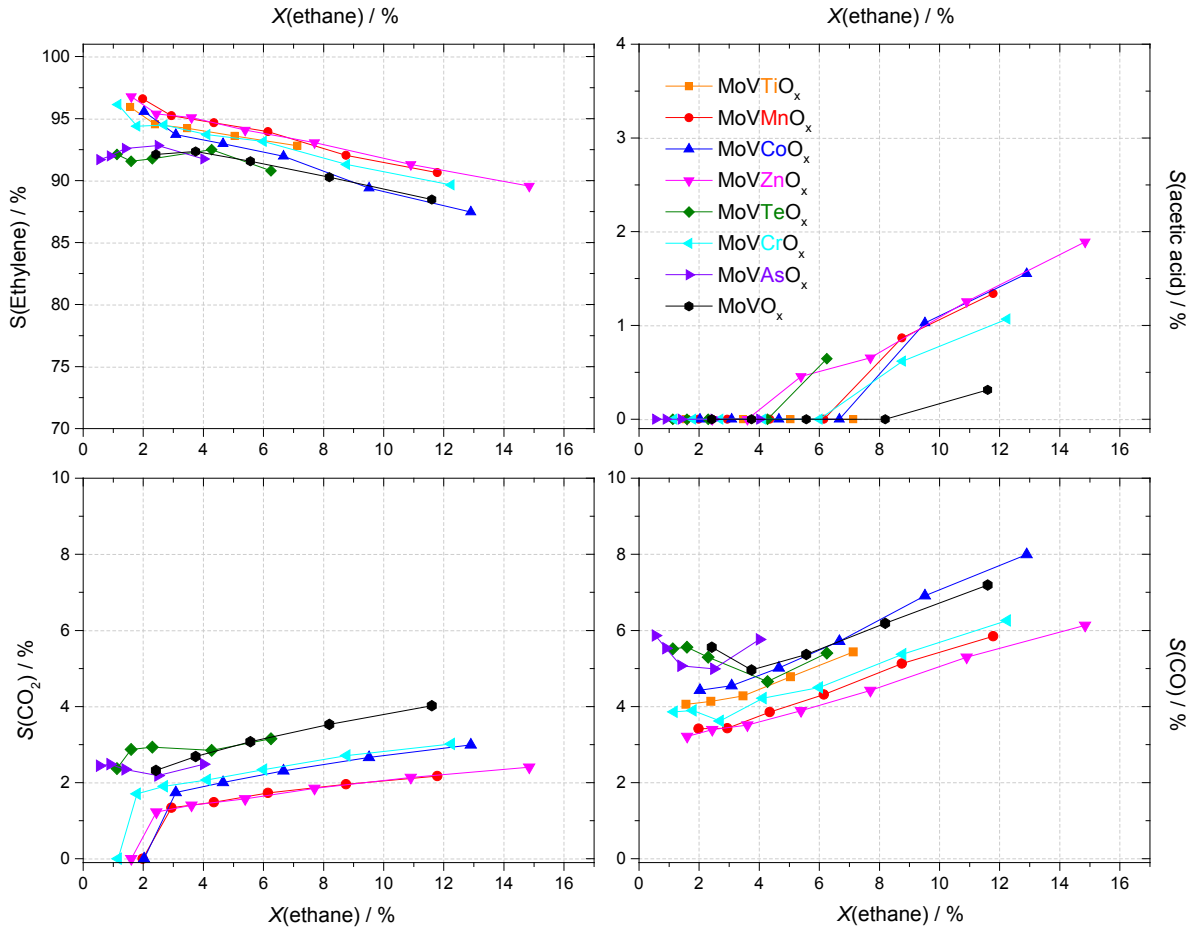

Fig. 6.13: Selectivity to ethylene, acetic acid, CO_2 and CO depending on the ethane conversion. Gas feed composition ethane/O_2/N_2 10:10:80 200 mg catalyst, 20 mL/min, 200-290 °C.

The selectivity values to the carbon oxide species lie in the same percentage regime as in the less oxidative gas feed. However, the ratio of carbon monoxide to carbon dioxide is now around 2 for all samples, indicating a change of mechanism for MoVTe and MoVAs. Acetic acid production does not exceed 2 % in any case and only starts once the ethane conversion is 3 % or higher.

6.4 Conclusion

Synthesis of M1 structured MoV oxide has been carried out at different total metal concentrations in aqueous solution. With decreasing concentration, not only less solid, but also less yield was obtained, reaching the point where no characterisation procedure could be executed. TEM images however revealed that the basic structural motifs of the M1 structure where present even in the resulting 8 mg of the mist diluted synthesis.

Substitution of 1 % of original vanadium concentration was tried out as a way to reduce the vanadium content in the catalyst and with that control the segregation of vanadium to the surface during catalysis, thus possibly increasing catalytic activity. All obtained black solids depict the morphology and crystal structure of orthorhombic M1. All samples show a third metal concentration between 0.2 and 0.3 at%, while the vanadium content has been simultaneously decreased compared to the unsubstituted $MoVO_x$.

Catalytic tests in the oxidative dehydrogenation of ethane in two different gas feed compositions have shown that different substituents have different influences on the catalytic activity dependent on the gas composition. In 10:5:85 ethane/O_2/N_2 environment, MoVTe and MoVAs on one hand depict the lowest ethane conversions, but at the same time show the best selectivity to ethylene among all catalysts. Additionally, the apparent activation energy is also lowest for both these samples. In the oxygen richer feed with a 10:10:80 composition, the ethylene selectivity for the aforementioned catalysts is among the lowest while the apparent activation energies are highest. Plotting the ethane conversion rates against the oxygen content of the gas feed showed an in some cases strong dependency on the oxygen presence, which agrees with the difference in apparent activation energies in different gas feed compositions.

Overall, the substituted ternary MoV oxides surpass the unsubstituted $MoVO_x$ in most cases, regardless of the gas feed composition, but no significant change in catalysis is achieved by the miniscule substitution of vanadium by a third metal.

In the end, neither the precursor speciation of the used polyoxometalates, nor the addition of a third metal during synthesis has a major influence on the catalyst and its properties.

7. Conclusion

In the present work, the speciation of polyoxomolybdates and –vanadates in aqueous solution and in the gas-phase depending on the respective metal concentration in solution and the pH value has been examined with Raman, and UV-vis spectroscopy, as well as with electrospray ionization mass spectrometry, ion mobility spectroscopy, and infrared multiple photon dissociation spectroscopy. Molybdovanadate solutions – which are used as precursor solutions for $MoVO_x$ synthesis – have been investigated with Raman, UV-vis, and mass spectrometry as well.
M1-structured MoV oxide has been synthesised hydrothermally at different precursor concentrations, and with substitution of different transition and main group metals. The latter have been tested in the oxidative dehydrogenation of ethane.

While the examinations of aqueous POM solutions have led to the results known in literature for the given concentration and pH range, mass spectrometric measurements showed an abundance of different species not detected in solution. For molybdate solutions, the structures of the species present in the mass spectrometer and hence gas-phase have been determined via IRMPD spectroscopy, and DFT calculations. Thus, the structural development of molybdates in the gas-phase does not follow linear cluster growth, but can be divided into three different structural domains: chains, rings, and Lindqvist-based structures.

A discrepancy between the speciation in the two media is also observable for vanadates. Furthermore, the speciation in the mass spectrometer is very sensitive to the ionisation conditions, which was not the case for molybdates. This however made it possible to detect the condensed and highly charged decavanadate $[V_{10}O_{28}]^{6-}$ in its protonated form, when the softest – i.e. lowest collision probability – ionisation conditions were applied. Harsher conditions lead to the loss of two oxygen atoms and with that structural rearrangement. Together with the results from the molybdate solutions, it is clear that fragmentation occurs during the ionisation process and that the compact species known to be present in solutions are not stable in their desolvated form.

Examining mixed MoV precursor solutions with different vanadium sources (metavanadate $[VO_3]_n^{n-}$ or vanadyl VO^{2+}) showed that the Keplerate structure $\{Mo_{72}V_{30}\}$ is only formed when vanadyl species are present. In the gas-phase, vanadium was almost completely incorporated in the mixed MoV species in

most cases, and these mixed species tended to become molybdenum-richer with increasing total metal concentration. Mixed MoV species are found in solution, but not in the form of a Keplerate structure but rather as substituted octamolybdates.

Diluting the precursor solution for M1 $MoVO_x$ synthesis led to a simultaneous non-linear decrease of product yield. Together with the results of the MS studies of the respective MoV solutions, the importance of free vanadyl species for the structural rearrangement from $\{Mo_{72}V_{30}\}$ to M1 was discussed. Furthermore, it was observed that the precursor isopolyoxometalate species applied for MoV synthesis do not influence the structural outcome, as when mixing the solutions the same Keplerate structure is formed. However, dilution of the MoV precursor solution led to the increase of an amorphous phase and of the presence of defects in the two dimensional *a*-*b*-plane. The three dimensional crystal structure remained unaffected.

To control the segregation of vanadium during synthesis, the vanadium content for hydrothermal synthesis was reduced by 1 % and replaced by various metals with different oxidation states, but similar ionic radii. The resulting black solids with phase-pure M1 structure contained the third metal in concentrations between 0.2 and 0.3 at%, while the vanadium content has been simultaneously decreased compared to the unsubstituted $MoVO_x$. Catalytic tests in the oxidative dehydrogenation of ethane showed that Te and As as substituents led to the best catalytic results with selectivity to ethylene of 95 % or more at their respective highest conversions and 290 °C and the lowest apparent activation energies. Furthermore, all substituted MoV oxides showed better catalytic results than the unsubstituted M1 $MoVO_x$, showing that the sensitive M1 structure is retained by this approach. Nevertheless, no significant changes in the structure of M1 $MoVO_x$ and its catalytic activity have been achieved by diluting the synthesis solution and by adding a third component to it.

8. References

1. Baes, C.F., Mesmer, R. E., *The Hydrolysis of Cations*. 1986, Malabar, Florida: Robert E. Krieger Publishing Company.
2. Chieregato, A., J.M. López Nieto, and F. Cavani, *Mixed-oxide catalysts with vanadium as the key element for gas-phase reactions.* Coordination Chemistry Reviews, 2015. **301–302**: p. 3-23.
3. Aureliano, M., et al., *Characterization of decavanadate and decaniobate solutions by Raman spectroscopy.* Dalton Transactions, 2016. **45**(17): p. 7391-7399.
4. Maksimovskaya, R.I. and G.M. Maksimov, *Mo-95 and O-17 NMR studies of aqueous molybdate solutions.* Inorganic Chemistry, 2007. **46**(9): p. 3688-3695.
5. Ozeki, T., H. Kihara, and S. Ikeda, *Study of equilibria in 0.03 mM molybdate acidic aqueous solutions by factor analysis applied to ultraviolet spectra.* Analytical Chemistry, 1988. **60**(19): p. 2055-2059.
6. Kung, H.H., *Oxidative dehydrogenation of light (C-2 to C-4) alkanes*, in *Advances in Catalysis, Vol 40*, D.D. Eley, H. Pines, and W.O. Haag, Editors. 1994, Elsevier Academic Press Inc: San Diego. p. 1-38.
7. Grabowski, R., *Kinetics of Oxidative Dehydrogenation of C2-C3 Alkanes on Oxide Catalysts.* Catalysis Reviews: Science and Engineering, 2006. **48**(2): p. 199 - 268.
8. Dobler, J., M. Pritzsche, and J. Sauer, *Oxidation of Methanol to Formaldehyde on Supported Vanadium Oxide Catalysts Compared to Gas Phase Molecules.* Journal of the American Chemical Society, 2005. **127**(31): p. 10861-10868.
9. Deo, G. and I.E. Wachs, *Reactivity of Supported Vanadium Oxide Catalysts: The Partial Oxidation of Methanol.* Journal of Catalysis, 1994. **146**(2): p. 323-334.
10. Deo, G., I.E. Wachs, and J. Haber, *SUPPORTED VANADIUM-OXIDE CATALYSTS - MOLECULAR STRUCTURAL CHARACTERIZATION AND REACTIVITY PROPERTIES.* Critical Reviews in Surface Chemistry, 1994. **4**(3-4): p. 141-187.
11. Demeter, M., M. Neumann, and W. Reichelt, *Mixed-valence vanadium oxides studied by XPS.* Surface Science, 2000. **454**: p. 41-44.
12. Ertl, G., *Reactions at Surfaces: From Atoms to Complexity (Nobel Lecture).* Angewandte Chemie International Edition, 2008. **47**(19): p. 3524-3535.
13. Wachs, I.E., *Recent conceptual advances in the catalysis science of mixed metal oxide catalytic materials.* Catalysis Today, 2005. **100**(1–2): p. 79-94.
14. Dinse, A., et al., *Oxidative dehydrogenation of propane over low-loaded vanadia catalysts: Impact of the support material on kinetics and selectivity.* Journal of Molecular Catalysis A: Chemical, 2008. **289**(1-2): p. 28-37.
15. Diebold, U., *The surface science of titanium dioxide.* Surface Science Reports, 2003. **48**(5-8): p. 53-229.
16. Beck, B., et al., *Partial oxidation of ethanol on vanadia catalysts on supporting oxides with different redox properties compared to propane.* Journal of Catalysis, 2012. **296**(0): p. 120-131.
17. Kim, T. and I.E. Wachs, *CH3OH oxidation over well-defined supported V2O5/Al2O3 catalysts: Influence of vanadium oxide loading and surface vanadium-oxygen functionalities.* Journal of Catalysis, 2008. **255**(2): p. 197-205.
18. Khodakov, A., et al., *Structure and Catalytic Properties of Supported Vanadium Oxides: Support Effects on Oxidative Dehydrogenation Reactions.* Journal of Catalysis, 1999. **181**(2): p. 205-216.

19. Wang, Q.G. and R.J. Madix, *Partial oxidation of methanol to formaldehyde on a model supported monolayer vanadia catalyst: vanadia on TiO2(110).* Surface Science, 2002. **496**(1-2): p. 51-63.
20. Wachs, I.E. and B.M. Weckhuysen, *Structure and reactivity of surface vanadium oxide species on oxide supports.* Applied Catalysis A: General, 1997. **157**(1-2): p. 67-90.
21. Blasco, T. and J.M.L. Nieto, *Oxidative dyhydrogenation of short chain alkanes on supported vanadium oxide catalysts.* Applied Catalysis A: General, 1997. **157**(1-2): p. 117-142.
22. Forzatti, P., et al., *Methanol oxidation over vanadia-based catalysts.* Applied Catalysis a-General, 1997. **157**(1-2): p. 387-408.
23. Wong, G.S., M.R. Concepcion, and J.M. Vohs, *Oxidation of methanol to formaldehyde on vanadia films supported on CeO2(111).* Journal of Physical Chemistry B, 2002. **106**(25): p. 6451-6455.
24. Feng, T. and J.M. Vohs, *A TPD study of the partial oxidation of methanol to formaldehyde on CeO2-supported vanadium oxide.* Journal of Catalysis, 2004. **221**(2): p. 619-629.
25. Fukudome, K. and T. Suzuki, *Highly Selective Oxidative Dehydrogenation of Propane to Propylene over VOx-SiO2 Catalysts.* Catalysis Surveys from Asia, 2015. **19**(3): p. 172-187.
26. Conte, M., et al., *Chemically induced fast solid-state transitions of omega-VOPO4 in vanadium phosphate catalysts.* Science, 2006. **313**(5791): p. 1270-1273.
27. Centi, G. and F. Trifiro, *Functionalization of paraffinic hydrocarbons by heterogeneous vapor-phase oxidation. III. Conversion of the C2-C7 alkane series.* Preprints - American Chemical Society, Division of Petroleum Chemistry, 1987. **32**(3-4): p. 754-62.
28. Centi, G., *Vanadyl Pyrophosphate - A Critical Overview.* Catalysis Today, 1993. **16**(1): p. 5-26.
29. Kiely, C.J., et al., *Characterisation of variations in vanadium phosphate catalyst microstructure with preparation route.* Journal of Catalysis, 1996. **162**(1): p. 31-47.
30. Centi, G. and F. Trifiro, *Functionalization of paraffinic hydrocarbons by heterogeneous vapor-phase oxidation. III. Conversion of the C1-C7 alkane series.* Catalysis Today, 1988. **3**(2-3): p. 151-62.
31. Kholdeeva, O.A., et al., *Mechanisms of oxidant activation in alkene epoxidation catalyzed by monosubstituted heteropolytungstates.* Kinetics and Catalysis, 1997. **38**(4): p. 507-512.
32. Kholdeeva, O.A., et al., *Unique Catalytic Performance of the Polyoxometalate Ti-2(OH)(2)As2W19O67(H2O) (8-): The Role of 5-Coordinated Titanium in H2O2 Activation.* European Journal of Inorganic Chemistry, 2009(34): p. 5134-5141.
33. Ritorto, M.D., et al., *Decomposition of A-type sandwiches. Synthesis and characterization of new polyoxometalates incorporating multiple d-electron-centered units.* Inorganic Chemistry, 2004. **43**(1): p. 44-49.
34. Neumann, R. and M. Gara, *HIGHLY-ACTIVE MANGANESE-CONTAINING POLYOXOMETALATE AS CATALYST FOR EPOXIDATION OF ALKENES WITH HYDROGEN-PEROXIDE.* Journal of the American Chemical Society, 1994. **116**(12): p. 5509-5510.
35. Ishikawa, E. and T. Yamase, *Kinetics of epoxidation of cyclooctene with H2O2 by alpha-Keggin PTi2W10O38(O-2)(2) (7-) catalyst in acetonitrile.* Journal of Molecular Catalysis a-Chemical, 1999. **142**(1): p. 61-76.
36. Nozaki, C., et al., *Synthesis and characterization of diiron(III)-substituted silicotungstate, gamma(1,2)-SiW10{Fe(OH2)}(2)O-38 (6-).* Inorganic Chemistry, 1999. **38**(25): p. 5724-5729.
37. Kamata, K., et al., *Efficient epoxidation of olefins with >= 99% selectivity and use of hydrogen peroxide.* Science, 2003. **300**(5621): p. 964-966.
38. Kamata, K., et al., *Olefin epoxidation with hydrogen peroxide catalyzed by lacunary polyoxometalate gamma-SiW10O34(H2O)(2) (4-).* Chemistry-a European Journal, 2007. **13**(2): p. 639-648.

39. Hua, L., et al., *A Ti-substituted polyoxometalate as a heterogeneous catalyst for olefin epoxidation with aqueous hydrogen peroxide.* New Journal of Chemistry, 2011. **35**(9): p. 1836-1841.
40. Balula, M.S.S., et al., *A comparative study between Keggin-type tungstophosphates and tungstosilicates in the oxidation of cyclooctane with hydrogen peroxide.* Journal of Molecular Catalysis a-Chemical, 2004. **222**(1-2): p. 159-165.
41. Adam, W., et al., *A highly chemoselective, diastereoselective, and regioselective epoxidation of chiral allylic alcohols with hydrogen peroxide, catalyzed by sandwich-type polyoxometalates: Enhancement of reactivity and control of selectivity by the hydroxy group through metal-alcoholate bonding.* Journal of Organic Chemistry, 2003. **68**(5): p. 1721-1728.
42. Zhizhina, E.G., et al., *Homogeneous catalytic oxidation of propene to acetone and butene-1 to butanone in the presence of palladium and molybdovanadophosphoric heteropoly acid.* Applied Catalysis a-General, 2007. **319**: p. 91-97.
43. Guo, W., et al., *Aerobic Oxidation of Formaldehyde Catalyzed by Polyvanadotungstates.* Acs Catalysis, 2014. **4**(4): p. 1154-1161.
44. Sloboda-Rozner, D., K. Neimann, and R. Neumann, *Aerobic oxidation of aldehydes catalyzed by epsilon-Keggin type polyoxometalates (Mo12O39)-O-V(mu(2)-OH)(10)H-2{X-II(H2O)(3)}(4) (X = Ni, Co, Mn and Cu) as heterogeneous catalysts.* Journal of Molecular Catalysis a-Chemical, 2007. **262**(1-2): p. 109-113.
45. Sun, M., et al., *Catalytic Oxidation of Light Alkanes (C1–C4) by Heteropoly Compounds.* Chemical Reviews, 2014. **114**(2): p. 981-1019.
46. Khenkin, A.M., et al., *Electron and oxygen transfer in polyoxometalate, H5PV2Mo10O40, catalyzed oxidation of aromatic and alkyl aromatic compounds: Evidence for aerobic Mars-van Krevelen-type reactions in the liquid homogeneous phase.* Journal of the American Chemical Society, 2001. **123**(35): p. 8531-8542.
47. Bordoloi, A., E. Lefebvre, and S.B. Halligudi, *Selective oxidation of anthracene using inorganic-organic hybrid materials based on molybdovanadophosphoric acids.* Journal of Catalysis, 2007. **247**(2): p. 166-175.
48. Al-Oweini, R., S. Aghyarian, and H. El-Rassy, *Immobilized polyoxometalates onto mesoporous organically-modified silica aerogels as selective heterogeneous catalysts of anthracene oxidation.* Journal of Sol-Gel Science and Technology, 2012. **61**(3): p. 541-550.
49. Wang, R., et al., *Performance evaluation of the carbon nanotubes supported Cs2.5H0.5PW12O40 as efficient and recoverable catalyst for the oxidative removal of dibenzothiophene.* Catalysis Today, 2010. **150**(1-2): p. 37-41.
50. Rafiee, E. and N. Rahpeyma, *Selective oxidation of sulfurs and oxidation desulfurization of model oil by 12-tungstophosphoric acid on cobalt-ferrite nanoparticles as magnetically recoverable catalyst.* Chinese Journal of Catalysis, 2015. **36**(8): p. 1342-1349.
51. Rafiee, E. and N. Nobakht, *Keggin type heteropoly acid, encapsulated in metal-organic framework: A heterogeneous and recyclable nanocatalyst for selective oxidation of sulfides and deep desulfurization of model fuels.* Journal of Molecular Catalysis a-Chemical, 2015. **398**: p. 17-25.
52. Sloboda-Rozner, D., et al., *Aqueous biphasic oxidation: A water-soluble polyoxometalate catalyst for selective oxidation of various functional groups with hydrogen peroxide.* Advanced Synthesis & Catalysis, 2004. **346**(2-3): p. 339-345.
53. Tundo, P., et al., *Multiphase oxidation of aniline to nitrosobenzene with hydrogen peroxide catalyzed by heteropolyacids.* Synlett, 2008(7): p. 967-970.
54. Mayer, C.R. and R. Thouvenot, *Organophosphoryl derivatives of trivacant tungstophosphates of general formula alpha-A- PW9O34(RPO)(2) (5-): synthesis and structure determination by*

multinuclear magnetic resonance spectroscopy (P-31, W-183). Journal of the Chemical Society-Dalton Transactions, 1998(1): p. 7-13.

55. Mayer, C.R., P. Herson, and R. Thouvenot, *Organic-inorganic hybrids based on polyoxometalates. 5. Synthesis and structural characterization of bis(organophosphoryl)decatungtosilicates gamma-SiW10O36((RPO)(2) (4-).* Inorganic Chemistry, 1999. **38**(26): p. 6152-6158.
56. Tran, M.H., et al., *Hydrothermal synthesis of molybdenum oxide catalyst: Heteropoly acids encaged in US-Y.* Applied Catalysis a-General, 2005. **287**(1): p. 129-134.
57. Pamin, K., et al., *Immobilization of dodecatungstophosphoric acid on dealuminated zeolite Y: a physicochemical study.* Applied Catalysis a-General, 2000. **194**: p. 137-146.
58. Olejniczak, Z., et al., *Heterogenization of 12-tungstophosphoric acid on stabilized zeolite Y.* Topics in Catalysis, 2000. **11**(1-4): p. 391-400.
59. Singh, S., N. Narkhede, and A. Patel, *Aerobic oxidation of alcohols and alkenes over a novel lacunary phosphomolybdate anchored to zeolite H beta.* Rsc Advances, 2015. **5**(46): p. 36270-36278.
60. Saedi, Z., et al., *The effect of encapsulated Zn-POM on the catalytic activity of MIL-101 in the oxidation of alkenes with hydrogen peroxide.* Journal of Coordination Chemistry, 2012. **65**(3): p. 463-473.
61. Maksimchuk, N.V., et al., *Hybrid Polyoxotungstate/MIL-101 Materials: Synthesis, Characterization, and Catalysis of H2O2-Based Alkene Epoxidation.* Inorganic Chemistry, 2010. **49**(6): p. 2920-2930.
62. Yang, X.-L., L.-M. Qiao, and W.-L. Dai, *Phosphotungstic acid encapsulated in metal-organic framework UiO-66: An effective catalyst for the selective oxidation of cyclopentene to glutaraldehyde.* Microporous and Mesoporous Materials, 2015. **211**: p. 73-81.
63. Vedrine, J.C., *Heterogeneous catalytic partial oxidation of lower alkanes (C-1 - C-6) on mixed metal oxides.* Journal of Energy Chemistry, 2016. **25**(6): p. 936-946.
64. Kwon, T., G.A. Tsigdinos, and T.J. Pinnavaia, *PILLARING OF LAYERED DOUBLE HYDROXIDES (LDHS) BY POLYOXOMETALATE ANIONS.* Journal of the American Chemical Society, 1988. **110**(11): p. 3653-3654.
65. Yun, S.K. and T.J. Pinnavaia, *Layered double hydroxides intercalated by polyoxometalate anions with Keggin (alpha-H2W12O406-), Dawson (alpha-P2W18O626-), and Finke (Co-4(H2O)(2)(PW9O34)(2)(10-)) structures.* Inorganic Chemistry, 1996. **35**(23): p. 6853-6860.
66. Liu, K., Z. Yao, and Y.-F. Song, *Polyoxometalates Hosted in Layered Double Hydroxides: Highly Enhanced Catalytic Activity and Selectivity in Sulfoxidation of Sulfides.* Industrial & Engineering Chemistry Research, 2015. **54**(37): p. 9133-9141.
67. Li, T.F., H.N. Miras, and Y.F. Song, *Polyoxometalate (POM)-Layered Double Hydroxides (LDH) Composite Materials: Design and Catalytic Applications.* Catalysts, 2017. **7**(9): p. 17.
68. Tatsumi, T., et al., *SHAPE SELECTIVE EPOXIDATION OF ALKENES CATALYZED BY POLYOXOMETALATE-INTERCALATED HYDROTALCITE.* Chemistry Letters, 1992(5): p. 815-818.
69. Li, T., et al., *Rational Design of a Polyoxometalate Intercalated Layered Double Hydroxide: Highly Efficient Catalytic Epoxidation of Allylic Alcohols under Mild and Solvent-Free Conditions.* Chemistry-a European Journal, 2017. **23**(5): p. 1069-1077.
70. Liu, K., et al., *Polyoxometalate-Intercalated Layered Double Hydroxides as Efficient and Recyclable Bifunctional Catalysts for Cascade Reactions.* Chemcatchem, 2016. **8**(5): p. 929-937.
71. Grasselli, R.K., *Site isolation and phase cooperation: Two important concepts in selective oxidation catalysis: A retrospective.* Catalysis Today, 2014. **238**(0): p. 10-27.
72. Vedrine, J.C., *Heterogeneous Partial (amm) Oxidation and Oxidative Dehydrogenation Catalysis on Mixed Metal Oxides.* Catalysts, 2016. **6**(2).

73. Thorsteinson, E.M., et al., *The oxidative dehydrogenation of ethane over catalysts containing mixed oxides of molybdenum and vanadium.* Journal of Catalysis, 1978. **52**(1): p. 116-132.
74. Woo, J., et al., *A study of M1/M2 phase synergy in the MoVTe(Nb,Ta)O catalysts for propane ammoxidation to acrylonitrile.* Applied Catalysis A: General, 2016. **515**: p. 179-189.
75. Kube, P., et al., *Functional Analysis of Catalysts for Lower Alkane Oxidation.* Chemcatchem, 2017. **9**(4): p. 573-585.
76. Ueda, W., *Establishment of Crystalline Complex Mo-V-Oxides as Selective Oxidation Catalysts.* Journal of the Japan Petroleum Institute, 2013. **56**(3): p. 122-132.
77. Trunschke, A., et al., *The Impact of the Bulk Structure on Surface Dynamics of Complex Mo-V-based Oxide Catalysts.* Acs Catalysis, 2017. **7**(4): p. 3061-3071.
78. Messaoudi, S., et al., *A density functional study of the dimerization mechanisms of molybdenum(vi) in aqueous solution.* Physical Chemistry Chemical Physics, 2004. **6**(9): p. 2083-2087.
79. Oyerinde, O.F., et al., *Solution structure of molybdic acid from Raman spectroscopy and DFT analysis.* Inorganica Chimica Acta, 2008. **361**(4): p. 1000-1007.
80. Tossell, J.A., *Calculating the partitioning of the isotopes of Mo between oxidic and sulfidic species in aqueous solution.* Geochimica et Cosmochimica Acta, 2005. **69**(12): p. 2981-2993.
81. Cruywagen, J.J., *Protonation, oligomerization, and condensation reactions of vanadate(V), molybdate(VI), and tungstate(VI).* Advances in Inorganic Chemistry, Vol 49, 2000. **49**: p. 127-182.
82. Cao, D.J., et al., *Study on the standard pattern of Raman spectrum of heptamolybdate ion in aqueous solution*. Sohn International Symposium Advanced Processing of Metals and Materials, Vol 3: Thermo and Physicochemical Principles: Special Materials and Aqueous and Electrochemical Processing, ed. F. Kongoli and R.G. Reddy. 2006, Warrendale: Minerals, Metals & Materials Soc. 507-+.
83. Cao, D.J., et al., *Investigation on chemical components in saturated aqueous solution of ammonium dimolybdate by comparative Raman spectroscopy*. Sohn International Symposium Advanced Processing of Metals and Materials, Vol 3: Thermo and Physicochemical Principles: Special Materials and Aqueous and Electrochemical Processing, ed. F. Kongoli and R.G. Reddy. 2006, Warrendale: Minerals, Metals & Materials Soc. 517-+.
84. Johansson, G., L. Pettersson, and N. Ingri, *FORMATION OF HEPTAMOLYBDATE AND OCTAMOLYBDATE IN AQUEOUS-SOLUTION - X-RAY-SCATTERING AND RAMAN MEASUREMENTS.* Acta Chemica Scandinavica Series a-Physical and Inorganic Chemistry, 1979. **33**(4): p. 305-312.
85. Tytko, K.H., et al., *MACROISOPOLYANION OF MOLYBDENUM - MO36O8-/112.* Angewandte Chemie-International Edition in English, 1973. **12**(4): p. 330-332.
86. Tytko, K.H. and G. Baethe, *On the polymolybdate types occurring at high degrees of acidification, with particular reference to the \"decamolybdates\" and \"phase C\" polymolybdates.* Zeitschrift fuer Anorganische und Allgemeine Chemie, 1987. **555**: p. 85-97.
87. Ng, K.Y.S. and E. Gulari, *Spectroscopic and scattering investigation of isopoly-molybdate and tungstate solutions.* Polyhedron, 1984. **3**(8): p. 1001-1011.
88. Tytko, K.H., G. Baethe, and J.J. Cruywagen, *EQUILIBRIUM STUDIES OF AQUEOUS POLYMOLYBDATE SOLUTIONS IN 1-M NACL MEDIUM AT 25-DEGREES-C.* Inorganic Chemistry, 1985. **24**(20): p. 3132-3136.
89. Coddington, J.M. and M.J. Taylor, *MO-95 NUCLEAR MAGNETIC-RESONANCE AND VIBRATIONAL SPECTROSCOPIC STUDIES OF MOLYBDENUM(VI) SPECIES IN AQUEOUS-SOLUTIONS AND SOLVENT EXTRACTS FROM HYDROCHLORIC AND HYDROBROMIC ACID - EVIDENCE FOR THE COMPLEXES MO2O5(H2O)6 2+, MOO2X2(H2O)2 (X = CL OR BR), AND MOO2CL4 2.* Journal of the Chemical Society-Dalton Transactions, 1990(1): p. 41-47.

90. Krishnan, C.V., et al., *Electrochemical measurements of isopolyoxomolybdates: 1. pH dependent behavior of sodium molybdate.* International Journal of Electrochemical Science, 2007. **2**(1): p. 29-51.
91. Baes, C.F.M., R.E., *The Hydrolysis of Cations.* Robert E. Krieger Publishing Company, 1986.
92. Sasaki, Y., I. Lindqvist, and L.G. Sillén, *On the first equilibrium steps in the acidification of the molybdate ion.* Journal of Inorganic and Nuclear Chemistry, 1959. **9**(1): p. 93-94.
93. Aveston, J., E.W. Anacker, and J.S. Johnson, *Hydrolysis of Molybdenum(VI). Ultracentrifugation, Acidity Measurements, and Raman Spectra of Polymolybdates.* Inorganic Chemistry, 1964. **3**(5): p. 735-746.
94. Sillén, Y.S.a.L.G., *Equilibrium studies of polyanions - 16. Equilibria of molybdates in 3 M Na(ClO4) medium at 25°C.* Arkiv För Kemi, 1967. **29**(253-277).
95. Haeringer, M. and J.P. Schwing, 1967. **2**: p. 708-718.
96. Maksimovskaya, R.I., V.M. Bondareva, and G.I. Aleshina, *NMR Spectroscopic Studies of Interactions in Solution during the Synthesis of MoVTeNb Oxide Catalysts.* European Journal of Inorganic Chemistry, 2008. **2008**(31): p. 4906-4914.
97. Noack, J., et al., *Speciation of Molybdates under Hydrothermal Conditions.* Zeitschrift für anorganische und allgemeine Chemie, 2014. **640**(14): p. 2730-2736.
98. Minubayeva, Z. and T.M. Seward, *Molybdic acid ionisation under hydrothermal conditions to 300 degrees C.* Geochimica Et Cosmochimica Acta, 2010. **74**(15): p. 4365-4374.
99. Liu, X., et al., *Solution Structures and Acidity Constants of Molybdic Acid.* The Journal of Physical Chemistry Letters, 2013. **4**(17): p. 2926-2930.
100. Pope, M.T., *Heteropoly and Isopoly Oxometalates*. Inorganic Chemistry Concepts, ed. C.K.e.a. Jorgensen. Vol. 8. 1983, Berlin, Heidelberg, New York, Tokyo: Springer-Verlag.
101. Newman, L., et al., *A SPECTROPHOTOMETRIC INVESTIGATION OF VANADIUM(V) SPECIES IN ALKALINE SOLUTIONS.* Journal of the American Chemical Society, 1958. **80**(17): p. 4491-4495.
102. Pettersson, L., et al., *MULTICOMPONENT POLYANIONS .36. HYDROLYSIS AND REDOX EQUILIBRIA OF THE H+-HVO42- SYSTEM IN 0.6 M NA(CL) - A COMPLEMENTARY POTENTIOMETRIC AND V-51 NMR-STUDY AT LOW VANADIUM CONCENTRATIONS IN ACID-SOLUTION.* Acta Chemica Scandinavica Series a-Physical and Inorganic Chemistry, 1985. **39**(7): p. 499-506.
103. Pettersson, L., I. Andersson, and B. Hedman, *MULTICOMPONENT POLYANIONS .37. A POTENTIOMETRIC AND V-51-NMR STUDY OF EQUILIBRIA IN THE H+-HVO4(2-) SYSTEM IN 3.0 M-NA(ClO4) MEDIUM COVERING THE RANGE 1 LESS-THAN-OR-EQUAL-TO -IG H+ LESS-THAN-OR-EQUAL-TO 10.* Chemica Scripta, 1985. **25**(4): p. 309-317.
104. Cruywagen, J.J. and J.B.B. Heyns, *VANADIUM(V) EQUILIBRIA - SPECTROPHOTOMETRIC AND ENTHALPIMETRIC INVESTIGATION OF THE DIMERIZATION AND DEPROTONATION OF HVO42.* Polyhedron, 1991. **10**(2): p. 249-253.
105. Cruywagen, J.J., J.B.B. Heyns, and A.N. Westra, *Protonation equilibria of mononuclear vanadate: Thermodynamic evidence for the expansion of the coordination number in VO2+.* Inorganic Chemistry, 1996. **35**(6): p. 1556-1559.
106. Konnert, J.A. and H.T. Evans, *CALCIUM DIVANADATE DIHYDRATE.* Acta Crystallographica Section B-Structural Science, 1975. **31**(NOV15): p. 2688-2690.
107. Andersson, I., et al., *Oxygen and vanadium exchange processes in linear vanadate oligomers.* Journal of the Chemical Society-Dalton Transactions, 1996(16): p. 3357-3361.
108. McCann, N., M. Wagner, and H. Hasse, *A thermodynamic model for vanadate in aqueous solution - equilibria and reaction enthalpies.* Dalton Transactions, 2013. **42**(7): p. 2622-2628.
109. Fuchs, J., S. Mahjour, and J. Pickardt, *STRUCTURE OF TRUE METAVANADATE ION.* Angewandte Chemie-International Edition in English, 1976. **15**(6): p. 374-375.

110. Sadoc, A., et al., *Structure and stability of VO2+ in aqueous solution: A car-parrinello and static ab initio study.* Inorganic Chemistry, 2007. **46**(12): p. 4835-4843.
111. Buhl, M., *Speciation of Peroxovanadium(V) Complexes Studied by First-Principles Molecular Dynamics Simulations and (51)V NMR Chemical Shift Computations*, in *Vanadium: The Verastile Metal*, K. Kustin, J.C. Pessoa, and D.C. Crans, Editors. 2007, Amer Chemical Soc: Washington. p. 312-322.
112. Howarth, O.W., L. Pettersson, and I. Andersson, *MONOMOLYBDONONAVANADATE AND CIS-DIMOLYBOO-OCTAVANADATE AND TRANS-DIMOLYBDO-OCTAVANADATE.* Journal of the Chemical Society-Dalton Transactions, 1989(10): p. 1915-1923.
113. Harrison, A.T. and O.W. Howarth, *OXYGEN-EXCHANGE AND PROTONATION OF POLYANIONS - A MULTINUCLEAR MAGNETIC-RESONANCE STUDY OF TETRADECAVANADOPHOSPHATE(9-) AND DECAVANADATE(6-).* Journal of the Chemical Society-Dalton Transactions, 1985(9): p. 1953-1957.
114. Howarth, O.W., L. Pettersson, and I. Andersson, *AQUEOUS MOLYBDOVANADATES AT HIGH MO-V RATIO.* Journal of the Chemical Society-Dalton Transactions, 1991(7): p. 1799-1812.
115. Nenner, A.M., *MULTICOMPONENT POLYANIONS .38. STRUCTURE OF K5NAMO6V2O26.4H2O, A COMPOUND CONTAINING A NEW CONFIGURATION OF THE HEXAMOLYBDODIVANADATE ANION.* Acta Crystallographica Section C-Crystal Structure Communications, 1985. **41**: p. 1703-1707.
116. Sadakane, M., et al., *Assembly of a Pentagonal Polyoxomolybdate Building Block, [Mo6O21]6–, into Crystalline MoV Oxides.* European Journal of Inorganic Chemistry, 2013. **2013**(10-11): p. 1731-1736.
117. Celaya Sanfiz, A., et al., *Preparation of Phase-Pure M1 MoVTeNb Oxide Catalysts by Hydrothermal Synthesis-Influence of Reaction Parameters on Structure and Morphology.* Topics in Catalysis, 2008. **50**(1-4): p. 19-32.
118. Ishikawa, S., et al., *Synthesis of Novel Orthorhombic Mo and V Based Complex Oxides Coordinating Alkylammonium Cation in Its Heptagonal Channel and Their Application as a Catalyst.* Chemistry of Materials, 2013. **25**(11): p. 2211-2219.
119. Cruywagen, J.J. and J.B.B. Heyns, *Molybdenum(VI) equilibria at high perchloric acid concentration.* Polyhedron, 2000. **19**(8): p. 907-911.
120. Cruywagen, J.J., et al., *Molybdenum(VI) equilibria in different ionic media. Formation constants and thermodynamic quantities.* Inorganica Chimica Acta, 2002. **331**(1): p. 322-329.
121. Wang, M.-Y., et al., *Existing form of Mo(VI) in acidic sulfate solution.* Rare Metals, 2017. **36**(7): p. 612-616.
122. Borg, S., et al., *An XAS study of molybdenum speciation in hydrothermal chloride solutions from 25–385 °C and 600 bar.* Geochimica et Cosmochimica Acta, 2012. **92**: p. 292-307.
123. Kurbatova, L.D. and D.I. Kurbatov, *Vanadium(V) complexes in sulfuric acid solutions.* Russian Journal of Inorganic Chemistry, 2006. **51**(5): p. 841-843.
124. Ishikawa, S. and W. Ueda, *Microporous crystalline Mo-V mixed oxides for selective oxidations.* Catalysis Science & Technology, 2016. **6**(3): p. 617-629.
125. Beato, P., et al., *Analysis of structural transformations during the synthesis of a MoVTeNb mixed oxide catalyst.* Applied Catalysis, A: General, 2006. **307**(1): p. 137-147.
126. Bondareva, V.M., et al., *The formation of an active component in V-Mo-Nb-O catalysts of ethane oxidation and amnioxidation.* Reaction Kinetics and Catalysis Letters, 2006. **88**(1): p. 183-191.
127. Kolen'ko, Y.V., et al., *Synthesis of MoVTeNb Oxide Catalysts with Tunable Particle Dimensions.* ChemCatChem, 2011. **3**(10): p. 1597-1606.

128. Girgsdies, F., R. Schlogl, and A. Trunschke, *In-situ X-ray diffraction study of phase crystallization from an amorphous MoVTeNb oxide catalyst precursor.* Catalysis Communications, 2012. **18**: p. 60-62.
129. Katou, T., D. Vitry, and W. Ueda, *Structure dependency of Mo-V-O-based complex oxide catalysts in the oxidations of hydrocarbons.* Catalysis Today, 2004. **91-92**(1): p. 237-240.
130. Ivars-Barceló, F., et al., *Understanding effects of activation-treatments in K-free and K-MoVSbO bronze catalysts for propane partial oxidation.* Catalysis Today, 2014. **238**(0): p. 41-48.
131. Dieterle, M., et al., *Mixed molybdenum oxide based partial oxidation catalyst: 2. Combined X-ray diffraction, electron microscopy and Raman investigation of the phase stability of (MoVW)5O14-type oxides.* Journal of Molecular Catalysis A: Chemical, 2001. **174**(1-2): p. 169-185.
132. Zenkovets, G.A., et al., *The structural genesis of a complex (MoVW)5O14 oxide during thermal treatments and its redox behavior at elevated temperatures.* Materials Chemistry and Physics, 2007. **103**(2-3): p. 295-304.
133. Knobl, S., et al., *The synthesis and structure of a single-phase, nanocrystalline MoVW mixed-oxide catalyst of the Mo5O14 type.* Journal of Catalysis, 2003. **215**(2): p. 177-187.
134. Roussel, M., et al., *MoVO-based catalysts for the oxidation of ethane to ethylene and acetic acid: Influence of niobium and/or palladium on physicochemical and catalytic properties.* Applied Catalysis A: General, 2006. **308**(0): p. 62-74.
135. Blum, V., et al., *Ab initio molecular simulations with numeric atom-centered orbitals.* Computer Physics Communications, 2009. **180**(11): p. 2175-2196.
136. Perdew, J.P., K. Burke, and M. Ernzerhof, *Generalized Gradient Approximation Made Simple.* Physical Review Letters, 1996. **77**(18): p. 3865-3868.
137. Tkatchenko, A. and M. Scheffler, *Accurate Molecular Van Der Waals Interactions from Ground-State Electron Density and Free-Atom Reference Data.* Physical Review Letters, 2009. **102**(7): p. 4.
138. Bussi, G., D. Donadio, and M. Parrinello, *Canonical sampling through velocity rescaling.* Journal of Chemical Physics, 2007. **126**(1): p. 7.
139. Rossi, M., M. Scheffler, and V. Blum, *Impact of Vibrational Entropy on the Stability of Unsolvated Peptide Helices with Increasing Length.* Journal of Physical Chemistry B, 2013. **117**(18): p. 5574-5584.
140. E, W.N., W.Q. Ren, and E. Vanden-Eijnden, *Simplified and improved string method for computing the minimum energy paths in barrier-crossing events.* Journal of Chemical Physics, 2007. **126**(16): p. 8.
141. Bajuk-Bogdanović, D., et al., *Study of the decomposition pathway of 12-molybdophosphoric acid in aqueous solutions by micro Raman spectroscopy.* Spectrochimica Acta Part A: Molecular and Biomolecular Spectroscopy, 2016. **153**: p. 152-159.
142. Griffith, W.P. and P.J.B. Lesniak, *Raman studies on species in aqueous solutions. Part III. Vanadates, molybdates, and tungstates.* Journal of the Chemical Society A: Inorganic, Physical, Theoretical, 1969(0): p. 1066-1071.
143. Himeno, S., H. Niiya, and T. Ueda, *Raman studies on the identification of isopolymolybdates in aqueous solution.* Bulletin of the Chemical Society of Japan, 1997. **70**(3): p. 631-637.
144. Tytko, K.-H., et al., *A Macroisopolyanion of Molybdenum: Mo36O 8−112.* Angewandte Chemie International Edition in English, 1973. **12**(4): p. 330-332.
145. Pungor, E. and A. Halász, *Spectrophotometric examination of the isopolyacide of molybdenum.* Journal of Inorganic and Nuclear Chemistry, 1970. **32**(4): p. 1187-1197.
146. Wang, J., et al., *Structures and Properties of Two New Three-Dimensional Inorganic-Organic Hybrid Compounds Based on Isopolymolybdate Clusters.* Chinese Journal of Chemistry, 2016. **34**(2): p. 239-245.

147. Ashley, J.H. and P.C.H. Mitchell, *Cobalt-molybdenum-alumina hydrodesulphurisation catalysts. Part I. A spectroscopic and magnetic study of the fresh catalyst and model compounds.* Journal of the Chemical Society A: Inorganic, Physical, Theoretical, 1968(0): p. 2821-2827.
148. Mitchell, P.C.H., *Speciation of molybdenum compounds in water* in *Report of the International Molybdenum Association*, R.M. Consortium, Editor. 2009.
149. K. Walanda, D., et al., *Electrospray mass spectral study of isopolyoxomolybdates.* Journal of the Chemical Society, Dalton Transactions, 1999(3): p. 311-322.
150. Long, D.-L., R. Tsunashima, and L. Cronin, *Polyoxometalates: Building Blocks for Functional Nanoscale Systems.* Angewandte Chemie International Edition, 2010. **49**(10): p. 1736-1758.
151. Hutin, M., D.L. Long, and L. Cronin, *Controlling the Molecular Assembly of Polyoxometalates from the Nano to the Micron Scale: Molecules to Materials.* Israel Journal of Chemistry, 2011. **51**(2): p. 205-214.
152. Fan, L., J. Cao, and C. Hu, *What can electrospray mass spectrometry of paratungstates in an equilibrating mixture tell us?* RSC Advances, 2015. **5**(101): p. 83377-83382.
153. Gunaratne, K.D.D., et al., *Gas-Phase Fragmentation Pathways of Mixed Addenda Keggin Anions: PMo12-nWnO40 (3-) (n=0-12).* Journal of the American Society for Mass Spectrometry, 2015. **26**(6): p. 1027-1035.
154. Schollkopf, W., et al., *The new IR and THz FEL Facility at the Fritz Haber Institute in Berlin*, in *Advances in X-Ray Free-Electron Lasers Instrumentation Iii*, S.G. Biedron, Editor. 2015, Spie-Int Soc Optical Engineering: Bellingham.
155. Gatehouse, B.M. and P. Leverett, *Crystal structure of potassium tetramolybdate, K2Mo4O13, and its relationship to the structures of other univalent metal polymolybdates.* Journal of the Chemical Society A: Inorganic, Physical, Theoretical, 1971(0): p. 2107-2112.
156. Marrot, J. and J.-M. Savariault, *Two Original Infinite Chains in the New Caesium Tetramolybdate Compound Cs2Mo4O13.* Acta Crystallographica Section C, 1995. **51**(11): p. 2201-2205.
157. Schmidt, J., et al., *Infrared Multiphoton Dissociation Spectroscopy Study of Protonated p-Aminobenzoic Acid: Does Electrospray Ionization Afford the Amino- or Carboxy-Protonated Ion?* Journal of Physical Chemistry A, 2011. **115**(26): p. 7625-7632.
158. Tian, Z.X. and S.R. Kass, *Does Electrospray ionization produce gas-phase or liquid-phase structures?* Journal of the American Chemical Society, 2008. **130**(33): p. 10842-+.
159. Schroder, D., M. Budesinsky, and J. Roithova, *Deprotonation of p-Hydroxybenzoic Acid: Does Electrospray Ionization Sample Solution or Gas-Phase Structures?* Journal of the American Chemical Society, 2012. **134**(38): p. 15897-15905.
160. Steill, J.D. and J. Oomens, *Gas-Phase Deprotonation of p-Hydroxybenzoic Acid Investigated by IR Spectroscopy: Solution-Phase Structure Is Retained upon ESI.* Journal of the American Chemical Society, 2009. **131**(38): p. 13570-+.
161. Schröder, D., *Applications of Electrospray Ionization Mass Spectrometry in Mechanistic Studies and Catalysis Research.* Accounts of Chemical Research, 2012. **45**(9): p. 1521-1532.
162. Griffith, W.P. and T.D. Wickins, *RAMAN STUDIES ON SPECIES IN AQUEOUS SOLUTIONS .1. VANADATES.* Journal of the Chemical Society a -Inorganic Physical Theoretical, 1966(8): p. 1087-&.
163. Hardcastle, F.D. and I.E. Wachs, *Determination of the molecular structures of tungstates by Raman spectroscopy.* Journal of Raman Spectroscopy, 1995. **26**(6): p. 397-405.
164. Mestiri, I., I. Nagazi, and A. Haddad, *Synthesis and structural characterization of diammonium bis[octaaquastrontium] decavanadate dehydrate (NH4)2[Sr(OH2)8]2 .V10O28.2H2O*. 2015.
165. Mutlu, E., et al., *Characterization of aqueous formulations of tetra- and pentavalent forms of vanadium in support of test article selection in toxicology studies.* Environmental Science and Pollution Research, 2017. **24**(1): p. 405-416.

166. Walanda, D.K., et al., *Unknown isopolyoxovanadate species detected by electrospray mass spectrometry.* Inorganica Chimica Acta, 2000. **305**(2): p. 118-126.
167. Walanda, D.K., et al., *New isopolyoxovanadate ions identified by electrospray mass spectrometry.* Inorganic Chemistry Communications, 1999. **2**(10): p. 487-489.
168. Frost, R.L., et al., *Raman and infrared spectroscopy of selected vanadates.* Spectrochimica Acta Part a-Molecular and Biomolecular Spectroscopy, 2005. **61**(5): p. 829-834.
169. Müller, A., et al., *Triangular Geometrical and Magnetic Motifs Uniquely Linked on a Spherical Capsule Surface.* Angewandte Chemie International Edition, 2005. **44**(25): p. 3857-3861.
170. Sadakane, M., et al., *Synthesis of Orthorhombic Mo-V-Sb Oxide Species by Assembly of Pentagonal Mo6O21 Polyoxometalate Building Blocks.* Angewandte Chemie International Edition, 2009. **48**(21): p. 3782-3786.
171. Sun, R.Q., et al., *Syntheses and spectral study of three polyoxuvanadium clusters.* Spectroscopy and Spectral Analysis, 2006. **26**(2): p. 282-286.
172. Robbins, P.J., et al., *Use of ion-mobility mass spectrometry (IMS-MS) to map polyoxometalate Keplerate clusters and their supramolecular assemblies.* Chemical Communications, 2013. **49**(19): p. 1909-1911.
173. Sanchez Sanchez, M., et al., *Aiding the Self-Assembly of Supramolecular Polyoxometalates under Hydrothermal Conditions To Give Precursors of Complex Functional Oxides.* Angewandte Chemie International Edition, 2012. **51**(29): p. 7194-7197.
174. Konya, T., et al., *An orthorhombic Mo3VOx catalyst most active for oxidative dehydrogenation of ethane among related complex metal oxides.* Catalysis Science & Technology, 2013. **3**(2): p. 380-387.
175. Aouine, M., J.M.M. Millet, and J.L. Dubois, *Crystal chemistry and phase composition of the MoVTeNbO catalysts for the ammoxidation of propane.* Chemical Communications, 2001(13): p. 1180-1181.

Vita

Sabrina Jung, born in Gießen, Germany

Education

Master of Science in chemistry at Justus-Liebig-University Gießen, September 2014. Thesis title *"Preparation and characterization of photoelectrodes in the system Ca-Mn-O"*

Bachelor of Science in chemistry at Justus-Liebig-University Gießen, September 2012. Thesis title *"Synthesis and electrochemical characterization of lithium ion and mixed conducting garnet-type solid electrolytes"*

Publications

T. Lunkenbein, L. Masliuk, S. Jung, M. Jastak, A. Trunschke and R. Schlögl, *"Disclosing the Real Structure of Complex Mixed Oxides",* 2018, to be published

M. Marianski, J. Seo, S. Jung, R. Schlögl, G. Meijer, A. Trunschke, and G. von Helden, *„Structural determination of molybdenum oxide nanoclusters present in early condensation stages",* 2018, to be published

Presentations at Professional Meetings

Poster "Investigation of molybdate species in aqueous solution at different concentrations and pH values", S. Jung, A. Trunschke, R. Schlögl,

49. Jahrestreffen Deutscher Katalytiker, Weimar, 16.-18.3.2016

Poster "Using a free electron laser to determine the structure of precursor molecules in catalyst synthesis", S. Jung, M. Marianski, J. Seo, M. van Gastel, G. von Helden, A. Trunschke, R. Schlögl, 50. Jahrestreffen Deutscher Katalytiker, Weimar, 15.-17.3.2017

Poster "Structural reconstruction of polyoxomolybdates and –vanadates in the gas phase with free electron laser powered infrared spectroscopy", S. Jung, M. Marianski, J. Seo, M. van Gastel, G. von Helden, A. Trunschke, R. Schlögl, 25th North American Catalysis Society Meeting, Denver, 4.-9.6.2017

Poster “Investigation of vanadate species with ion-mobility mass spectrometry and spectroscopy and its prospects for catalyst synthesis”, S. Jung, M. Marianski, J. Seo, M. van Gastel, G. von Helden, A. Trunschke, R. Schlögl, EuropaCat, Florence, 27.-31.8.2017

Poster “Precursor analysis in catalyst synthesis studied by ion mobility-mass spectrometry and optical spectroscopy”, S. Jung, M. Marianski, J. Seo, M. van Gastel, G. von Helden, A. Trunschke, R. Schlögl, 8th World Congress o Oxidation Catalysis, Krakow, 3.8.9.2017

Presentation “Substituting Vanadium in the M1 Structure of (Mo,V)Ox for Oxidative Dehydrogenation of Light Alkanes”, S. Jung, P. Kube, A. Trunschke, R. Schlögl, 51. Jahrestreffen Deutscher Katalytiker, Weimar, 14.-16.3.2018

Poster “Substituting Vanadium in the M1 Structure of (Mo,V)Ox for Oxidative Dehydrogenation of Light Alkanes”, S. Jung, P. Kube, A. Trunschke, R. Schlögl, 7. Berliner Chemie Symposium Berlin, 5.4.2018